The Role of SWI/SNF Chromatin Remodeling Complex Subunit BAF60a in Vascular Diseases

by

Yang Zhao

A dissertation submitted in partial fulfillment
of the requirements for the degree of
Doctor of Philosophy
(Pharmacology)
in the University of Michigan
2022

Doctoral Committee:

Professor Y. Eugene Chen, Co-Chair
Associate Professor Jifeng Zhang, Co-Chair
Assistant Professor Matthew J Brody
Associate Professor Michael Holinstat
Professor Jiandie Lin

Yang Zhao

ypharan@umich.edu

ORCID iD: 0000-0002-1428-5145

© Yang Zhao 2022

Dedication

To my family, mentors, and all beloved friends, for your endless support, inspiration, and accompaniment throughout the journey

Acknowledgments

First, I would like to give my sincere thanks to my advisor, Dr. Eugene Chen, for his kind support during my research training, illuminating guidance on making moves under tough decisions, and profound knowledge of selecting targets, designing protocols, conducting experiments, analyzing results, performing troubleshooting, wrapping up the story and countless pieces of stuff related to being a good researcher.

I also want to thank Dr. Jifeng Zhang for being the best co-mentor I can think of, constantly staying positive and never complaining, who helped me through every step of the experiment details and taught me how to communicate with peers.

Being in Chen's lab for the past five years has been a great experience. All lab members are easy to communicate with and always willing to help each other. Dr. Ziyi Chang, a former graduate student, led me through the beginning of the experiments. Dr. Guizhen Zhao and Dr. Haocheng Lu taught me how to handle animals and perform bioinformatics analysis. Dr. Wenying Liang and Dr. Huilun Wang provided various suggestions for my research. In addition, I want to thank Dr. Tianqing Zhu for being an excellent lab manager and Dr. Minerva T. Garcia-Barrio for helping me revise manuscripts.

My dissertation committee members, Dr. Jiandie Lin, Dr. Matthew J Brody, and Dr. Michael Holinstat, have been with me since my second year and have guided me through my entire graduate study. The kind suggestions and encouragement from the committee helped me improve the quality of my work and move further confidently.

I am grateful to the Rackham Graduate School, Endowment for Basic Sciences, and American Heart Association for providing funding, recognizing, and motivating me. In addition, I want to thank the Department of Pharmacology for allowing me to step into the pharmacological field and providing valuable education related to academic success. Besides, my most profound appreciation goes to Dr. Stephen K. Fisher for recommending me to the program.

At last, I deeply appreciate my entire family. I grow up with you. I grow strong with you. Memories of love and happiness have accompanied me every day of my past life, and I make sure these shall continue.

There are many more people I could not list, but I want to share my appreciation. I am fortunate to have you all. Without your help, it would be impossible for me to achieve the end of my doctoral training.

Table of Contents

Dedication ii

Acknowledgments iii

Table of Contents v

List of Tables x

List of Figures xi

Abstract xiii

Chapter 1 Introduction 1

1.1 Overview 1

1.2 SWI/SNF Chromatin Remodeling Complex 4

1.2.1 The ATP-dependent chromatin remodeler 4

1.2.2 The SWI/SNF chromatin remodeler 5

1.2.3 SWI/SNF chromatin remodeler in cancers 8

1.2.4 SWI/SNF chromatin remodeler in cardiac development and disorder 8

1.2.5 SWI/SNF chromatin remodeler in neuronal functions 9

1.2.6 SWI/SNF chromatin remodeler as an emerging therapeutic target 10

1.3 Cell Type and Context-dependent Differential Activity of BAF60a 11

1.3.1 The BAF60 a, b and c subunits 11

1.3.2 BAF60a in liver and cholesterol metabolism 11

1.3.3 BAF60a in adipose tissue and cold-induced thermogenesis 13

1.3.4 BAF60a in macrophages and diabetic obesity 14

1.4 Summary 15

Chapter 2 Disordered Epigenetic-Metabolic Crosstalk in BAF60a Deficiency Macrophages Dampens Mitochondrial Energy Homeostasis and Promotes Atherosclerosis 16

2.1 Introduction 16

2.2 Materials and methods 20

2.2.1 Antibodies and reagents 20

2.2.2 Animal procedures 20

2.2.3 Histology 21

2.2.4 Lipoprotein fractionation and quantification 21

2.2.1 Plasma cholesterol, glucose, and complete blood count (CBC) 22

2.2.2 Cell culture 22

2.2.3 Western blot (WB) 23

2.2.4 Quantitative real-time PCR (qPCR) 23

2.2.5 Plasma cytokine enzyme-linked immunosorbent assay (ELISA) 23

2.2.6 Dissecting aortic cell population by fluorescence-activated cell sorting (FACS) 24

2.2.7 Cell adhesion assay 24

2.2.8 Nucleofection of siRNAs and plasmids 25

2.2.9 Intravital microscope of in vivo leukocyte adhesion 25

2.2.10 Oxygen consumption rate measurement by seahorse 25

2.2.11 Mitochondrial DNA copy number 26

2.2.12 Transmission electron microscopy (TEM) 26

2.2.13 Annexin V/PI assay 26

2.2.14 Lactate dehydrogenase (LDH) activity assay 26

2.2.15 Cell and mitochondrial staining 27

2.2.16 Co-immunoprecipitation 27

2.2.17 Assay for Transposase-Accessible Chromatin using sequencing (ATAC-seq) 27

2.2.18 Statistical analysis 27

2.3 Results 29

2.3.1 BAF60a expression positively correlates with mitochondria gene expression in human atherosclerotic macrophages 29

2.3.2 BAF60a is downregulated in murine atherosclerotic macrophages 33

2.3.3 Myeloid BAF60a deficiency exacerbates atherosclerosis in ApoE$^{-/-}$ mice 35

2.3.4 The effect of myeloid BAF60a in atherosclerosis is vascular-localized and sex-independent 38

2.3.5 BAF60a deletion enhances leukocyte recruitment in the vasculature 40

2.3.6 BAF60a deficiency does not affect foam cell formation in vitro 44

2.3.7 BAF60a deficiency in macrophages induces mitochondria dysfunction 46

2.3.8 Environmental cue links BAF60a deficiency to mitochondria dysfunction, cell toxicity and apoptosis 49

2.3.9 Loss BAF60a disrupts NRF1 accessibility at key mitochondria genes while NRF1 overexpression reverses mitochondria dysfunction 52

2.4 Discussion 56

Chapter 3 Investigates the Role of Smooth Muscle BAF60a in Abdominal Aortic Aneurysm 59

3.1 Acknowledgment 59

3.2 Introduction 59

3.3 Materials and methods 62

3.3.1 Antibodies and reagents 62

3.3.2 Human patient aortic samples 62

3.3.3 Animal procedures 63

3.3.4 Immunostaining and immunohistochemistry 65

3.3.5 Flow cytometry analysis of murine aorta 66

3.3.6 RNAscope in situ hybridization 67

3.3.7 Isolation of mouse aortic smooth muscle cells 67

3.3.8 siRNA-mediated BAF60a knockdown 68

3.3.9 Adenovirus-mediated BAF60a overexpression 68
3.3.10 Protein extraction and western blotting 69
3.3.11 mRNA isolation and qPCR analysis 69
3.3.12 RNA-sequencing 70
3.3.13 Chromatin immunoprecipitation (ChIP) assay 71
3.3.14 Chromatin immunoprecipitation followed by sequencing (ChIP-seq) 72
3.3.15 Co-immunoprecipitation 72
3.3.16 Immunofluorescence staining of cultured cells 73
3.3.17 ELISA 73
3.3.18 Macrophage migration assay 73
3.3.19 Statistical analyses 74
3.4 Results 75
3.4.1 BAF60a is highly expressed in human and murine AAA 75
3.4.2 BAF60a deficiency in VSMCs attenuates AngII-induced murine AAA formation 78
3.4.3 BAF60a deficiency in VSMCs attenuates elastase-induced murine AAA formation 81
3.4.4 BAF60a deficiency in VSMCs reduces ECM degradation in AAA lesions 84
3.4.5 BAF60a deficiency in VSMCs suppresses inflammatory response in AAA lesions 88
3.4.6 BAF60a knockdown reduces VSMC inflammation 91
3.4.7 BAF60a overexpression aggravates VSMC inflammation 94
3.4.8 BAF60a regulates Cathepsin S expression in VSMCs 96
3.4.9 BAF60a is required for SWI/SNF recruitment to the promoters of NF-κB target genes 98
3.5 Discussion 102
Chapter 4 Summary and Perspectives 105
4.1 Summary 105
4.2 Perspective 107

4.2.1 Generation and characterization of a sex-independent smooth muscle-targeted inducible Cre recombinase mouse model 107

4.2.2 The three-way balance between BAF60a, b, and c 112

4.3 Concluding remarks 113

Bibliography 114

List of Tables

Table 1.1 List of Common Nomenclature for SWI/SNF complex subunits. The table summarizes the nomenclature for the common and exclusive subunits of the three mSWI/SNF complexes. ... 7

Table 2.1 Complete blood count of Baf60a^{mKO}/ApoE$^{-/-}$ and Baf60a$^{f/f}$/ApoE$^{-/-}$ mice fed WD for different time points (N=3/group). 41

List of Figures

Figure 2.1 BAF60a positively correlates with mitochondria-high macrophages in human plaques 32

Figure 2.2 BAF60a is reduced in mouse atherosclerotic macrophages. 34

Figure 2.3 Myeloid BAF60a deficiency exacerbates atherosclerosis in Apoe−/− mice 37

Figure 2.4 The effect of myeloid BAF60a in atherosclerosis is vascular-localized and sex-independent 39

Figure 2.5 BAF60a deletion enhances leukocyte recruitment in the vasculature 43

Figure 2.6 BAF60a deficiency does not affect foam cell formation in vitro 45

Figure 2.7 BAF60a deficiency in macrophages induces mitochondria dysfunction 48

Figure 2.8 Environmental cue links BAF60a deficiency to mitochondria dysfunction, cell toxicity and apoptosis 51

Figure 2.9 Loss BAF60a disrupts NRF1 accessibility at key mitochondria genes while NRF1 overexpression reverses mitochondria dysfunction 55

Figure 2.10 Schematic model of BAF60a regulation of macrophage mitochondria dysfunction and atherosclerosis. 58

Figure 3.1 BAF60a is upregulated in human and murine AAA. 77

Figure 3.2 BAF60a deficiency in VSMCs attenuates AngII-induced murine AAA formation.... 80

Figure 3.3 BAF60a deficiency in VSMCs attenuates elastase-induced murine AAA formation. 83

Figure 3.4 BAF60a deficiency in VSMCs reduces ECM degradation in AAA lesions 87

Figure 3.5 BAF60a deficiency in VSMCs suppresses inflammatory response in AAA lesion.... 90

Figure 3.6 BAF60a knockdown reduces VSMC inflammation 93

Figure 3.7 BAF60a overexpression aggravates VSMC inflammation 95

Figure 3.8 BAF60a regulates Cathepsin S expression in VSMCs 97

Figure 3.9 BAF60a is required for SWI/SNF recruitment to the promoters of NF-κB target genes 101

Figure 3.10 Schematic model of BAF60a regulation of VSMC inflammation and ECM degradation in AAA development. 104

Figure 4.1 Generation and characterization of a sex-independent smooth muscle-targeted 111

Abstract

Cardiovascular diseases (CVDs) are the #1 killer worldwide in which both genetic and environmental factors play critical roles. Besides, various vascular diseases have revealed epigenetic modification of disease-related genes. The chromatin remodeling complex alters DNA accessibility and chromatin structure to modulate gene expression in response to external and internal cellular environmental cues. However, how the multiple CVD environmental stimuli coordinately alter chromatin remodeling in the context of vasculature remains poorly understood. SMARCD1, also known as BAF60a, is a transcription factor interacting subunit of the SWI/SNF (SWItch/Sucrose Non-Fermentable) chromatin remodeling complex, participating in various diseases. In the present work, we aimed to define the cell type-dependent role of BAF60a in underlying vascular diseases, particularly atherosclerosis and abdominal aortic aneurysm (AAA).

We found that BAF60a expression is positively correlated with mitochondria-high macrophages in human plaques. Myeloid BAF60a deletion dampens mitochondria integrity and induces macrophage ROS production and apoptosis, aggravating mouse plaque formation. Mechanistically, we found that BAF60a is essential for macrophage mitochondrial homeostasis under pro-atherosclerotic stress by retaining Nuclear Respiratory Factor 1 (NRF1) accessibility at essential nuclear mitochondrial genes in an SWI/SNF complex-dependent manner. Overexpression of NRF1 functionally rescues macrophage mitochondrial dysfunction caused by BAF60a deficiency. We further studied the effect of BAF60a deficiency in vascular smooth

muscle cells (VSMCs) on AAA formation. In human and mouse aneurysm tissues, BAF60a expression is increased. VSMC-specific knockout of BAF60a inhibits the development of murine AAA by significantly reducing vascular inflammation, monocyte infiltration, and elastin fragmentation. Furthermore, BAF60a regulates VSMC inflammation by attracting BRG1 to the promoter region of NF-κB target genes. In addition, the absence of BAF60a in VSMCs hindered the overexpression of the proteolytic enzymes, thereby ameliorating extracellular matrix degradation in the aneurysm arterial wall. Finally, we generated a novel CreERT2 knock-in mice model compatible with smooth muscle-targeted deletion of Baf60a and other genes in both male and female sex, allowing sex-oriented study that previously could not achieve.

Our work demonstrated the role of macrophage BAF60a-transcription factor interaction in combating atherosclerosis while also showing that BAF60a is required to recruit the SWI/SNF complex to facilitate the epigenetic regulation of VSMC inflammation in AAA. Highly cell type and context-dependent role of BAF60a in vascular diseases like atherosclerosis and AAA suggest functional compensation of disordered epigenetic-disease crosstalk as a potential therapeutic target.

Chapter 1 Introduction

1.1 Overview

Despite ongoing advances in diagnosis and treatment, CVDs remain the leading cause of death worldwide[1]. Atherosclerosis is a multifocal, chronic inflammatory disease that affects large and medium-sized arteries and is the main pathological change underlying most CVDs, such as myocardial infarction and ischemic stroke[2, 3]. In addition, atherosclerosis is associated with many other diseases and risk factors, including hyperlipidemia, diabetes mellitus, hypertension, smoking, and aging[4]. Specifically, macrophages are the predominant immune cell population in arterial plaques. Lipid-laden macrophages called foam cells play a crucial role in the formation of atherosclerosis by ingesting modified lipids and the consequent inhibition of cholesterol efferocytosis. However, these foam cells are incapable of moving and get trapped inside the plaque, which eventually dies and forms the necrotic core[5].

Recent research has uncovered that atherosclerotic plaque has a complicated metabolic milieu. In addition, it has been claimed that cells within the unstable plaque have a higher glycolysis rate, increased amino acid utilization, and suppressed fatty acid oxidation (FAO) in contrast to stable plaques[6]. Inactive M0 macrophages acquire energy mainly through oxidative phosphorylation (OXPHOS)[7]. In contrast, M1 or M2-polarized macrophages appear to shift to an energy-generation metabolic state reflective of their respective microenvironments[8]. Several recent studies utilizing single-cell transcriptomics to dissect cell suspensions within the atherosclerotic plaque have uncovered at least five major macrophage clusters in the murine atherosclerosis model, which partially resemble those in humans and await further study[9].

Aortic aneurysm (AA) is an asymptomatic disease with a high mortality rate upon rupture or dissection, making it the 13th leading killer (CDC-Aortic Aneurysm Fact Sheet). Thoracic (TAA) is highly associated with genetic mutations without sexual dimorphism[10]. In contrast, abdominal (AAA), which usually affects the infrarenal aorta, shows a relatively weak genetic association[11, 12]. Instead, it has often been related to well-known risk factors, including atherosclerosis, aging, high cholesterol, tobacco use, and male sex (4-5 times higher than females, albeit often with increased severity in women)[13]. AAA is a primary medical concern due to its increasing prevalence and mortality. Open or endovascular surgical repairs, which are only suitable for 10% of all aneurysmal patients, are still the only therapeutic option associated with lingering mortality risks[14]. There are no effective drugs currently for AAA treatment, likely due to limitations in understanding the underlying pathological and molecular mechanisms of AAA.

Vascular wall damage, reactive oxygen species (ROS), extracellular matrix degradation, SMC dysfunction and apoptosis are widely accepted pathological hallmarks of AAA. Nonetheless, in clinical trials, all orally bioavailable drugs targeting these processes or pathways were less effective than expected, particularly in secondary and tertiary prevention [15, 16]. These include anti-hypertensive drugs, ACE inhibitors, HMG-COA reductase inhibitors (statins), PYP12 inhibitors, TGFβ-1 inducers, mast cell inhibitors, anti-inflammatory drugs, curcumin, and metformin[17, 18]. Furthermore, pharmacologic and life style modifications of those risk factors have shown variable results in the early intervention[16]. The fact that inhibition of any of these processes individually is insufficient to prevent AAA progression in human clinical trials underscores the complexity of the pathogenesis of AAA. It highlights the need for a better

understanding of AAA formation to develop novel management procedures and treatment strategies[19, 20].

The broad term "epigenetic" defines changes in gene expression levels without involving DNA sequence alterations, including DNA methylation, histone modification, noncoding RNA, and ATP-dependent chromatin remodeling[21]. Epigenetic modifications and chromatin remodelings have been confirmed to be involved in various physiological and disease-associated conditions that regulate disease response gene expression[22]. Understanding how these complicated environmental conditions coordinate and concurrently alter the chromatin structure and DNA expression in the context of vascular diseases like atherosclerosis and aneurysm, and how they cross-talk with cells in the vasculature, will enhance the chance of identifying new therapeutic targets in CVDs.

1.2 SWI/SNF Chromatin Remodeling Complex

1.2.1 The ATP-dependent chromatin remodeler

In eukaryotic creatures, DNA is condensed around nucleosomes, forming the basic packing unit. DNA that is compact and difficult to access is encircled in close proximity by a nucleosome core that is made up of histone octamers. Because of these close connections, nucleosomes are inhibitory in nature since they block the vast majority of nucleotide-interacting elements by limiting their availability to access the DNA duplexes[23]. In addition, via modification and replacement, the histone complexes are widely involved in "epigenetic coding," which is vital for allowing cells to react to environmental changes and signals[24]. The capacity of a cell to adapt to its surroundings and survival pressures depends on the two-way communications between cellular function and the surrounding environment. For instance, cells possess a remarkable potential to detect varied surroundings and reprogram metabolic activity and proliferative potential appropriately. The inability to adapt can result in cell death, developmental abnormalities, and illness. Indeed, abnormalities in energy metabolism are a significant contributor to several diseases, including metabolic and cardiovascular diseases[25].

Repositioning and compositional alterations of histones are dependent on the chromatin-remodeling machinery. The ATP-dependent chromatin remodelers are evolutionarily conserved complexes that regulate several DNA-templated activities, such as replication, repair, and transcription, by actively modifying histone-DNA interactions. Specifically, chromatin remodeling can actively control gene expression by modulating transcription factor accessibility to the chromatin. Chromatin remodelers are necessary for maintaining and promoting epigenetic landscape alterations in response to environmental changes. In addition, as evidenced by the

proven function involving numerous disease contexts, chromatin remodeling is essential for maintaining cellular homeostasis and lineage dependence[26-29].

A variety of complex-dependent subunits surround the core structure of chromatin remodelers. Each of these contributes to the wide range of diversity and classes of the remodelers. These remodelers interact differentially with the genome to change the activities of the interacting genomic DNA. Remodelers can accelerate various remodeling activities at histones leading to chromatin structural changes, including but not limited to the assembly, replacement, sliding, or repositioning changes based on their different composition of subunits[30-32]. Four prominent remodeler families have spiked the most study interest to date. These families include SWI/SNF, ISWI, CHD, and INO80[30]. The main focus of the present work is on SWI/SNF complex.

1.2.2 The SWI/SNF chromatin remodeler

The SWI/SNF chromatin remodeling complex represents a class of multiunit complexes that are genetically closely related. They were initially identified in yeast and were termed for their role in the production of SUC2 for sucrose non-fermenting (SNF) and the activation of HO for mating-type switching (SWI)[33, 34]. Several SNF and SWI genes were subsequently discovered to produce proteins that physically aggregate as a large (1.14 MDa) multiunit complex in yeast, containing SWI2/SNF2 as ATPase subunit and exhibiting nucleosome remodeling activity dependent on ATP hydrolysis[35, 36]. Brahma (BRM) is the equivalent of the yeast SWI2/SNF2 ATPase component in Drosophila, and it forms a complex with other proteins called BAP (short for Brahma-associated protein)[37].

In mammals, the combination of genes expressing SWI/SNF complex subunits assembles into three distinct BAF(BRG1/BRM associated factor) classes. These classes are referred to as canonical BAF (cBAF), polybromo-associated BAF (PBAF), and noncanonical BAF (ncBAF). Generally, cBAF is the most common type, while ncBAF is the least common form of SWI/SNF. Every SWI/SNF complex has unique subunits shared with other complexes. All three SWI/SNF complexes comprise DNA binding subunits BRG1 or BRM. In addition, they possess ATPase functions and utilize ATP to alter DNA accessibility by controlling their compatibility[31, 38, 39]. However, it is not yet fully known how noncatalytic subunits contribute to nucleosome remodeling. The cBAF complex is a multi-member complex that includes two BAF250 proteins, BAF250A or BAF250B, and the tandem PHD domain-containing BAF45D subunit. The PBAF complex contains BAF200 rather than BAF250A or BAF250B. In addition, it contains the BRM containing BAF180, BRD7, and BAF45A with PHD components. ncBAF is the most recent mSWI/SNF complex discovered and described, comprises the GLTSCR1/GLTSCR1L and BRD9 subunits and neither a BAF250 nor tandem-PHD PHF/DPF component[40, 41].

These unique SWI/SNF complexes connect to various genomic positions, including distal enhancers, promoters, and CTCF-binding sites, where they facilitate and maintain DNA accessibility to control gene transcription. SWI/SNF is often associated with transcriptional activation. However, it may also target and orient histones to enable the attachment of restriction transcription factors (TFs) or to establish a suppressive genomic architecture[42]. Common Nomenclature for SWI/SNF complex subunits is listed in Table 1.1.

Canonical BAF (cBAF)	Polybromo-associated BAF (PBAF)	Non-canonical BAF (ncBAF)	Common subunits
ARID1a	ARID2	BRD9	SMARCC1
(BAF250A)	(BAF200)	BICRA	(BAF155)
(SMARCF1)	PBRM1	(GLTSCR1)	SMARCC2
ARID1b	(BAF180)	BICRAL	(BAF170)
(BAF250B)	BRD7	(GLTSCR1L)	SMARCA4
DPF2	PHF10		(BRG1 or BAF190A)
(BAF45D)	(BAF45A)		SMARCA2
DPF3			(BRM or BAF190B)
(BAF45C)			SMARCB1
BCL11A			(BAF47 or SNF5)
BCL11B			SMARCE1 (BAF57)
			SMARCD 1, 2, 3
			(BAF60a, b, c)
			ACTB
			ACTL6A, 6B
			(BAF53A, 53B)
			BCL7A, 7B and 7C
			SS18 (SYT or SSXT)

Table 1.1 List of Common Nomenclature for SWI/SNF complex subunits. The table summarizes the nomenclature for the common and exclusive subunits of the three mSWI/SNF complexes.

1.2.3 SWI/SNF chromatin remodeler in cancers

It has been reported that mutations in the genes that make up SWI/SNF complexes subunits have been found in over 20% of human cancers, making these genes the most frequently altered ones among all chromatin remodeling complex genes[43]. As a result, BAF250A, BAF180, BRG1, and BAF180 are currently included in regular diagnostic cancer-screening panels since their mutation frequency is high in many major cancer types. Intriguingly, distinct SWI/SNF complex members are often mutated differently in various cancer subtypes. For example, BAF47 deletion is seen in more than 90 percent of epithelial sarcomas while seldomly found in other types. In addition, BAF250A and BRG1 are often mutated in several forms of cancer, despite their paralogs, BAF250B and BRM, having much less mutation frequency[44-46]. The cause for the widely existing SWI/SNF selectivity of subunits in certain forms of cancer calls for more specific future research. Despite this, the findings suggest the possibility of new therapy options by targeting the subunit-related dependency found in a significant number of cancer patients.

1.2.4 SWI/SNF chromatin remodeler in cardiac development and disorder

Mutations of multiple SWI/SNF complex subunits, including BRG1, BAF47, BAF60c, BAF155, and BAF250A, have been revealed to cause cardiac defects mediated embryo lethality[47]. For example, mutants of BRG1 caused hypoplastic right ventricles and outflow tracts, myocardial thinning, lack of a septum, growing endocardium, and embryonic mortality[48, 49]. Meanwhile, BAF250A is required for SWI/SNF recruitment to target genes like THBS1, inducing cardiac protection[50-52]. Moreover, PBAF-specific BAF180 and BAF200 may boost RXR, VDR, and PPAR transcriptional activity. BAF180 includes six BRM

domains that recognize and interact with the histone acetylation site. Its loss of function induces hypoplastic ventricles and ventricular defects, causing embryonic death[53, 54]. BAF200 participates in heart morphogenesis and coronary artery development[55]. The most prevalent BAF60 component in BAF and PBAF complexes in the heart is BAF60c. BAF60c, through its interaction with BRG1, TBX5 and GATA4, may direct non-cardiac mesoderm to become cardiomyocytes in the heart[43]. We and others also reported that BAF60c prevents AAA formation by preserving the contractile phenotype, suppressing inflammation, and preventing the apoptosis of VSMCs[56].

1.2.5 SWI/SNF chromatin remodeler in neuronal functions

SWI/SNF chromatin remodelers play a fundamental role in maintaining proper neuronal development and function, and numerous researchers have reported the association and causative functions between SWI/SNF subunit mutation and neuronal disorders[57]. For instance, the core subunits BRG1, BAF155, and BAF170 are involved in neuronal genesis, and their deletion or missense mutation leads to Coffin-Siris syndrome (CSS) and autistic disorders[58, 59]. CSS is characterized by mutations in BAF subunits that combine intellectual impairment, growth retardation, joint deformities, brachydactyly, and hypoplastic or missing fifth finger/toe fingernails. In 70% of CSS instances, BAF250B is also mutated[60, 61]. In contrast to its paralogue, BAF250A mutation is also found in CSS but plays a significantly more prominent role in cancer[58, 62]. In addition, the BAF47 mutation is identified as the cause of rhabdoid tumors[63] and produces a severe type of CSS[64]. It is also reported to contribute to Kleefstra's syndrome[65]. Besides, BRM, BAF155, BAF170 and BAF100s are important for neural subtype determination[66, 67]. Mutations of BRM have been linked to Nicolaides-Baraitser syndrome

(NCBRS)[68]. Its pathological phenotypes include seizures, huge interphalangeal joints without inflammatory symptoms, significant cerebral disability with speech delay, development retardation, and unique facial features[69]. In addition to CSS, Kleefstra's syndrome, and NCBRS, various BAF subunit mutations have been linked to adrenoleukodystrophy, amyotrophic lateral sclerosis, and schizophrenia as well[59, 70-75].

1.2.6 SWI/SNF chromatin remodeler as an emerging therapeutic target

As a result of the high-frequency SWI/SNF complex subunits variants in cancer and other critical diseases, research into genetically defined reliance mechanisms is opening the door to novel therapeutic possibilities for a wide variety of human diseases with primary unmet medical needs. However, to date, targeting SWI/SNF complex subunits is still challenging, especially in the circumstance of enhancing the activity under missense mutation. Although several small inhibitors and PROTAC-based drugs targeting cancer-specific overrepresented SWI/SNF subunits or synthetic lethality have been proposed and examed[41, 76-81], better identification and functional knowledge of SWI/SNF complex activities will make it easier to expedite drug development efforts targeting distinct SWI/SNF complex variations in other non-cancer diseases. On the other hand, specific targeting of the cell type and context-dependent alterations of SWI/SNF chromatin remodeler subunits abundance, as well as the functional rescuing of the downstream signaling networks, seem to be also valuable for the treatment of metabolic and inflammatory diseases in which environmental stress and epigenetic modifications play important roles.

1.3 Cell Type and Context-dependent Differential Activity of BAF60a

1.3.1 The BAF60 a, b and c subunits

The BAF60 subunits, BAF60a, BAF60b, and BAF60c, are also referred to as SMARCD1, SMARCD2, and SMARCD3, respectively. BAF60s are unique among all the mSWI/SNF subunits since they operate as a bridge connecting the SWI/SNF complex and specific transcription factors[82-85]. Such interaction regulates the expression patterns of specific target genes. It is evidenced that different amounts of transcription factors may compete for BAF60 binding in response to varied stimuli, resulting in a change in the specificity of promotes and gene expression level[83]. In addition, the specific actions of each isoform are provided by the various tissue distribution patterns and regulatory mechanisms of BAF60s. The differential controls that BAF60s exert in the context of metabolic and inflammatory diseases have been demonstrated in previous researches[56, 86-91].

1.3.2 BAF60a in liver and cholesterol metabolism

The liver is a primary metabolic organ and plays a crucial role in regulating systemic glucose and lipid homeostasis. The imbalance of hepatic lipid metabolism as a consequence of metabolic disorders like obesity and type II diabetes, contributes to the severe consequence of non-alcoholic fatty liver disease (NAFLD). NAFLD is characterized by an ectopic triglycerides (TG) buildup, which gradually leads to fatty liver, non-alcoholic steatohepatitis (NASH), liver fibrosis, and cirrhosis. To develop novel treatment strategies for NAFLD, a deeper understanding of the molecular pathways that regulate lipid metabolism and the crosstalk with epigenetic machinery in the liver is essential[92].

BAF60a, an interacting partner of PGC-1 in the liver, is identified by a genome-wide, high-throughput coactivation screen[87]. PGC-1 is an inducible coactivator for nuclear hormone receptors and transcriptional factors to control critical functional pathways, such as mitochondrial oxidative phosphorylation (OXPHOS) and hepatic gluconeogenesis[93]. The work demonstrated that BAF60a is a crucial linker between the SWI/SNF complex and the fatty acid oxidation gene regulatory network[87].

In addition, BAF60a was shown to inhibit cellular aging in HepG2 cells[94]. The treatment of HepG2 cells with palmitic acid decreased the expression of BAF60a, which led to the buildup of lipids and the senescence of HepG2 cells. Simultaneously, when mice were given a high-fat diet, the expression of BAF60a in the liver decreased considerably, resulting in lipid buildup and cell senescence[94]. Therefore, BAF60a showed application potential for liver lipid accumulation and cell aging and may be utilized to treat fatty liver and other liver metabolic illnesses[87, 94].

BAF60a also functions as a diet-induced component of the SWI/SNF complexes in the liver that connects cholesterol absorption to systemic lipid metabolism in the whole body. Hepatocyte-specific BAF60a loss consistently protected mice against diet-induced hypercholesterolemia and atherosclerosis, followed by decreased liver bile acid synthesis and decreased intestine cholesterol intake. In contrast, BAF60a overexpression increases plasma cholesterol levels[88]. Furthermore, BAF60a is necessary to bridge the ATP-dependent mSWI/SNF chromatin-remodeling complexes to CAR (constitutive androstane receptor) and alter its related genes to induce a chromatin and gene expression shift from inhibition to activation[88].

1.3.3 BAF60a in adipose tissue and cold-induced thermogenesis

BAF60a not only controls the lipid metabolism of the liver but also plays a crucial function in the thermogenesis of adipose tissue. White fat, the primary type of energy storage in the body, is mainly distributed in subcutaneous tissues and surrounding internal organs[95]. Brown fat has the ability to generate heat. Therefore, it highly expresses the genes responsible for heat generation and releases energy as heat through a large number of mitochondria. Under the influence of a cold environment, white adipocytes transform into beige fat, triggering the activation of thermogenic genes[96].

Liu et al. recently showed that BAF60a is necessary for brown fat thermogenesis in a cold environment[90]. Under the influence of a cold environment and adrenal hormone, the deletion of BAF60a inhibits the chromatin accessibility of the brown fat thermogenic gene, diminishing the thermogenic ability of cold-induced brown fat[90]. On the other hand, inactivation of the fat-specific BAF60a gene increases the browning of inguinal white adipose tissue in a cold environment. Such browning processes are associated with stimulating the adrenocorticotropic hormone (ACTH) receptor MC2R (Melanocortin 2 Receptor). In response to ACTH stimulation, increased MC2R expression uncouples the thermogenic response of adipocytes and BAF60a-deficient adipose tissue, revealing an interesting bidirectional role of BAF60a and its mediated chromatin remodeling in transcriptional alteration of brown and beige fat thermogenesis[90].

1.3.4 BAF60a in macrophages and diabetic obesity

Type II diabetes is a chronic, inflammatory cell-related disease in which the resident macrophage orchestrates chronic metabolic inflammation and contributes to the etiology of metabolic disease[97]. Classically activated M1 macrophages are characterized by the high secretion of pro-inflammatory cytokines and chemokines such as IL-6, IL-12, and TNF-α, which impair insulin signaling in the adipose tissue, while alternatively activated M2 macrophages protect against adipocytes dysfunction through inhibition of inflammation response. Adipose tissue-resident macrophages (ATMs) are balanced under physiological conditions. In contrast, recruited macrophages in the adipose tissue displayed an inflammatory behavior with increased obesity. Intriguingly, the metabolically active state of ATMs is distinct from the M1/M2 classification[91]. Nonetheless, the underlying mechanism that integrates environmental inputs to regulate ATM activity and adipose inflammation during obesity and type II diabetes remains unknown.

In a recent study, the authors found that among the three mutually exclusive BAF60 subunits, the expression of BAF60a is considerably decreased in the stromal vascular fraction (SVF) of white adipose tissue (WAT) under diabetic conditions [91]. Moreover, they demonstrated that different inflammatory stimulus is responsible for changes in BAF60a expression. Myeloid-specific BAF60a deletion in mice significantly exacerbated diabetes-related phenotypes such as insulin resistance, obesity, and resident macrophage activation. Mechanistically, transcription factor ATF3 interacts directly with BAF60a. The interaction inhibits inflammatory gene expression, thereby decreasing ATM and metabolic inflammation. This work identified BAF60a as a crucial chromatin remodeling factor that links obesity-associated stress signals with inflammation and systemic homeostasis[91].

1.4 Summary

Macrophage activation, OXPHOS, VSMCs inflammation, phenotypic switch, and apoptosis have been linked to CVDs such as atherosclerosis and AAA. However, how the multiple external stimuli coordinately and concurrently translate into those outcomes remains largely unknown. Epigenetic factors altering DNA accessibility and chromatin structure to modulate gene expression in response to the external and internal cellular environment stresses, and could serve as potential yet underexplored mechanisms to address that question. There is mounting evidence that BAF60a is an essential chromatin remodeling subunit bridging the interaction between DNA and disease/ cell type-dependent transcription factor activity in metabolic and inflammatory diseases. Understanding the dynamic regulation of BAF60a under various microenvironments permits the development of substances that can modulate its activity or compensate for the loss of function. Currently, most BAF60a biology research focuses on cancer, liver, and metabolic disorder. Understanding the biology of BAF60a in arterial wall biology and cardiovascular illnesses might aid in elucidating the pathophysiology of these conditions and offer us new therapeutic targets. In the present work, we described the involvement of BAF60a in macrophage mitochondria dysfunction and atherosclerosis in chapter 2. In chapter3, the involvement of BAF60a in vascular smooth muscle cell inflammation and the aortic aneurysm was summarized. Finally, in chapter 4, we concluded the work and reported the generation of a new inducible SMC-specific CreERT2 mice model compatible with smooth muscle-targeted deletion of Baf60a and other genes in both male and female sex, in which the previous Y-chromosome located CreERT2 mice cannot achieve.

Chapter 2 Disordered Epigenetic-Metabolic Crosstalk in BAF60a Deficiency Macrophages Dampens Mitochondrial Energy Homeostasis and Promotes Atherosclerosis

2.1 Introduction

Atherosclerosis is a chronic progressive disease initiated from intimal damage, inflammatory cell infiltration, smooth muscle cell migration, and lipid accumulation, gradually leading to calcification and plaque rupture. It is a major killer worldwide and the underlying cause of most cardiovascular diseases (CVDs). Build-up and rupture of the plaque resulted in life-threatening clinical complications, including but not limited to myocardial infarction and ischemic stroke[2, 3]. Through innate and adaptive responses, immune cells like monocytes/macrophages, DCs, T cells, and B cells contribute significantly to the formation, development, vulnerability, and regression of atherosclerotic plaques[98-105]. Despite that current LDL-lowering drugs, such as statins and PCSK9 inhibitors, effectively reduce blood lipid levels in compatible patients, residual major cardiovascular events remain high[106, 107]. On the other side, the clinical benefit of anti-inflammatory therapy for atherosclerosis is also limited to patients with increased systemic inflammatory markers, urges for drug targeting additional pathways, and an in-depth understanding of the challenging nature of the cell-environmental communication of the disease[108, 109].

Broadly defined as the change in gene expression levels without involving DNA sequence alterations, epigenetics has been confirmed to be involved in developing various diseases. For example, while large-scale population studies revealed multiple genetic variations

associated with CVDs, CVD risks and the development of atherosclerosis in response to risk stimuli are also controlled by changes at the epigenetic level, including DNA methylation, histone modification, noncoding RNAs, and ATP-dependent chromatin remodeling, in a microenvironment and cell type-dependent manner[56, 110-117].

Macrophages are the primary immune cells that participate dynamically in the initiation, necrotic core formation, and regression of atherosclerosis[118]. The intrinsic plasticity and the plaque environmental heterogeneity switch atherosclerotic macrophages into various subtypes, far more complicated than the M1 and M2 classification that originated in vitro[119]. Traditional classification based on membrane protein expression reported at least eight macrophage subtypes associated with atherosclerosis, with known functions ranging from escalating inflammation, inflammatory cell recruiting, phago- and efferocytosis, lipid and iron metabolism, to calcification and plaque repairment[119-127]. More recent techniques utilizing single cell transcriptomics, CyTOF, and CITE-Seq, cross-referenced to characterize plaque macrophages into 5 clusters further, including Lyve1 and Mrc1 high resident-like macrophages, Trem2 high foamy macrophages, circulating derived Ccr2 high macrophages with high chemokines, Interferon induced Ifit3 and Irf7 high macrophages, and Itgax high cavity macrophages[9, 128-133].

The mitochondrion is the primary powerhouse of most cells, including macrophages[134]. Pyruvate from glycolysis and fatty acids are oxidized and joins amino acid metabolites to enter the TCA cycle inside the mitochondria matrix. Protons are carried to the electron transport chain (ETC), producing chemo gradients at the intermembrane spaces and generating ATP in the process called oxidative phosphorylation (OXPHOS) to fuel cell activities. Microenvironment changes that shift the mitochondria energy balance between OXPHOS and glycolysis have been closely linked to differential macrophage subtypes and

functions in inflammatory and metabolic diseases like atherosclerosis[135-141]. Accumulating evidence suggests that the disease microenvironment reprograms immune cell metabolic processes at the epigenetic level. Concurrently, cellular metabolites also participate in regulating epigenetic machinery[142, 143]. For example, macrophages exposed to IL-4 displayed increased acetyl-CoA production and elevated α-ketoglutarate (AKG) to succinate ratio, associated with an increase in histone acetylation[143-145]. While LPS treatment increases histone methylation, accompanied by suppressed mitochondrial OXPHOS in macrophages[146-148]. Noncoding RNAs like miRNAs were also reported to regulate mitochondria function and control the fate of macrophage activation[149, 150].

The mammalian SWI/SNF complex is the largest of the ATP-dependent chromatin remodeling complex, containing 10 to 15 subunits varying by subtypes. It utilizes energy from ATP hydrolysis to either slide or evicts nucleosomes, enabling transcription machinery to access naked DNA. The complex subunits include one of the two ATPase catalytic Bromo and HSA regions containing BRG1 or BRM. Others are named by Brg1/Brm associated factors (BAFs) and molecular weight. The distinct assembly of SWI/SNF subunits allows context-specific functional variation of the SWI/SNF complex[39, 151, 152]. Of note, the three mutually exclusive SMARCD 1,2 and 3 subunits, also called BAF60a, b, and c, bridge the interaction between tissue-specific transcription factors(TFs)/cofactors and the SWI/SNF core complex to regulate gene expression changes in response to various inflammatory and metabolic complications[39, 56, 87, 88, 90, 91, 114, 153, 154]. To date, the influence of the complex atherosclerotic microenvironment on the interaction between BAF60s and TFs-mediated gene expression in immune cells remains to be defined.

In the present work, we reported drastically and significantly aggravated atherosclerotic lesions in hypercholesterolemia mice with myeloid BAF60a deletion. We systemically uncovered that environmental stress-induced temporal downregulation of BAF60a in atherosclerotic macrophages disrupts the accessibility of macrophage-specific TFs, especially NRF1, at essential mitochondrial genes to combat mitochondrial dysfunction, dysregulated energy homeostasis, cell toxicity, and apoptosis, contributing to plaque formation. The regulation between BAF60a and mitochondrial energy homeostasis in macrophages is an excellent example of the epigenetic-metabolic crosstalk altered by the disease microenvironment, revealing additional layers of targets for atherosclerosis therapy.

2.2 Materials and methods

2.2.1 Antibodies and reagents

Purified mouse Anti-BAF60a (611728) antibody was purchased from BD Biosciences (San Jose, CA). Rabbit antibodies against BAF60a (ab245222) and BAF60b (ab220164) were from Abcam (Cambridge, UK). Antibodies for BAF155 (rabbit, 11956), BRD9 (rabbit, 71232), PDH (rabbit, 3205), TOM20 (rabbit, 42406), β-actin (mouse, 3700), and rabbit IgG (2729) were purchased from Cell Signaling Technology (CST, Danvers, MA). Antibodies against TFAM (PA5-68789) and NRF1 (PA5-27854) were from Thermo Fisher Scientific (Waltham, MA). Antibody against Mac2 (14-5301-82) was from eBioscience (San Diego, CA). COX4 Antibody (NB110-39115) was purchased from (Novus Biologicals, Centennial, CO). Recombinant human TNFα protein (210-TA) was from R&D Systems (Minneapolis, MN). Low-Density Lipoprotein (LDL) was purchased from Lee Biosolutions (Maryland Heights, MO). Oxidation of LDL was prepared as previously reported[155]. Mouse siSmarcd1 (L-046893-01-0005), human siSMARCD1 (L-017244-00-0005) and siControl pool2 (D-001206-14-05) were from Dharmacon (Lafayette, CO). 7-Keto cholesterol (16339) was purchased from Cayman (Ann Arbor, MI). HA-NRF1 (MG52011-NY) was purchased from Sino Biological (Beijing, China). Anti-F4/80 MicroBeads (130-110-443) was purchased from Miltenyi Biotec (Gaithersburg, MD).

2.2.2 Animal procedures

C57BL/6J background BAF60a floxed ($BAF60a^{f/f}$) mice were described previously[88] and were crossbred with $ApoE^{-/-}$ (B6.129P2-$Apoe^{tm1Unc/J}$) and Lyz2Cre (B6.129P2-$Lyz2^{tm1(cre)Ifo/J}$) mice purchased from the Jackson Laboratory to generate the $BAF60a^{mKO}/ApoE^{-/-}$

mice. BAF60a$^{fl/fl}$/ApoE$^{-/-}$ mice were used as littermate control. All mice were kept on a regular 12h light/12 h dark cycle at 22 °C in a pathogen-free environment. Mice at 10 to 12-week-age were fed a high-cholesterol Western diet (Envigo, TD.88137) to induce hypercholesterolemia for an additional 8, 12, or 16 weeks, varying by experiments. All animal procedures were performed following the protocols approved by IACUC at the University of Michigan.

2.2.3 Histology

After sacrifice, mice were perfused with ice-cold saline through the left ventricle. The aortic root, liver, and eWAT tissue were dissected, fixed in formalin, embedded in paraffin or frozen OCT, and sectioned. The H&E staining, Oil Red O, and Mac2 histochemistry were performed by the IVAC at the University of Michigan. For the TUNEL apoptosis assay, paraffin-embedded aortic sections were stained with the ApopTag Peroxidase In Situ Apoptosis Detection Kit (S7100, Millipore Sigma) and counterstained with hematoxylin according to the manufacturer's recommendation. In addition, en-face staining of the whole aorta was conducted as previously described[156]. The quantification was done by Image J.

2.2.4 Lipoprotein fractionation and quantification

Fast protein liquid chromatography (FPLC), as mentioned previously[100], was used to determine the amount of cholesterol contained in specific lipoprotein particle fractions. Pooled fasting plasma from BAF60a^{mKO}/ApoE$^{-/-}$ and BAF60a$^{fl/fl}$/ApoE$^{-/-}$ mice were analyzed by FPLC. After collecting and eluting a total of forty fractions, the total cholesterol content of each fraction was analyzed using a cholesterol fluorometric test kit (Cayman Chemical, 10007640).

2.2.1 Plasma cholesterol, glucose, and complete blood count (CBC)

Fasting plasma total cholesterol (TC) levels were measured by enzymatic kits (999-02601, Fujifilm Wako Diagnostics, Osaka, Japan). Fasting blood glucose was measured using a glucometer and glucose test strips (Ascensia, 0193-7308-50, Parsippany, NJ). CBC was performed by the IVAC at the University of Michigan.

2.2.2 Cell culture

BMDM: Bone marrow cells were flushed out of the femur and tibia from the lower limbs of 6-12-week-old mice with ice-cold DPBS. BMDMs were then cultured in BMDM differentiation medium (IMDM medium (Gibco, 31980030) + 10% FBS (Gibco, 10100147) + Non-Essential Amino Acids (Gibco, 11140050, 1:100) + 1mM Sodium Pyruvate (Gibco, 11360070) + Penicillin-Streptomycin (Gibco, 15140122, 1:100) + 25ng/mL M-CSF (R&D systems, 416-ML)) for 7 days before experiments.

THP-1: THP1 cells were purchased from ATCC (TIB-202) and cultured in RPMI1640 with 10% FBS. For THP1-derived macrophage, THP1 cells were treated with phorbol 12-myristate 13-acetate (PMA, Sigma, P8139) 100ng/mL for 72 hours.

RAW 264.7: RAW 264.7 cells were purchased from ATCC (TIB-71) and cultured in DMEM with 10% FBS. HAECs: HAECs (CC-2535) from a 54-year-old male were purchased from Lonza and cultured in EC growth media-2 (CC-3202, Lonza) from passages 4 to 8.

AD-293: AD-293 cells were purchased from Agilent (240085) and cultured in DMEM with 10% FBS.

2.2.3 Western blot (WB)

Tissue or cells were lysed in RIPA buffer (Thermo Fisher Scientific, 89901) with protease inhibitor (Roche, 11873580001) and phosphatase inhibitor (Roche, 4906845001). Proteins were resolved in SDS-PAGE gel and then transferred to the nitrocellulose membrane. Membranes were blocked with 5% fat-free milk or BSA for 1h at room temperature. Membranes were then incubated with primary antibody (1:1,000 dilution) at 4℃ overnight and then fluorescence-labeled secondary antibody (Li-Cor Bioscience) (1:5,000 to 10,000 dilution) at room temperature for 1h. The membrane was scanned and quantified using the Li-Cor DLx Odyssey imaging system.

2.2.4 Quantitative real-time PCR (qPCR)

Total RNA from tissue was purified using TRIzol (Invitrogen, 15596018). RNA was isolated from cells using RNeasy Mini Kit (Qiagen, 74106) and then reverse transcribed with SuperScript III kit (Thermo Fisher Scientific, 18080051) using random hexamer. mRNA was determined by BioRad Realtime PCR Detection System, using SYBR Green Fast qPCR Mix (Abclonal, RK21203). The mRNA level was normalized to the internal control, GAPDH.

2.2.5 Plasma cytokine enzyme-linked immunosorbent assay (ELISA)

MCP-1 and Il-6 levels in mouse plasma from both BAF60a^{mKO}/ApoE$^{-/-}$ mice and BAF60a$^{fl/fl}$/ApoE$^{-/-}$ mice group were measured by ELISA with the help of the Cancer Center Immunology Core at the University of Michigan.

2.2.6 Dissecting aortic cell population by fluorescence-activated cell sorting (FACS)

The aorta region of euthanized mice from both BAF60a^{mKO}/ApoE$^{-/-}$ mice and BAF60a$^{fl/fl}$/ApoE$^{-/-}$ mice group were washed with PBS containing 2% of heparin. A cocktail of collagenases (Gibco, 17100-017 and Sigma-Aldrich, C7657), hyaluronidase (Sigma-Aldrich, H3606), and DNase-I (Roche, 10104159001) were used for tissue digestion at 37°C for 90 minutes as previously described[155]. Single cells were filtered by a 100 μm cell strainer. Cells were further blocked by Fc block (eBioscience, 14-0161-85) for 5 to 10 minutes on ice. After blocking, cells were incubated with fluorochrome-conjugated antibodies for 30 minutes. Cells were then washed with PBS and fixed in 4% PFA before subjecting to FACS analysis by the Flow Cytometry Core at the University of Michigan[155]. Data were analyzed using FlowJo v10.6.1. Antibodies used for flow cytometry: CD16/CD32 for Fc block (eBioscience, 14-0161-85), eFluor 450 isotype control (rat IgG2b kappa, eBioscience, 48-4031-82), APC conjugated isotype control (rat IgG2a kappa, eBioscience, 17-4321-81), PerCP-cy5.5 isotype control (eBR2a, eBioscience, 45-4321-80), FITC isotype control (Biolegend, 400110), APC-Cy7 isotype control (BioLegend, 400623), CD45 (EF450, eBioscience, 48-0451-82), Ly6G (FITC, BioLegend, 127605), F4/80 Rat anti-mouse (APC, TONBO 130-102-471), CD11b (APC-Cy7, BioLegend, 101225), CD19 (FITC, BD Biosciences, 557398), CD3 (PerCP-Cy5.5, eBioscience, 45-0031).

2.2.7 Cell adhesion assay

HCECs at confluence were treated with TNFa (2ng/ml) for 6h, followed by washing with PBS and re-culturing in Opti-MEM medium (31985062, Gibco) for an additional 10h. THP-1 with siControl or siBAF60a were stained with 1uM Calcium A/M and sed onto the HCECs for 5h. The cells were washed with cold PBS three times, stained with NucBlue™ (R37605), and

visualized using a fluorescent microscope (Olympus, IX71). The NIH Image J analyzer was used for quantification.

2.2.8 Nucleofection of siRNAs and plasmids

Nucleofection of siRNAs and plasmids in THP-1 and RAW264.7 macrophages were performed using a Nucleofector™ 2b Device and Human Monocyte NucleofectorTM Kit (VPA-1007). The program and concentration were set according to the manufacturer's protocol.

2.2.9 Intravital microscope of in vivo leukocyte adhesion

Eight weeks old male Baf60a^{mKO} and Baf60a$^{f/f}$ mice were IP injected with 50 μg/kg LPS. In addition, mice were injected with rhodamine 6G chloride to label the leukocyte population 4 hours after the LPS administration. After anesthetization, the cremaster muscle was separated from the tissues around it. It was sliced lengthwise and then held flatly using a silk suture. At 37 degrees Celsius, the muscle was maintained wet by saline. Intravital microscopy was used to keep track of the leukocyte movement. The amount of rolling leukocytes was measured by counting cells that rolled past a stationary spot in one minute. Adhesion was determined if the leukocytes adhered to the endothelial layer and remained motionless for more than 30 seconds.

2.2.10 Oxygen consumption rate measurement by seahorse

The Seahorse XFe96 Analyzer from Agilent was used to measure the oxygen consumption rate (OCR). F4/80+ aortic macrophages isolated from the BAF60a^{mKO}/ApoE$^{-/-}$ mice and BAF60a$^{fl/fl}$/ApoE$^{-/-}$ mice group and BMDMs from Baf60a^{mKO} and Baf60a$^{f/f}$ mice were cultured in the 96-weel culture plate. OCR was measured following optimized cell type optimization from the manufacturers.

2.2.11 Mitochondrial DNA copy number

F4/80+ aortic macrophages isolated from the BAF60a^{mKO}/ApoE$^{-/-}$ mice and BAF60a$^{fl/fl}$/ApoE$^{-/-}$ mice group, and BMDMs from Baf60a^{mKO} and Baf60a$^{f/f}$ mice were digested with proteinase K. Genomic (nDNA), and mitochondrial DNA (mtDNA) were extracted and purified using Phenol:Chloroform: Isoamyl Alcohol (25:24:1, v/v). The mitochondrial DNA (mtDNA) to nuclear DNA (nDNA) ratio numbers were quantified by qPCR, as we previously described[100].

2.2.12 Transmission electron microscopy (TEM)

BMDMs from Baf60a^{mKO} and Baf60a$^{f/f}$ mice were treated with oxLDL (50μg/ml) for 48 hours in DMEM, followed by fixation and TEM imaging in the Microscopy Core of the University of Michigan.

2.2.13 Annexin V/PI assay

BMDMs from Baf60a^{mKO} and Baf60a$^{f/f}$ mice were treated with 7-KC (10μg/ml) for 24 hours in a serum-free medium. According to the procedure outlined before[157], the cells were first dissociated with 0.25% trypsin before being stained with the FITC Annexin V Apoptosis Detection Kit I. In general, the cells were washed with cold PBS, followed by suspension in a 1x binding buffer, and then labeled with FITC Annexin V and Propidium Iodide to finish (PI). Quantification was done by FACS at the University of Michigan core facility.

2.2.14 Lactate dehydrogenase (LDH) activity assay

BMDMs from Baf60a^{mKO} and Baf60a$^{f/f}$ mice were treated with 7-KC (10μg/ml) for 24 hours in Opti-MEM medium (31985062, Gibco). In addition, the LDH assay was performed with the LDH kit (MAK066) from Sigma-Aldrich according to the manufacturer's recommendation.

2.2.15 Cell and mitochondrial staining

BMDMs from Baf60a^{mKO} and Baf60a$^{f/f}$ mice were treated with oxLDL (50μg/ml) for 48 hours in DMEM, followed by staining with MitoTracker™ Deep Red FM (M22426), MitoSOX™ Red (M36008), HCS LipidTOX™ Green (H34475), or NucBlue™ (R37605), respectively, following the manufacturer's instructions. Cells were visualized using a fluorescent microscope (Olympus, IX71) and quantified by FACS in the Flow Cytometry Core at the University of Michigan. Data were analyzed using FlowJo v10.6.1.

2.2.16 Co-immunoprecipitation

For Co-IP, cells were lysed using Cell Lysis Buffer (CST, 9803) supplemented with PMSF (CST, 8553), immunoprecipitated using Protein G Magnetic Beads (CST, 7024), and antibodies against HA (ABclonal, AE008) following the manufacturer's protocol.

2.2.17 Assay for Transposase-Accessible Chromatin using sequencing (ATAC-seq)

BMDMs from Baf60a^{mKO} and Baf60a$^{f/f}$ mice were treated with oxLDL (50μg/ml) for 48 hours in DMEM. ATAC-seq of nuclei isolated from the cell was performed by the Epigenomics Core at the University of Michigan. The reads were mapped to the human genome (NCBI GRCh38) with bowtie2. The peak calling was done with MACS3 (with the following settings: -f BAMPE –g hs –B --SPMR –q 0.01). Motif enrichment analysis was performed using HOMER. Transcription factor footprints were analyzed via HINT-ATAC. BigWig tracks were visualized in IGV.

2.2.18 Statistical analysis

Statistical evaluations were conducted using the GraphPad Prism 9.0 program (available from GraphPad Software in San Diego, California). Data were presented as mean ± standard

error of the mean (SEM). If the data were normally distributed and had comparable variances, the Student's t-test (a parametric test) was used to compare the difference between the two groups. For comparisons among three or more groups, either a one-way ANOVA followed by post hoc or a two-way ANOVA followed by post hoc was performed. In addition, the Mann-Whitney test (nonparametric analysis), Chi-squared analysis (distribution analysis), or the Mantel-Cox test (a survival percentage analysis) were used to analyze the variations between the two groups when the data failed to pass the normality test. The results were deemed statistically significant if the p-value was less than 0.05. At least three separate experiments were performed for all results.

2.3 Results

2.3.1 BAF60a expression positively correlates with mitochondria gene expression in human atherosclerotic macrophages

To address whether and how the atherosclerotic microenvironment influences BAF60s and targeted gene expressions in immune cells, we first reanalyzed previously reported single-cell RNA sequencing (scRNA-seq) results, containing a total of 51,721 cells from three human atherosclerotic plaque samples and paired controls (GSE159677). Following quality control and normalization, unsupervised SNN-based clustering of cell types was performed[158]. With a specific focus, macrophage populations were extracted and mapped to the original population after clustering, revealing 14 cell clusters, including 4 macrophage subtypes (Fig. 2.1 A). As expected, the expression of BAF60c is more concentrated in the smooth muscle cell population. In contrast, BAF60a and b expressions are less cell type restricted (Data not shown). Notably, cells expressing a high level of BAF60a were mainly enriched in the Mφ4 cluster, while the Mφ3 cluster is one of the lowest BAF60a expression clusters (Fig. 2.1 B). GO pathway enrichment suggests critical genes involved in mitochondrion function and OXPHOS, such as Cytochrome C Oxidase Subunit 4I1(COX4I1), Mitochondrial Transcription Factor A (TFAM), Mitochondrial Transcription Factor B1 (TFB1M), Translocase of Outer Mitochondrial Membrane 20 (TOMM20) and Flavoprotein (FP) subunit of succinate dehydrogenase (SDHA1), significantly differ between Mφ3 and Mφ4 clusters, but comparable between Mφ1 and Mφ2 clusters which have similar BAF60a expression level (Fig. 2.1 C). We next decoded the 4 macrophage clusters using a curated signature gene list derived from cross-referenced mice datasets[9]. The Mφ1 population with the highest average gene expression resembles Interferon-induced and inflammatory macrophages. Mφ1 and Mφ2 also have increased expression of foamy and

resident-like macrophage signatures. On the contrary, Mφ3 and Mφ4, which comprise about one-fourth of the population, despite comparable expression levels of common macrophage markers such as CD68 and LGALS3, have less genetic similarity to the above major macrophage populations seen in mice plaque but are well characterized by mitochondria gene levels, likely suggesting differences in energy metabolic processes (Fig. 2.1 D).

To further resolve the biological and technical variability due to limits in sample size, we performed deconvolution on 126 bulk human plaque microarray samples from the Biobank of Karolinska Endarterectomy (BiKE) using space normalized single-cell gene expression as the signature matrix[159]. Mφ1 and Mφ2 are mixed as Mac(M), Mφ3 is renamed Mac(L), and Mφ4 to Mac(H). We observed a significant correlation between BAF60a, and Mac(L), Mac(H) populations (Fig. 2.1 E).

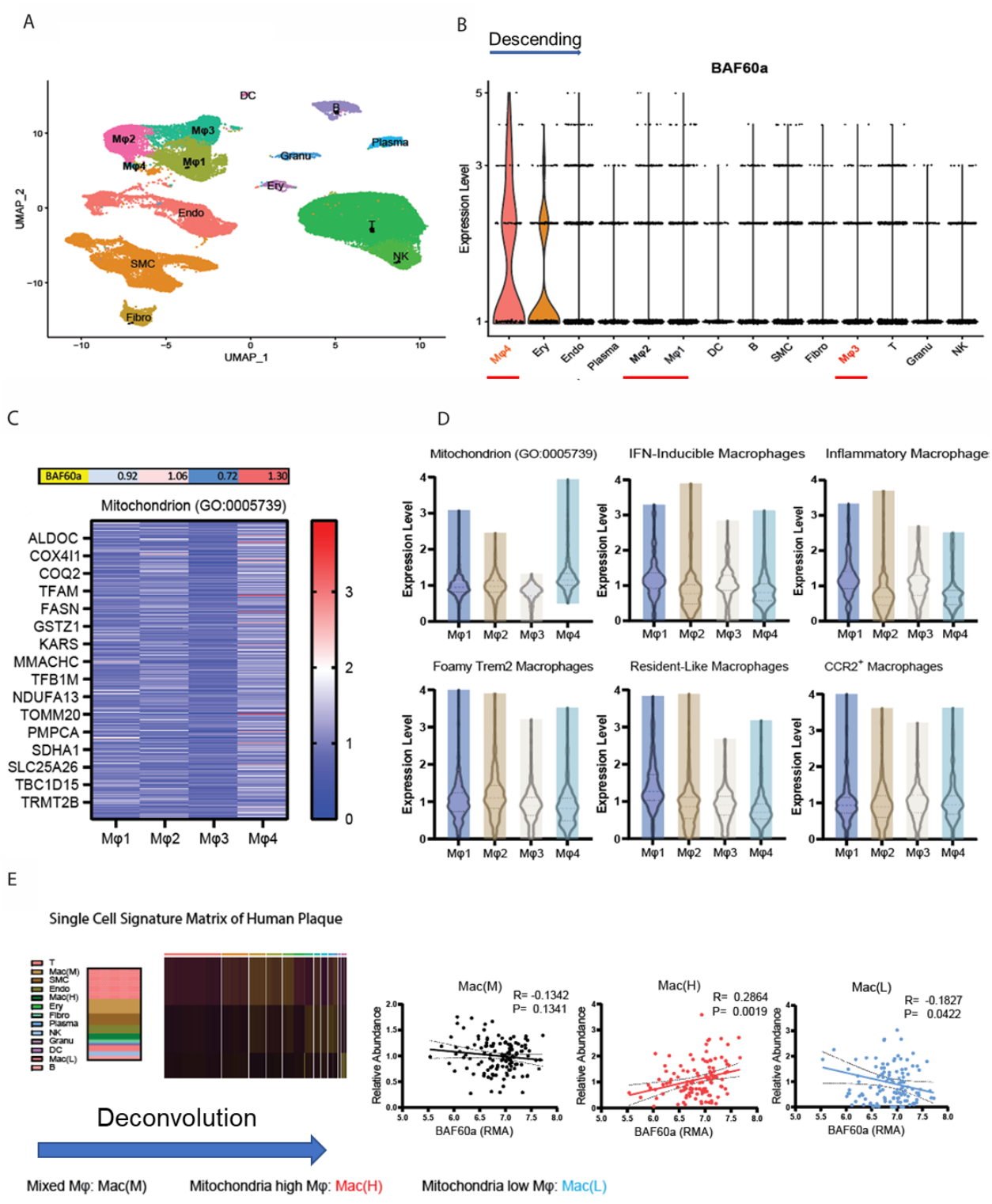

A
DC
B
Mφ2
Mφ3
Plasma
Granu
Mφ4
Mφ1
Ery
Endo
T
NK
SMC
Fibro
UMAP_2
UMAP_1
B
Descending
BAF60a
Expression Level
Mφ4
Ery
Endo
Plasma
Mφ2
Mφ1
DC
B
SMC
Fibro
Mφ3
T
Granu
NK
C
BAF60a
0.92
1.06
0.72
1.30
Mitochondrion (GO:0005739)
ALDOC
COX4I1
COQ2
TFAM
FASN
GSTZ1
KARS
MMACHC
TFB1M
NDUFA13
TOMM20
PMPCA
SDHA1
SLC25A26
TBC1D15
TRMT2B
Mφ1
Mφ2
Mφ3
Mφ4
D
Mitochondrion (GO:0005739)
IFN-Inducible Macrophages
Inflammatory Macrophage
Foamy Trem2 Macrophages
Resident-Like Macrophages
CCR2+ Macrophages
Expression Level
E
Single Cell Signature Matrix of Human Plaque
T
Mac(M)
SMC
Endo
Mac(H)
Ery
Fibro
Plasma
NK
Granu
DC
Mac(L)
B
Deconvolution
Mac(M)
R= -0.1342
P= 0.1341
Mac(H)
R= 0.2864
P= 0.0019
Mac(L)
R= -0.1827
P= 0.0422
Relative Abundance
BAF60a (RMA)
Mixed Mφ: Mac(M)
Mitochondria high Mφ: Mac(H)
Mitochondria low Mφ: Mac(L)

Figure 2.1 BAF60a positively correlates with mitochondria-high macrophages in human plaques

A, Uniform Manifold Approximation and Projection (UMAP) plot of different cell types in human plaque scRNA-seq (GSE159677). B, Violin plot of BAF60a expression in different cell clusters in decreasing order. C, Heatmap of normalized gene expression within Mitochondrion (GO:0005739) in Mφ1 to Mφ4 subtypes. D, Violin plot of gene expression under known gene lists in Mφ1 to Mφ4 subtypes. E, Illustration of bulk plaque sequencing deconvolution followed by Pearson r correlation analysis (N=126).

2.3.2 BAF60a is downregulated in murine atherosclerotic macrophages

To examine whether BAF60a changes dynamically upon atherosclerosis development, we fed ApoE$^{-/-}$ mice a high-cholesterol Western diet (WD) for 8 or 16 weeks to induce hypercholesterolemia and atherosclerosis formation. Single aortic cells were isolated by FACS, followed by total RNA extraction and quantitative PCR (Fig. 2.2 A). Single aortic cells from WD-fed ApoE deficient mice atherosclerosis model showed drastically decreased BAF60a in CD45 and Gelactin-3 (LGALS3, Mac2) double-positive macrophage populations during 16-week advanced atherosclerosis compared to 8-week. At the same time, no difference in BAF60a level was observed in mixed aortic cell populations or non-macrophage pan-leukocytes (Fig. 2.2 B). Results combined with section 2.3.1, suggest the potential of a dynamic BAF60a, mitochondria function interaction, and macrophage population changes under the atherosclerosis environment that should be investigated further.

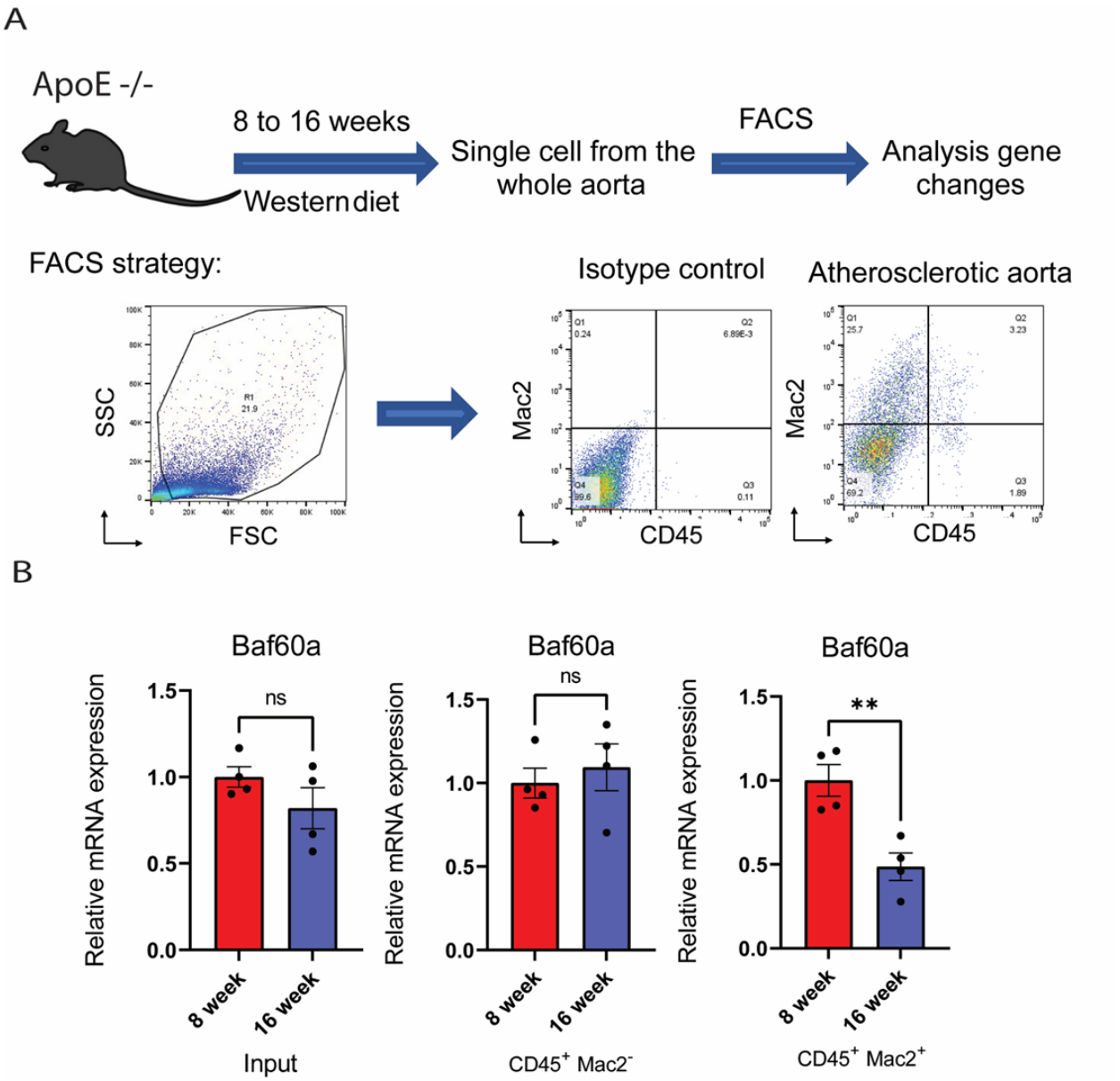


Figure 2.2 BAF60a is reduced in mouse atherosclerotic macrophages.

A, FACS isolation of single aortic cells from atherosclerotic mice model 8- (N=4) or 16- (N=4) weeks post-feeding. B, qPCR measurement of relative mRNA abundance for Baf60a (N=4). Data are presented as mean±SEM. In addition, the student's t-test was performed for B.

2.3.3 Myeloid BAF60a deficiency exacerbates atherosclerosis in ApoE$^{-/-}$ mice

To evaluate the role of BAF60a in macrophage and atherosclerosis, we first generated myeloid-specific Baf60a knockout mice (Baf60a^{mKO}) by crossbreeding Baf60a floxed mice (Baf60a$^{f/f}$) with Lyz2Cre mice, and then crossed to the ApoE$^{-/-}$ mice to obtain the Baf60a^{mKO}/ApoE$^{-/-}$ and Baf60a$^{f/f}$/ApoE$^{-/-}$(littermate control) mice (Fig. 2.3 A). We confirmed the deficiency of BAF60a in bone marrow-derived macrophages (BMDMs) while also observing no alterations to other SWI/SNF complex components such as BAF155, BRD9, and BAF60b (Fig. 2.3 B-C). After 16 weeks on a WD, en face oil red O (ORO) staining revealed an over 30% significant increase in atherosclerotic lesions in the aorta tree of male mice ($p = 0.0097$, Fig. 2.3 D-E). To identify whether cholesterol is responsible for the difference in the lesion. Fasting plasma was passed into FPLC, and further fractioned to 40 subfractions based on elution time. No changes in cholesterol content in very-low-density lipoprotein (VLDL), intermediate- and low-density lipoprotein (IDL/LDL), or high-density lipoprotein (HDL) were observed between the Baf60a^{mKO}/ApoE$^{-/-}$ and Baf60a$^{f/f}$/ApoE$^{-/-}$ group (Fig. 2.3 F).

We then quantified atherosclerosis in the aortic root region using hematoxylin/eosin (H&E), ORO, and immunofluorescence staining for macrophage content using Mac2 (Fig. 2.3 G). Significant increase in aortic root plaque area ($p=0.0123$) and macrophages ($p=0.0114$) were observed in Baf60a^{mKO}/ApoE$^{-/-}$ mice compared to Baf60a$^{f/f}$/ApoE$^{-/-}$ control (Fig. 2.3 H). At the same time, ELISA of plasma showed no difference in inflammatory cytokine MCP-1 and IL-6 levels ($p=0.7890$ and 0.9229, respectively, Fig. 2.3 I), suggesting unaltered systemic inflammation.

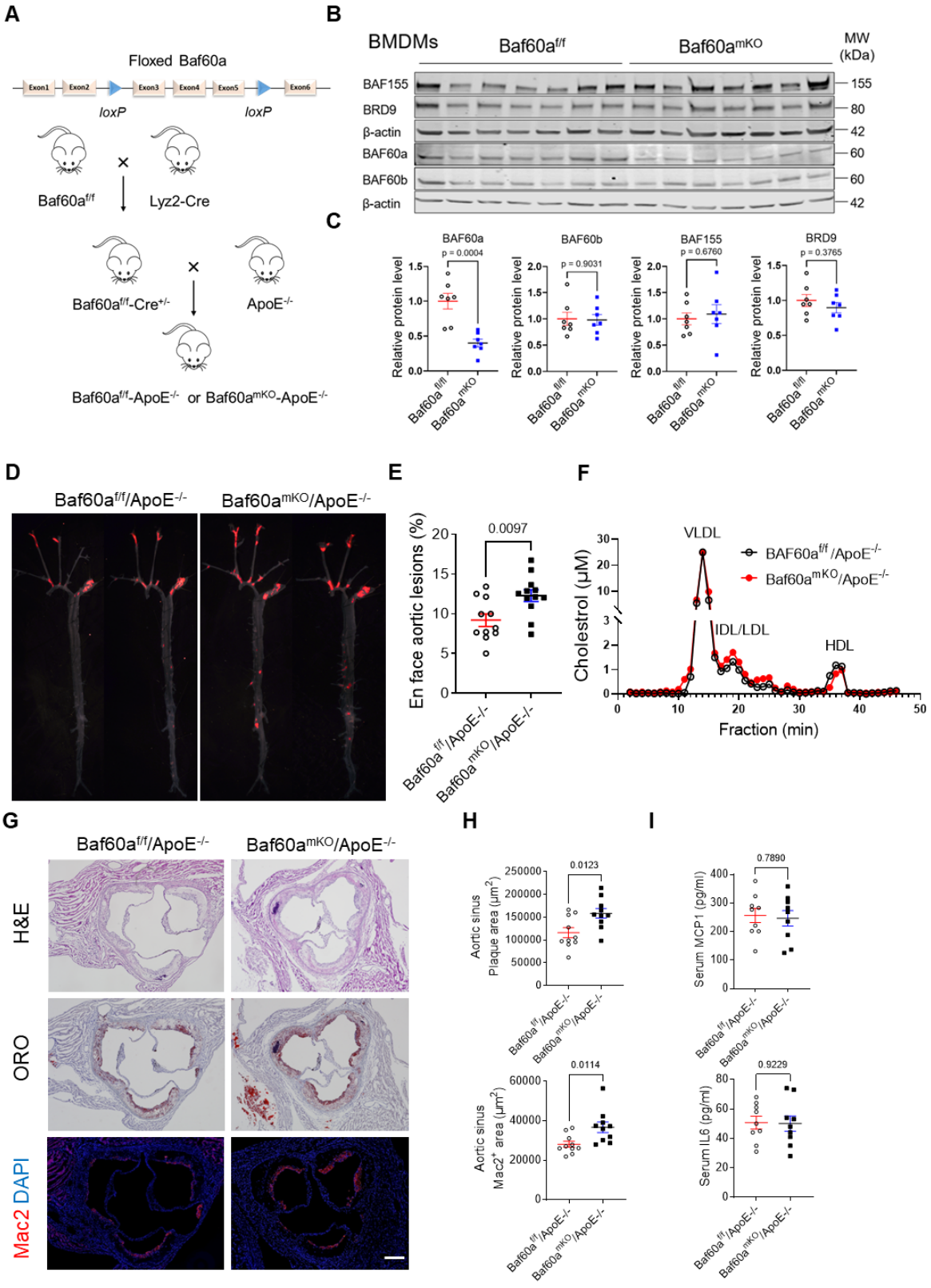

A
Floxed Baf60a
Exon1
Exon2
Exon3
Exon4
Exon5
Exon6
loxP
loxP
Baf60a f/f
Lyz2-Cre
Baf60a f/f-Cre+/-
ApoE-/-
Baf60a f/f-ApoE-/- or Baf60a mKO-ApoE-/-
B
BMDMs
Baf60a f/f
Baf60a mKO
MW (kDa)
BAF155
BRD9
β-actin
BAF60a
BAF60b
β-actin
155
80
42
60
60
42
C
BAF60a
p = 0.0004
BAF60b
p = 0.9031
BAF155
p = 0.6760
BRD9
p = 0.3765
Relative protein level
Baf60a f/f
Baf60a mKO
D
Baf60a f/f/ApoE-/-
Baf60a mKO/ApoE-/-
E
0.0097
En face aortic lesions (%)
Baf60a f/f/ApoE-/-
Baf60a mKO/ApoE-/-
F
VLDL
IDL/LDL
HDL
BAF60a f/f /ApoE-/-
Baf60a mKO/ApoE-/-
Cholestrol (μM)
Fraction (min)
G
Baf60a f/f/ApoE-/-
Baf60a mKO/ApoE-/-
H&E
ORO
Mac2 DAPI
H
0.0123
Aortic sinus Plaque area (μm2)
0.0114
Aortic sinus Mac2+ area (μm2)
I
0.7890
Serum MCP1 (pg/ml)
0.9229
Serum IL6 (pg/ml)

Figure 2.3 Myeloid BAF60a deficiency exacerbates atherosclerosis in Apoe−/− mice

A, Schematic illustration of the strategy to generate $Baf60a^{mKO}/ApoE^{-/-}$ mice. B, Immunoblotting of BAF60a, BAF60b, BAF155, BRD9, and β-actin protein abundance in BMDMs isolated from $Baf60a^{mKO}$ (N=7) and $Baf60a^{f/f}$ mice (N=7), followed by quantification (C). D-I: Male $Baf60a^{mKO}/ApoE^{-/-}$ (N=12) and $Baf60a^{f/f}/ApoE^{-/-}$ (N=11) mice were fed a WD for 16 weeks. D, en face ORO staining of the aorta tree and quantification (E). F, FPLC followed by cholesterol measurement of pooled plasma. G, H&E, ORO, and Mac2 staining of the aortic root, followed by quantification (N=10/group, H). Scale bars, 200 μm. I, Plasma level of MCP1 and IL6 quantified by ELISA (N=9/group). Data are presented as mean±SEM. Student's t-test for C-E, H-I.

2.3.4 The effect of myeloid BAF60a in atherosclerosis is vascular-localized and sex-independent

Systemic metabolic changes affect atherosclerosis development[4]. Hence we measured the body weight and glucose level in 16-weeks WD fed Baf60a^{mKO}/ApoE$^{-/-}$ and Baf60a$^{f/f}$/ApoE$^{-/-}$ male mice. We observed no significant difference in body weight (p=0.1360, Fig. 2.4 A) or plasma glucose level (p=0.8944, Fig. 2.4 B). To test if adipose tissue-resident macrophage (ATM) or liver Kupffer cell (stellate macrophages) are also affected by BAF60a knockout, thus altering the metabolic profiling, frozen sections of liver and epididymal white adipose tissue (eWAT) were stained with H&E or F4/80 respectively. No difference were observed for lobular inflammation in liver (p=0.3706, Fig. 2.4 C) and Crown-like structure in eWAT (CLS, p=0.2469, Fig. 2.4 D) between the Baf60a^{mKO}/ApoE$^{-/-}$ and Baf60a$^{f/f}$/ApoE$^{-/-}$ group. Results suggest that during atherosclerosis, the effect of myeloid BAF60a is mainly localized to the vasculature. Sex differences widely appear in CVDs, influencing the disease's diagnosis, treatment, and outcome [160]. Using the female mice model with the same genetic background as the male atherosclerosis model, we confirmed that the detrimental effect of myeloid BAF60a deletion also exists in the female sex (Fig. 2.4 E-F).

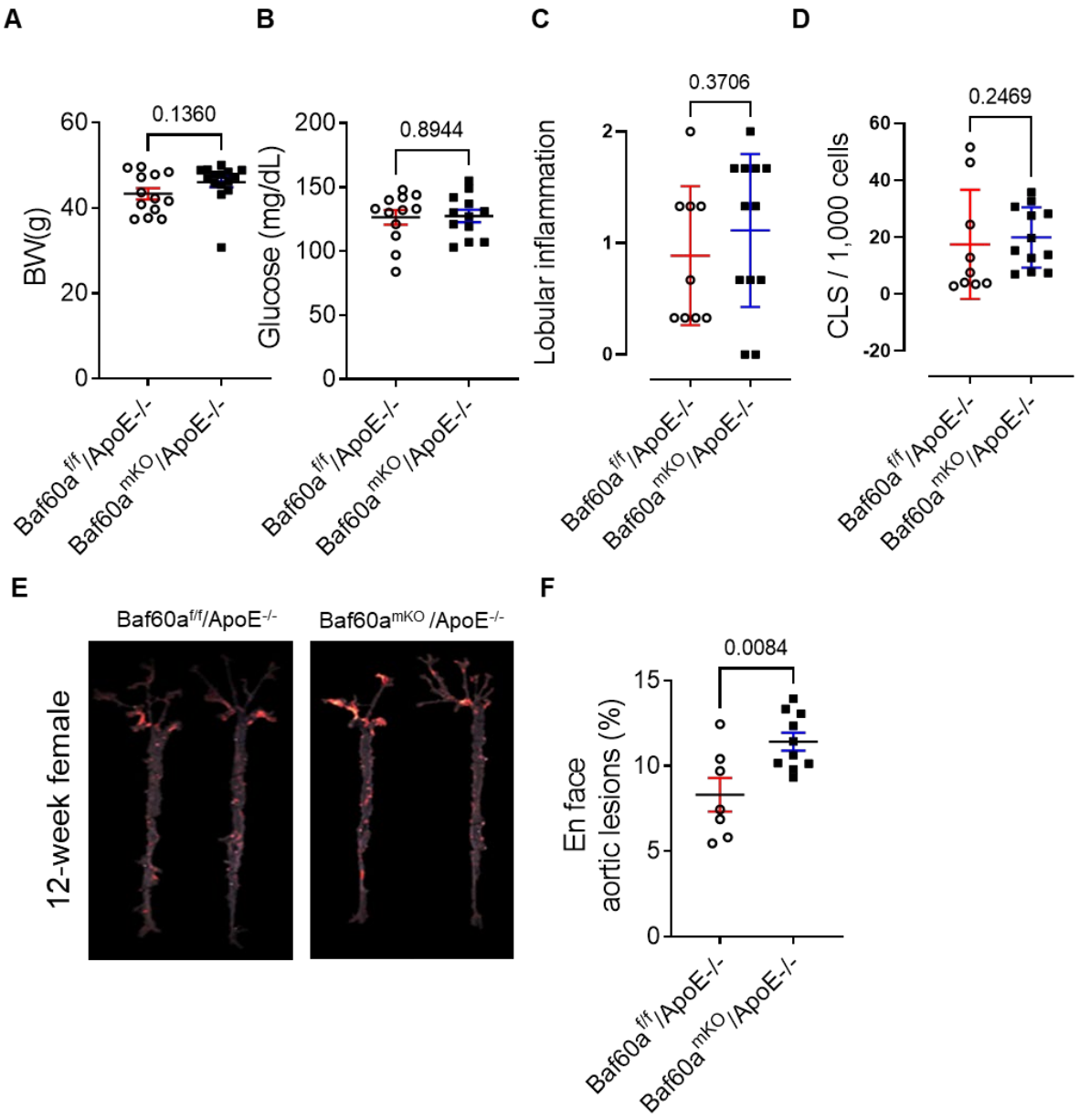


Figure 2.4 The effect of myeloid BAF60a in atherosclerosis is vascular-localized and sex-independent

A-D: Male Baf60a^{mKO}/ApoE$^{-/-}$ (N=15) and Baf60a$^{f/f}$/ApoE$^{-/-}$ (N=13) mice were fed a WD for 16 weeks. A, Body weight. B, Plasma Glucose. C, Liver lobular inflammation score based on the FLIP algorithm. D, Count of CLS per 1,000 cells in eWAT. E-F: Female Baf60a^{mKO}/ApoE$^{-/-}$ (N=10) and Baf60a$^{f/f}$/ApoE$^{-/-}$ (N=7) mice were fed a WD for 12 weeks. E, en face ORO staining of the aorta tree and quantification (F). Data are presented as mean±SEM. Student's t-test for A-D, F.

2.3.5 BAF60a deletion enhances leukocyte recruitment in the vasculature

Increased inflammatory cell population at the plaque is a hallmark of atherosclerosis[119]. Flow cytometry analysis was performed on single cells isolated from the aortas to explore whether the detrimental effect of BAF60a knockout in atherosclerosis development is related to increased immune cell recruitment. Significant upregulation of CD45+ leukocytes was identified in the Baf60a^{mKO}/ApoE$^{-/-}$ group compared to the control (Fig. 2.5 A). We further gated the CD45+ leukocyte population based on the expression of membrane markers. Ly6G for neutrophils, CD11b and F4/80 for macrophages, CD19 for B cells, and CD3 for T cells. Among the leukocyte population above, macrophages showed the most significant increase between the Baf60a^{mKO}/ApoE$^{-/-}$ and Baf60a$^{f/f}$/ApoE$^{-/-}$ groups (Fig. 2.5 B). At the same time, systemic blood cell composition remains essentially the same (Table. 2.1).

Circulating monocytes significantly contribute to plaque macrophage increase[9]. Hence we tested if BAF60a influences monocyte adhesion. Knockdown of BAF60a in human monocyte cell line THP-1 (Fig. 2.5 C) significantly upregulates the expression of adhesion-related molecules, including ITGA4, ITGB1, ST3GAL3, and GLG1 (Fig. 2.5 D). Next, to mimic the inflammatory vascular condition, we pre-treated human aortic endothelial cells (HAECs) with TNFα (2ng/ml), 6h after, HAECs were washed with PBS and cultured in the growth medium for an additional 10h, followed by coculturing with Calcein AM stained THP-1 cell for 5h (Fig. 2.5 E). Knockdown of BAF60a significantly exacerbates monocyte adhesion to TNFα pre-stimulated HAECs ($p=0.0026$, Fig. 2.5 E-F). Intravital microscopy is widely used to study the blood cells and endothelium interaction in the mouse cremaster muscle in vivo[161]. We observed a significantly increased leukocyte adhesion and rolling on the vascular wall in LPS-injected

Baf60a^{mKO}/ApoE$^{-/-}$ mice compared to Baf60a$^{f/f}$/ApoE$^{-/-}$ group (Fig. 2.5 G). Data indicate that BAF60a deletion promotes leukocyte adhesion.

Group	WBC 10^3/μL	NEU 10^3/μL	LYM 10^3/μL	MONO 10^3/μL	EOS 10^3/μL	BAS 10^3/μL	RBC 10^3/μL	HGB g/dL	PLT 10^3/μL
Week 16 KO	8.66± 0.86	2.97± 0.65	3.645± 0.375	0.61± 0.04	0.875± 0.125	0.56± 0*	10.27± 0.12	15.9± 0.3	909± 33
Week 16 WT	5.79± 0.08	2.71± 0.07	1.66± 0.31	0.58± 0.24	0.5± 0.18	0.34± 0.04	10.205± 0.525	15.4± 0.4	1074± 56
Week 12 KO	7.27± 0.22	2.975± 0.205	2.29± 0.03	0.59± 0.01	0.82± 0.07	0.595± 0.045	9.995± 0.205	15.3± 0.2	886.5± 10.5
Week 12 WT	5.7± 0.41	2.335± 0.135	2.105± 0.045	0.38± 0.07	0.565± 0.125	0.315± 0.035	9.535± 0.425	14.75± 0.85	976± 200
Week 8 KO	5.44± 0.7	1.89± 0.15	2.31± 0.62	0.35± 0.06	0.515± 0.035	0.375± 0.025	10.51± 0.12*	16.15± 0.15	875± 12
Week 8 WT	4.06± 1.34	1.43± 0.39	1.65± 0.71	0.35± 0.08	0.39± 0.03	0.24± 0.13	9.715± 0.105	14.45± 0.35	1424± 151
Week 0 KO	2.645± 0.095	0.375± 0.015	2.13± 0.06	0.04± 0	0.08± 0.02	0.02± 0	9.345± 0.045	15.05± 0.15	520.5± 301.5
Week 0 WT	3.04± 0.68	0.505± 0.095	2.42± 0.59	0.06± 0	0.03± 0.01	0.025± 0.005	11.99± 0.64	18.6± 1	400.5± 164.5

Table 2.1 Complete blood count of Baf60a^{mKO}/ApoE$^{-/-}$ and Baf60a$^{f/f}$/ApoE$^{-/-}$ mice fed WD for different time points (N=3/group).

Data are presented as mean±SEM. *P<0.05. WBC, white blood cell; NEU, neutrophil; LYM, lymphocyte; MONO, monocyte; EOS, eosinophils; BAS, basophile; RBC, red blood cell; HGB, hemoglobin; PLT, platelets.

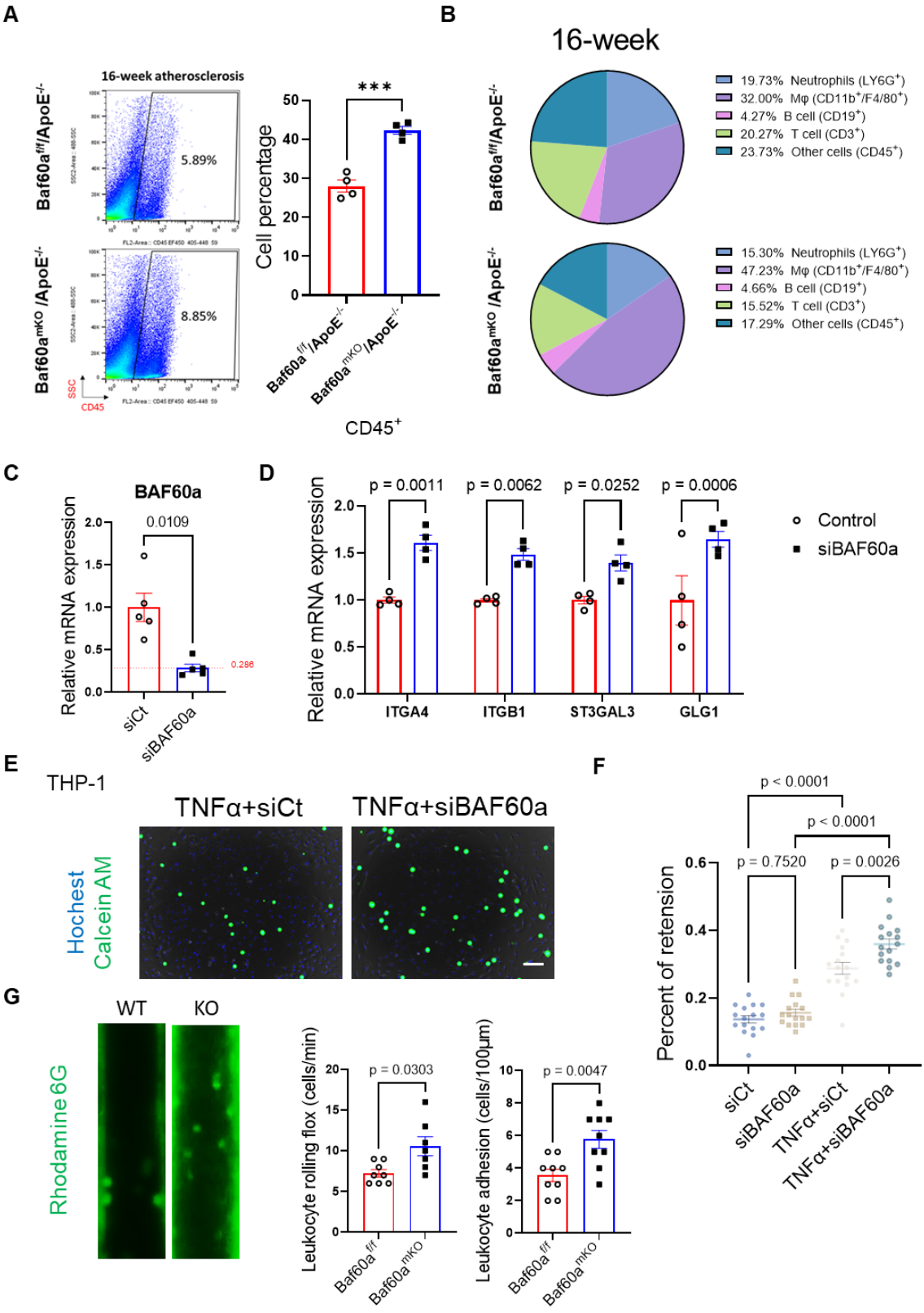

A
16-week atherosclerosis
Baf60a f/f/ApoE-/-
Baf60a mKO /ApoE-/-
5.89%
8.85%
SSC
CD45
Cell percentage
***
Baf60a f/f/ApoE-/-
Baf60a mKO/ApoE-/-
CD45+
B
16-week
Baf60a f/f/ApoE-/-
19.73% Neutrophils (LY6G+)
32.00% Mφ (CD11b+/F4/80+)
4.27% B cell (CD19+)
20.27% T cell (CD3+)
23.73% Other cells (CD45+)
Baf60a mKO /ApoE-/-
15.30% Neutrophils (LY6G+)
47.23% Mφ (CD11b+/F4/80+)
4.66% B cell (CD19+)
15.52% T cell (CD3+)
17.29% Other cells (CD45+)
C
BAF60a
0.0109
0.286
Relative mRNA expression
siCt
siBAF60a
D
p = 0.0011
p = 0.0062
p = 0.0252
p = 0.0006
Relative mRNA expression
ITGA4
ITGB1
ST3GAL3
GLG1
Control
siBAF60a
E
THP-1
TNFα+siCt
TNFα+siBAF60a
Hochest
Calcein AM
F
p < 0.0001
p < 0.0001
p = 0.7520
p = 0.0026
Percent of retension
siCt
siBAF60a
TNFα+siCt
TNFα+siBAF60a
G
WT
KO
Rhodamine 6G
Leukocyte rolling flox (cells/min)
p = 0.0303
Baf60a f/f
Baf60a mKO
Leukocyte adhesion (cells/100μm)
p = 0.0047
Baf60a f/f
Baf60a mKO

Figure 2.5 BAF60a deletion enhances leukocyte recruitment in the vasculature

A-B, Male Baf60a^{mKO}/ApoE$^{-/-}$ (N=4) and Baf60a$^{f/f}$/ApoE$^{-/-}$ (N=4) mice were fed a WD for 16 weeks. Single cells were isolated by FACS. A. Representative dot plots and quantification of CD45+ leukocytes population. B, Piechart of various leukocytes composition in the aorta. C, qPCR showing BAF60a knockdown efficiency in THP-1 cells. n=5. D, qPCR measurement of adhesion-related gene expression in control and siBAF60a THP-1 cells (n=4). E, Representative figure of Calcein AM stained THP-1 cell attached to HAECs and quantification (F), n=16. Scale bar=50 μm. G, Male Baf60a^{mKO} mice, and Baf60a$^{f/f}$ mice were IP injected with 50 μg/kg LPS. Rhodamine 6G was used for staining. Leukocyte adhesion and rolling were observed under an intravital microscope (N=9). Data are presented as mean±SEM. Student's t-test for A, C, and G. Two-way ANOVA followed by Holm-Sidak post hoc analysis for D and F.

2.3.6 BAF60a deficiency does not affect foam cell formation in vitro

Foam cells are lipid-laden macrophages. They are crucial to the development of atherosclerosis. Specifically, the creation and accumulation of foam cells in the subendothelial region of a damaged artery are one of the earliest steps in the progression of atherosclerosis[162]. BAF60a deficiency BMDM showed no difference in the expression of lipid uptake and export genes such as CD36, OLR1, LDLR, ABCA1, or ABCG1 (Fig. 2.6 A). In addition, the oxLDL uptake assay using Dil-labeled oxLDL (50µg/ml) showed no time-dependent difference in lipid uptake between the Baf60a^{mKO} and Baf60a$^{f/f}$ BMDMs (Fig. 2.6 B). Meanwhile, LipidTox staining of oxLDL uptake displayed no dose-dependent alterations in lipid uptake by BAF60a knockout (Fig. 2.6 C-D), further suggesting that BAF60a does not affect foam cell formation.

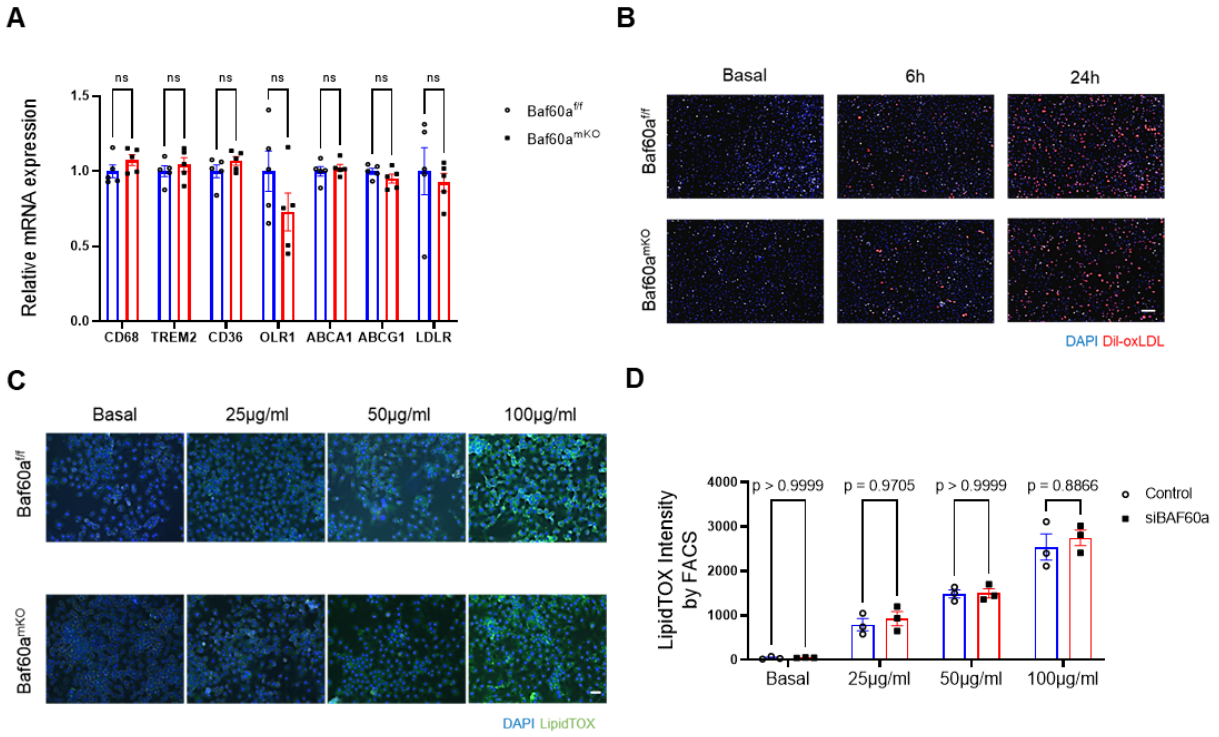


Figure 2.6 BAF60a deficiency does not affect foam cell formation in vitro

A, Total RNA was extracted from Baf60a^{mKO} and Baf60a$^{f/f}$ BMDMs (n=5 for each group). qPCR was performed to quantify specific gene expression. B, Dil-labeled oxLDL uptake by BMDMs at 0, 6, and 24h, followed by fixation and DAPI staining. Scale bar=50 μm. C, Dose-dependent oxLDL update by BMDMs followed by fixation and staining of DAPI and LipidTOX. Scale bar=50 μm. D. FACS quantification of dose-dependent oxLDL uptake in LipidTOX stained BMDMs. Data are presented as mean±SEM. Two-way ANOVA followed by Holm-Sidak post hoc analysis for A and D.

2.3.7 BAF60a deficiency in macrophages induces mitochondria dysfunction

As the vital organelle for OXPHOS to fuel critical cellular functions, mitochondria dysfunction in macrophages directly promotes atherosclerotic plaque formation[7, 134, 137, 138, 140, 149]. As we uncovered the significant positive association of high mitochondrial macrophage and BAF60a expression level in human atherosclerotic plaques, we hypothesized that such a correlation also exists and is the underlying mechanism driving aggravated plaque formation in BAF60a deficiency mice. Functionally, this is evidenced by the decreased maximum oxygen consumption rate (OCR) in oxLDL (50μg/ml, 48h) treated Baf60a^{mKO} BMDMs (Fig. 2.7 A). Furthermore, direct measurement of mitochondria copy number by qPCR showed a decrease in both bone marrow-derived monocytes (Day5, $p=0.008$, Fig. 2.7 B) and macrophages (Day 9, $p=0.0016$, Fig. 2.7 B) upon BAF60a knockout compared to control. The same phenomenon was observed in MACS-sorted F4/80+ aortic macrophages from the atherosclerotic mice model (Fig. 2.7 C-D). Visually, transmission electron microscopy (TEM) analysis of oxLDL-treated BAF60a deficiency showed structurally increased features of autophagosome containing damaged mitochondria in oxLDL-treated BAF60a deficiency BMDMs (Fig. 2.7 E). In addition, we confirmed a decreased abundance of essential proteins responsible for maintaining mitochondrial function (Fig. 2.7 F), including mitochondrial transcription factor A (TFAM, mtTFA, $p<0.0001$), Cytochrome c oxidase (COX IV, $p=0.0174$), and pyruvate dehydrogenase complex (PDH, $p=0.0425$) in oxLDL treated BAF60a deficiency BMDMs (Fig. 2.7 G). Moreover, as a result, increased reactive oxygen species (ROS) leakage from damaged mitochondria (Fig. 2.7 H-I).

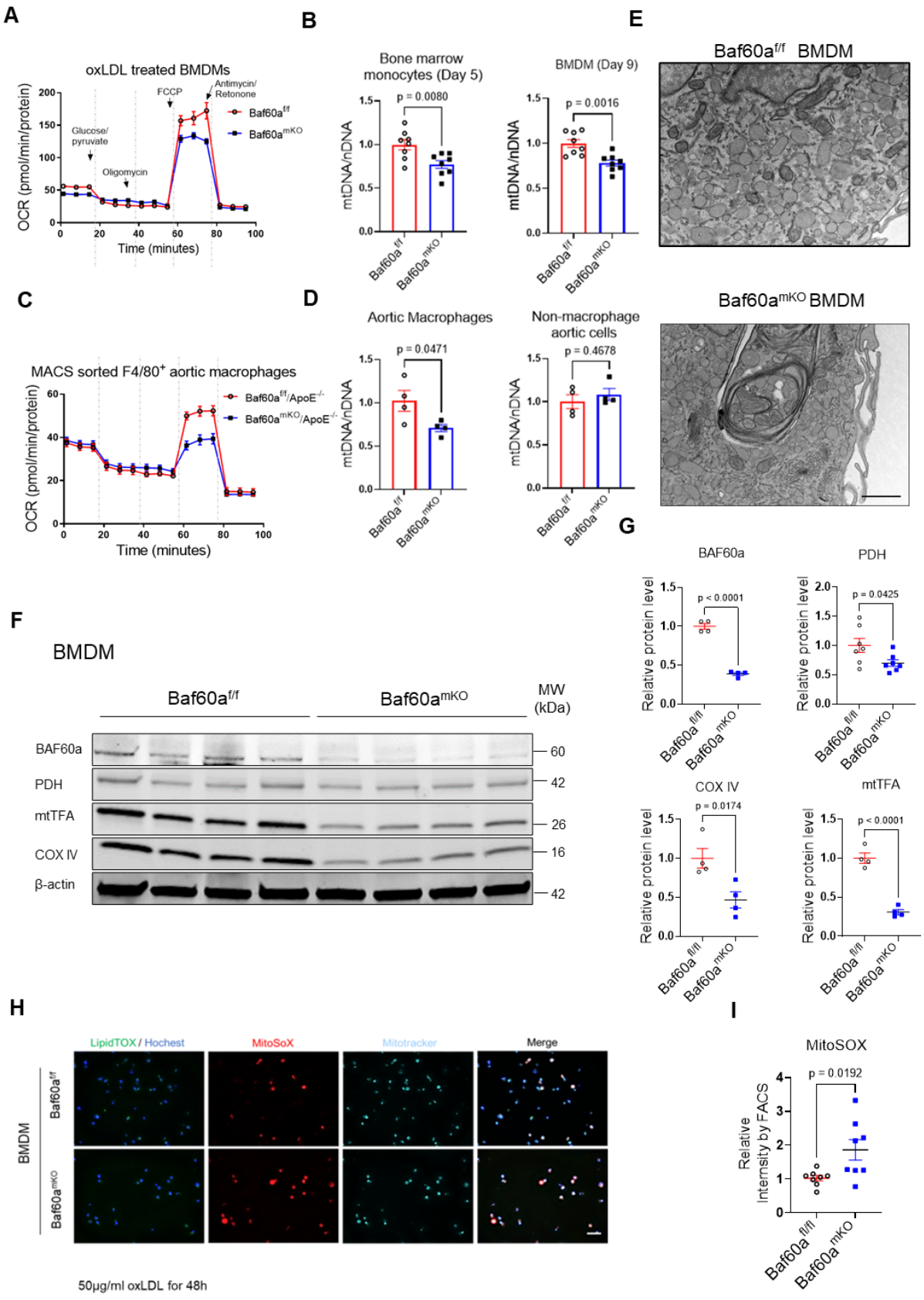

A
oxLDL treated BMDMs
OCR (pmol/min/protein)
Time (minutes)
Glucose/ pyruvate
Oligomycin
FCCP
Antimycin/ Retonone
Baf60a f/f
Baf60a mKO
B
Bone marrow monocytes (Day 5)
p = 0.0080
BMDM (Day 9)
p = 0.0016
mtDNA/nDNA
C
MACS sorted F4/80+ aortic macrophages
Baf60a f/f/ApoE-/-
Baf60a mKO/ApoE-/-
D
Aortic Macrophages
p = 0.0471
Non-macrophage aortic cells
p = 0.4678
E
Baf60a f/f BMDM
Baf60a mKO BMDM
F
BMDM
Baf60a f/f
Baf60a mKO
MW (kDa)
BAF60a
PDH
mtTFA
COX IV
β-actin
60
42
26
16
42
G
BAF60a
p < 0.0001
PDH
p = 0.0425
COX IV
p = 0.0174
mtTFA
p < 0.0001
Relative protein level
H
LipidTOX / Hochest
MitoSoX
Mitotracker
Merge
BMDM
50μg/ml oxLDL for 48h
I
MitoSOX
p = 0.0192
Relative Intensity by FACS

Figure 2.7 BAF60a deficiency in macrophages induces mitochondria dysfunction

A, Seahorse assay of OCR measured in Baf60a^{mKO} and Baf60a$^{f/f}$ BMDMs treated with oxLDL (50μg/ml, 48h). B, Mitochondrial DNA (mtDNA) normalized to nuclear DNA (nDNA) was measured in Baf60a^{mKO} and Baf60a$^{f/f}$ BMDMs treated with oxLDL(n=8/group). C, Seahorse assay of OCR measured in F4/80+ aortic macrophage from 16-week WD fed Baf60a^{mKO}/ApoE$^{-/-}$ and Baf60a$^{f/f}$/ApoE$^{-/-}$ mice (N=4), and quantification of mtDNA/nDNA ratio (D). E-I: BMDMs from Baf60a^{mKO} and Baf60a$^{f/f}$ mice were treated with oxLDL (50μg/ml, 48h). E, TEM illustration of subcellular structural changes (5,000 X). F, Immunoblotting of BAF60a, PDH, mtTFA, COX IV and β-actin protein abundance in BMDMs, followed by quantification (G, n=4-7/group). H, Immunofluorescence illustration of BMDMs stained with LipidTox, MitoSoX, and MitoTracker, followed by FACS quantification (I, n=8/group). Scale bar=50 μm.
Data are presented as mean±SEM. Student's t-test for B, D, G and I.

2.3.8 Environmental cue links BAF60a deficiency to mitochondria dysfunction, cell toxicity and apoptosis

Modified lipoproteins such as oxLDL contributed to the highly complex microenvironment of plaques[163]. We have demonstrated that BAF60a deficiency reduces mitochondria protein in the presence of oxLDL. Herein, we further concluded that oxLDL-induced atherosclerotic stress is required for BAF60a deficiency-mediated mitochondria dysfunction in BMDMs. Under basal level, the abundance of mitochondria proteins remains largely unaffected upon BAF60a deletion (Fig. 2.8 A), including mtTFA ($p=0.4622$), COX IV ($p=0.5804$), PDH ($p=0.2908$) and Nuclear Respiratory Factor 1 (NRF1, $p=0.9707$, Fig. 2.8 B). 7-keto cholesterol (7-KC) is the major oxysterol component of oxLDL, inducing macrophage damage and apoptosis during atherosclerosis[164, 165]. Upon exposure to 10μg/ml 7-KC for 24h, BMDMs from $Baf60a^{mKO}$ mice compared to $Baf60a^{f/f}$ control mice showed a higher level of cell apoptosis and damage-associated lactate dehydrogenase (LDH) release (Fig. 2.8 C). Likewise, MACS-sorted F4/80+ aortic macrophages from the $Baf60a^{mKO}/ApoE^{-/-}$ atherosclerotic mice model also showed higher pre-apoptotic cells compared to the cells from littermate control (Fig. 2.8 D). Co-staining of Mac2 and TUNEL of the sinus root region suggests BAF60a deficiency induces an increase in apoptosis signal, which overlaps with plaque macrophages (Fig. 2.8 E).

In addition, we found that adenovirus-mediated BAF60a overexpression rescued oxLDL induced reduction of mitochondria number ($p<0.0001$, Fig. 2.8 F), reduces ROS leakage ($p=0.0009$, Fig. 2.8 G), and prevents 7-KC induced cell toxicity and death in $Baf60a^{mKO}$ BMDMs (Fig. 2.8 H).

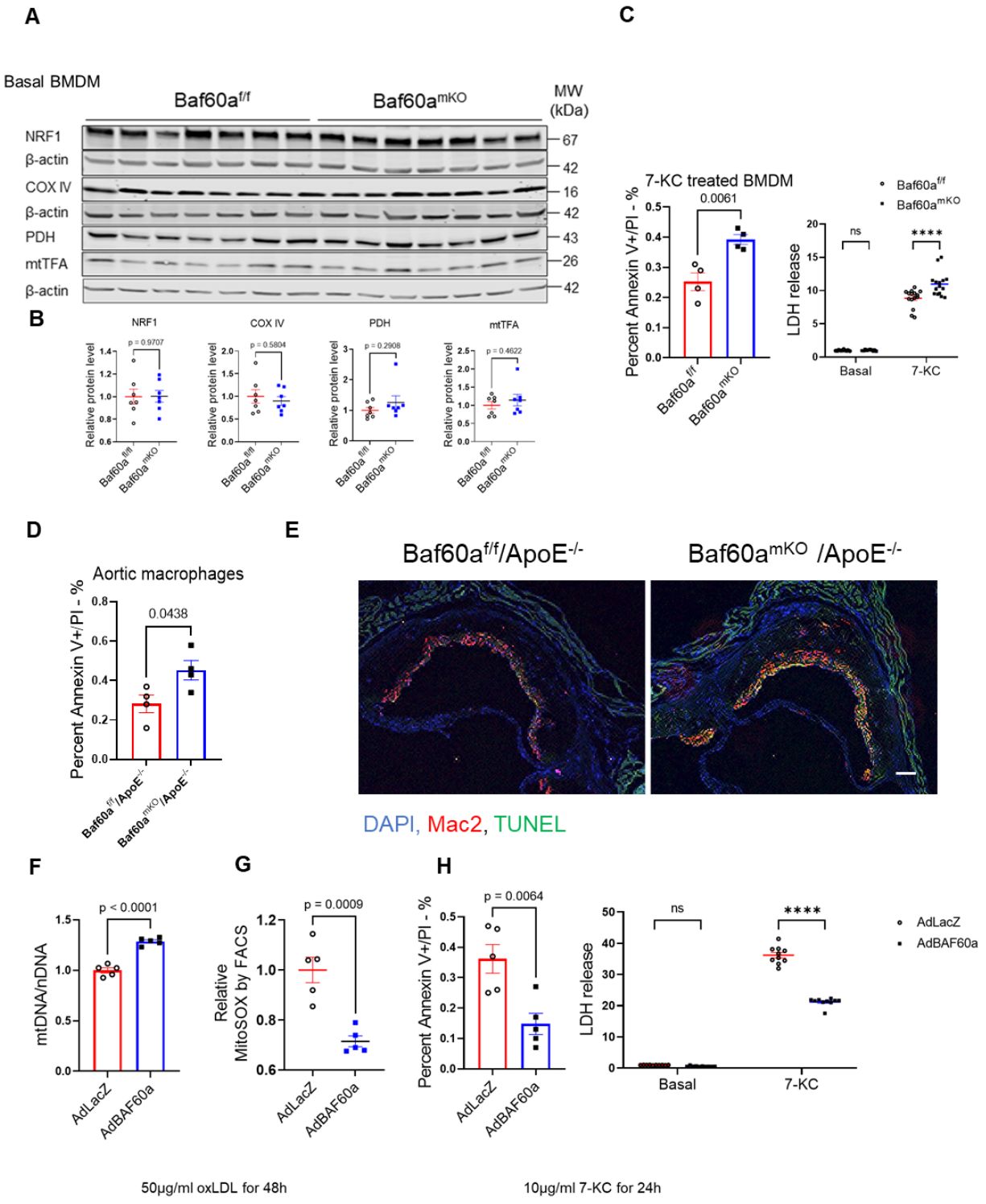

A
Basal BMDM
Baf60a f/f
Baf60a mKO
MW (kDa)
NRF1
β-actin
COX IV
β-actin
PDH
mtTFA
β-actin
67
42
16
42
43
26
42
B
NRF1
COX IV
PDH
mtTFA
Relative protein level
p = 0.9707
p = 0.5804
p = 0.2908
p = 0.4622
Baf60a f/f
Baf60a mKO
C
7-KC treated BMDM
Percent Annexin V+/PI - %
0.0061
LDH release
ns
****
Basal
7-KC
D
Aortic macrophages
Percent Annexin V+/PI - %
0.0438
E
Baf60a f/f/ApoE -/-
Baf60a mKO /ApoE -/-
DAPI, Mac2, TUNEL
F
mtDNA/nDNA
p < 0.0001
AdLacZ
AdBAF60a
G
Relative MitoSOX by FACS
p = 0.0009
H
Percent Annexin V+/PI - %
p = 0.0064
LDH release
ns
****
AdLacZ
AdBAF60a
Basal
7-KC
50μg/ml oxLDL for 48h
10μg/ml 7-KC for 24h

Figure 2.8 Environmental cue links BAF60a deficiency to mitochondria dysfunction, cell toxicity and apoptosis

A, Immunoblotting of NRF1, TOM20, COX IV, PDH, mtTFA, and β-actin protein abundance in BMDMs, followed by quantification (B, n=7/group). The bottom two β-actin bands correspond to the reused membrane from Fig 2.3. C, 7-KC treated BMDMs from Baf60a^{mKO} and Baf60a$^{f/f}$ mice were stained for Annexin V/PI to quantify apoptotic cell number (n=4/group) and measure LDH releases for cytotoxicity quantification (n=15/group). D, Annexin V/PI staining and quantification of MACS sorted F4/80+ aortic macrophages from 16-week WD fed Baf60a^{mKO}/ApoE$^{-/-}$ and Baf60a$^{f/f}$/ApoE$^{-/-}$ mice (N=4). E, Immunofluorescence illustration of aortic sinus from 16-week WD fed Baf60a^{mKO}/ApoE$^{-/-}$ and Baf60a$^{f/f}$/ApoE$^{-/-}$ mice co-stained with DAPI, Mac2 and TUNEL. Scale bars, 100 μm. F-G: BMDMs from Baf60a^{mKO} mice treated with oxLDL for oxLDL (50μg/ml, 48h) with or without adenovirus-mediated BAF60a overexpression. F, quantification of mtDNA to nDNA ratio (n=5/group). G, quantification of MitoSOX level by FACS (n=5/group). H, 7-KC treated BMDMs from Baf60a^{mKO} with or without BAF60a overexpression were stained for Annexin V/PI to quantify apoptotic cell number (n=5/group) and measure LDH releases for cytotoxicity quantification (n=10/group). Data are presented as mean±SEM. Student's t-test for B-H.

2.3.9 Loss BAF60a disrupts NRF1 accessibility at key mitochondria genes while NRF1 overexpression reverses mitochondria dysfunction

BAF60a is known to interact with TFs, recruiting the SWI/SNF complex to enable chromatin accessibility at specific gene loci[153]. To identify the molecular mechanism underlying BAF60a deficiency-mediated mitochondria dysfunction, we performed transposase-accessible chromatin using sequencing (ATAC-seq) on nuclei isolated from oxLDL-treated BMDMs from $Baf60a^{mKO}$ and $Baf60a^{f/f}$ mice. HOMER transcription motif enrichment analysis identified a significant underrepresentation of NRF1 in the BAF60a KO BMDMs compared to the control (Fig. 2.9 A). This is further confirmed by a drop in transcription factor footprint near the NRF1 binding motif ($p<0.0001$, Fig. 2.9 B-D). Furthermore, decreased chromatin accessibility was observed in NRF1 targeted genes such as TFAM and TFB1M upon BAF60a deficiency (Fig. 2.9 E). In addition, BAF60a deficiency in oxLDL-treated BMDM significantly suppressed the expression of NRF1-regulated mitochondria genes, such as TFAM, TFB1M, TFB2M, HSPD1, PDHA1 (Fig. 2.9 F). Co-IP of HA-NRF1 overexpressed RAW 264.1 macrophages suggest a direct physical interaction between the NRF1 and BAF60a (Fig. 2.9 G). Consequently, overexpression of NRF1 in BAF60a knockdown RAW264.1 macrophages significantly rescued oxLDL-induced decrease in mitochondrial protein abundance (Fig. 2.9 H-I). An increased mitochondria copy number also confirms functional protection of NRF1 overexpression in BAF60a knockdown cells under oxLDL stress (Fig. 2.9 J).

In conclusion, results suggest a direct role of BAF60a in maintaining mitochondria function by interacting with NRF1 to promote chromatin accessibility at key mitochondria genes. Such interaction is disrupted during atherosclerosis, in which BAF60a expression is reduced in

stress-associated aortic macrophages. The dysregulated mitochondrial function can be rescued by overexpression of BAF60a or NRF1.

A

Motif	Name	Percent of WT	Percent of KO	P-value
	NRF1	1.49%	1.01%	1.00E-49

Figure 2.9 Loss BAF60a disrupts NRF1 accessibility at key mitochondria genes while NRF1 overexpression reverses mitochondria dysfunction

A-F: OxLDL-treated BMDMs from Baf60a^{mKO} and Baf60a$^{f/f}$ mice. A, HOMER motif analysis of ATAC-seq motifs from WT and KO group (n=2/group). B, Transcription footprint analysis by HINT-ATAC using ATAC-seq motifs from WT and KO group, followed by quantification of peak occupancy within 100bp of the TF binding site (C). D. Top downregulated transcription factor activities. E, Normalized ATAC-seq reads around TFAM and TFB1M gene in WT and KO group shown in IGV. F, qPCR of NRF1-related gene expression (n=3/group). G, Co-IP of physical interaction between NRF1 and BAF60a in HA-NRF1 overexpressed RAW 264.1 cells. IgG was used as a negative control. H-J: From left to right, RAW264.1 cells treated with or without oxLDL, with siCt or siBAF60a, and overexpressed with or without NRF1 overexpression. H, immunoblotting of NRF1, PDH, mtTFA, COX IV and β-actin protein abundance. I, quantification of (H), n=4/group. J, mtDNA to nDNA ratio quantified by qPCR. Data are presented as mean±SEM. Student's t-test for C, I. Two-way ANOVA followed by Holm-Sidak post hoc analysis for F, J.

2.4 Discussion

As a chronic progressive disease, the complex microenvironment of atherosclerotic plaque assigns drastic plasticity to the plaque macrophage population, with at least five subtypes of macrophages reported in humans[9]. Alterations in macrophage metabolism and epigenetic modification have individually been proposed to alter macrophage phenotype and are potentially associated with disease conditions. How epigenetic machinery crosstalk with macrophage mitochondria metabolic profile in the plaque remains elusive. Exclusive among all mSWI/SNF subunits, BAF60s are a link between the SWI/SNF complex and specific transcription machinery to regulate the expression of target genes[153]. In the present work, we showed that BAF60a, TF interacting subunit of the mammalian SWI/SNF chromatin remodeling complex, expression positively correlates with mitochondria high macrophage population in the human plaque and is downregulated during atherosclerosis in mice, pointing to the potential of a dynamic BAF60a, mitochondrial and macrophage population changes under atherosclerosis.

Myeloid BAF60a deletion exacerbates atherosclerosis plaque formation in male and female mice without altering systemic lipid and inflammatory profiles. Deleting BAF60a increased the expression of the adhesion-related protein in monocytes leading to increased recruitment to the vasculature without changing cell composition in circulation. In addition, foam cell, a signature of lipid-laden plaque macrophage, is not altered by BAF60a deficiency. At the same time, we reported robust mitochondrial dysfunction upon BAF60a deletion in vitro and in vivo through a series of functional, structural, and toxicity assays. We identified that mitochondrial dysfunction occurs when the cell senses the atherosclerotic environmental cues and further induces cell toxicity and apoptosis, which is known to advance plaque formation directly.

Inside the cell, existing mitochondria are constantly importing and integrating new lipids and amino acids as part of a dynamic intrinsic process to synthesize new mitochondria. In reaction to changes in their surrounding environment, mitochondria replicate mitochondrial DNA, fuse, and split. This system, which is carefully managed to maintain a functional mitochondrial network, is required for maintaining energy balance, metabolic signaling, and cell death[166]. The nuclear genes are responsible for the expression of the majority of the mitochondrial morphology and functionality proteins. These nuclear genes work with a group of transcriptional regulators that include NRF1[167]. Mechanistically, chromatin accessibility assay suggests that BAF60a deficiency reduces the transcription factor NRF1 binding to essential mitochondrial genes during atherosclerotic stress through a physical interaction between SWI/SNF subunits BAF60a and NRF1. Thus, while adenovirus-mediated BAF60a is protective, overexpression of the transcription factor NRF1 also functional compensate for the loss of BAF60a and mitochondria dysfunction. Given the highly context-dependent role of BAF60a in various disease conditions, identifying the downstream regulatory network of BAF60a provides an additional layer of therapeutic targets.

One limitation of the present work is that we did not wholly address how BAF60a deficiency macrophage corresponds to the five human plaque macrophage subtypes. Recent research suggested that BAF60a is decreased in the adipose tissue macrophage (ATM) of white adipose tissue (WAT) of diabetic mice, and its deficiency induces the M1 proinflammatory activation of ATM as a result of disrupted interaction between BAF60a and ATF3[91]. However, potentially owing to the complicated disease environment of atherosclerosis plaque, we found that in BAF60a deficiency, aortic macrophages, despite showing reduced OXPHOS, resemble neither classical activated M1 nor alternative activated M2 macrophage gene signature (data not

shown). How BAF60a affects the plaque macrophage population could be significantly benefited by future scRNA studies of the atherosclerotic aorta from BAF60a deficient mice.

In summary, we identified that BAF60a is required for macrophage mitochondrial energy homeostasis under pro-atherosclerotic stress by preserving NRF1 accessibility to essential nuclear mitochondrial genes in an SWI/SNF complex-dependent way. Furthermore, the disrupted connection between BAF60a and mitochondrial energy homeostasis in macrophages is an example of the epigenetic-metabolic interaction affected by the disease microenvironment, exposing new layers of atherosclerosis treatment targets (Fig. 2.10).

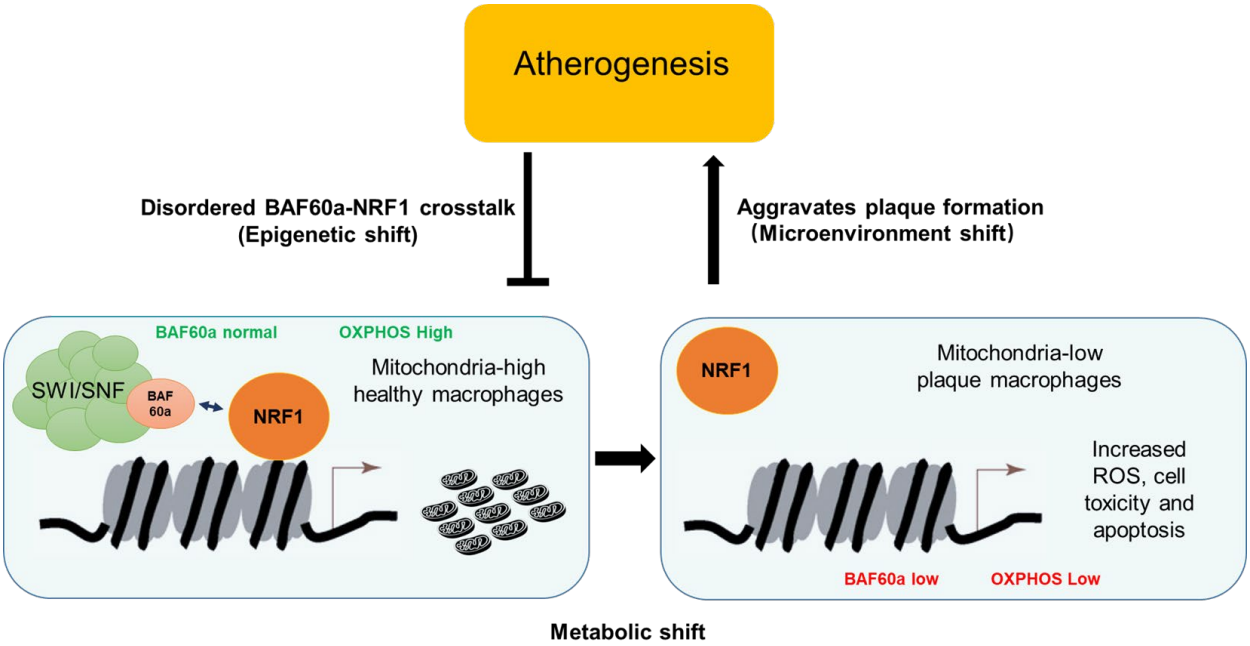


Figure 2.10 Schematic model of BAF60a regulation of macrophage mitochondria dysfunction and atherosclerosis.

Chapter 3 Investigates the Role of Smooth Muscle BAF60a in Abdominal Aortic Aneurysm

3.1 Acknowledgment

This chapter contains co-first author work previously published in the Arterioscler Thromb Vasc Biol. 2020 Oct;40(10):2494-2507.

Chang Z, Zhao G and Zhao Y obtained and analyzed the data. Lu H, Xiong W, Liang W, Sun J, Wang H, Zhu T, Rom O, Guo Y, Fan Y, Chang L, Yang B, Garcia-Barrio MT, Lin JD, Schopfer FJ, Freeman BA, and Tianqing Zhu provided technical and material support.

3.2 Introduction

Abdominal aortic aneurysm (AAA) affects more than 5% of men[168] and 1.3% of women over 65 years old[169] and is associated with a mortality rate of 50%-80% upon rupture. AAA is a focal dilation of the abdominal aorta to a diameter of over 30mm in humans and is primarily asymptomatic[170]. Although endovascular and open surgical repair can spare patients from fatal or severe outcomes, no medical therapy has been conclusively shown to prevent or treat AAA, partially due to the incomplete understanding of the molecular mechanisms of AAA development and progression.

Recent evidence has highlighted the importance of innate and adaptive immunity in the initiation and expansion of AAA[171]. As a hallmark of AAA, the intense transmural inflammatory response involves different kinds of cells constituting the vascular wall, including endothelial cells[172], VSMCs[173], and resident immune cells, along with a significant influx

of exogenous leukocytes to the media and adventitia[170, 171]. Furthermore, VSMC inflammatory response promotes vascular disease progression through enhanced secretion of pro-inflammatory cytokines, adhesion molecules, and proteolytic enzymes[174]. Nevertheless, the molecular biology of VSMC inflammation and its role in AAA development remains elusive.

As one of the four prominent families of chromatin remodeling proteins, it has been proposed that SWI/SNF complexes play a crucial role in the pathophysiology of several human disorders by regulating gene expression through chromatin accessibility modifications[43, 175]. SWI/SNF complexes comprise one of the two catalytic subunits, BRG1 or BRM, plus other subunits, known collectively as BAFs (BRG1/BRM associated factors)[82]. BAF60a, also known as SMARCD1, is one of the three 60-kDa subunits and recruits various transcription factors[85, 87, 176]. In vivo investigations reveal that BAF60a is essential for regulating hepatic fatty acid oxidation[87], constraining embryonic stem cell pluripotency networks[177], integrating circadian signals[178], and controlling systemic metabolic homeostasis[88]. A recent study has demonstrated that BAF60a deficiency in hepatocytes protected mice from diet-induced atherosclerosis[88], the first to link BAF60a with cardiovascular disease. Multiple microarray-based profiles of human gene expression revealed an increase of BAF60a in samples of AAA[176] and intracranial aneurysms[179] and intracranial aneurysms[180], suggesting a potential function for BAF60a in changing vascular homeostasis.

Through modulation of VSMC inflammation and the production of the proteolytic enzyme cathepsin S, the current work demonstrated a causal function for BAF60a-dependent chromatin remodeling in AAA formation. In two distinct mouse models, disruption of this mechanism by VSMC-specific deletion of BAF60a prevented the development of AAA. Our

findings improve the understanding of the epigenetic control of AAA and identify BAF60a as a promising therapeutic target for the prevention and treatment of the disease.

3.3 Materials and methods

3.3.1 Antibodies and reagents

BAF60a mouse antibody (#611728) was purchased from BD Biosciences (San Jose, CA). Rabbit antibodies for BAF60a (ab245222), BRG1 (ab110641), SM22α (ab10135), and Cathepsin S (ab92780) were from Abcam (Cambridge, UK). Antibodies against BAF155 (#11956), BAF170 (#12760), BAF47 (#91735), p65 (#8242), p-p65 (#3033), p-IKKα/β (#2697), lamin A/C (#2032), β-actin (rabbit mAb #4970 and mouse mAb #3700) were purchased from Cell Signaling Technology (CST, Danvers, MA). Antibodies against MMP2 (A11144) and MMP9 (A2095) were purchased from ABclonal (Woburn, MA). The antibody against Mac2 (#14-5301-82) was from eBioscience (San Diego, CA). GAPDH antibody (sc-365062) was from Santa Cruz Biotechnology (Santa Cruz, CA). Alexa Fluor® 680 AffiniPure Goat Anti-Mouse IgG, light chain specific antibody (#115-625-174), Alexa Fluor® 488 Streptavidin Conjugate antibody (#016-540-084), Alexa Fluor® 488-AffiniPure Donkey Anti-Mouse IgG (H+L) (#715-545-151), Alexa Fluor® 647 AffiniPure Donkey Anti-Rat IgG (H+L) (#712-605-153), and Alexa Fluor® 488-AffiniPure Donkey Anti-Rabbit IgG (H+L) (#711-545-152) were from Jackson ImmunoResearch (West Grove, PA). Recombinant human TNFα protein (# 210-TA) was from R&D Systems (Minneapolis, MN) and was used at 20 ng/ml to stimulate HASMCs.

3.3.2 Human patient aortic samples

Human aortic tissues from AAA patients or heart transplant donors were obtained from the Cardiovascular Health Improvement Project (CHIP) core of the Department of Cardiac Surgery at the University of Michigan with the Institutional Review Board approval (Hum00077616).

3.3.3 Animal procedures

BAF60a$^{f/f}$ mice in the C57BL/6J background were a kind gift from Dr. Jiandie Lin's lab at the University of Michigan, and the gene targeting strategy was described previously[88]. In brief, exons 3 to 5 of the mouse Baf60a gene were flanked with two loxP sites. SMMHC-CreERT2-BAF60a$^{f/f}$ mice were generated by crossbreeding female BAF60a$^{f/f}$ mice with male SMMHC-CreERT2 mice (the expression of CreERT2 is under control of the mouse smooth muscle myosin, heavy polypeptide 11 promoter/enhancer. The Jackson Laboratory, #019079). Since the SMMHC-CreERT2 transgene was inserted in the Y chromosome, only male smooth muscle cell-specific BAF60a knockout mice can be generated and thus were used in this study. A series of 5 days' intraperitoneal injections of tamoxifen (80 mg/kg/day, Sigma-Aldrich, #T5648) was given to the 6 to 8 weeks-old male SMMHC-CreERT2- BAF60a$^{f/f}$ mice and BAF60a$^{f/f}$ mice to generate VSMC-specific BAF60a knockout (BAF60a^{SMKO}) and floxed control (BAF60a$^{f/f}$) mice for the current study. Mice were allowed 9 days to clear the excess tamoxifen before further treatment.

The Angiotensin II (AngII)-induced murine AAA model was performed as previously described[181]. Briefly, 8- to 10-week-old male BAF60a$^{f/f}$ and BAF60a^{SMKO} mice or 10-week-old male C57BL/6J mice received 2×10^{11} genomic copies of AAV carrying gain-of-function mutation of mouse PCSK9 (AAV-Pcsk9.D377Y, hereafter AAV-Pcsk9) (Penn Vector Core at the University of Pennsylvania) by intraperitoneal injection and switched to a Western diet containing 0.2% cholesterol by mass (Harlan Teklad, #TD. 88137, Envigo, Hackensack, NJ) to induce hypercholesterolemia. Two weeks later, the BAF60a$^{f/f}$ and BAF60a^{SMKO} mice were subjected to subcutaneous implantation of osmotic mini-pumps (Alzet, Model #2004, Cupertino, CA) for delivery of AngII (Bachem, #H-1706, Vista, CA) at a releasing rate of 1,500 ng/kg/min

(or an equivalent volume of saline solution, as control). Two groups of wild-type C57BL/6J mice were also set up and subjected to the same protocol as above. In addition, systolic blood pressure was monitored weekly by tail cuff using the BP-2000 Blood Pressure Analysis System (Visitech, Cary, NC). After 28 days of AngII infusion, mice were euthanized and perfused with saline through the left ventricle to remove blood from the aorta after blood collection. The perivascular tissue of the aorta was carefully removed from the aortic wall under a dissection microscope. The maximal outer diameter of the suprarenal aorta was assessed with a digital caliper (Fisher Scientific, #14-648-17) as an average of three measurements in a double-blinded manner[182]. Suprarenal abdominal aortas with a maximal diameter >50% larger than their adjacent portion were considered abdominal aortic aneurysms. Ruptures that happened in the thoracic aorta were excluded from AAA incidence. Serum total cholesterol (TC) and triglyceride levels were measured by enzymatic kits (Wako Diagnostics, Osaka, Japan). Mice with TC levels less than 400mg/dl at termination were excluded from data analysis regardless of whether they had developed AAA. Serum MCP-1 and IL-6 levels were determined by ELISA at the Immunology Core at the University of Michigan.

The elastase-induced AAA model was performed as previously described[183, 184]. Ten to twelve weeks old male BAF60a$^{f/f}$ and BAF60a^{SMKO} mice or C57BL/6J mice were anesthetized by intraperitoneal injection of a mixture of ketamine (210 mg/kg) and xylazine (30 mg/kg). The infrarenal aorta was isolated and then surrounded with a sterile gauze soaked with 30μL elastase (MilliporeSigma, #E1250, lot#SLBV9311, 44 units/mL) or heat-inactivated elastase as the sham control. Elastase was removed 30 minutes later, and the abdominal cavity was washed twice with saline. BAF60a$^{f/f}$ and BAF60a^{SMKO} mice were euthanized 14 days after elastase exposure, and C57BL/6J mice in the AAA progression experiment were euthanized at 0,

7, or 14 days after elastase exposure. Mice were perfused with saline through the left ventricle to remove blood from the aorta after blood collection. The perivascular tissue of the aorta was carefully removed from the aortic wall under a dissection microscope. The maximal outer diameter of the infrarenal aorta was assessed with a digital caliper (ThermoFisher Scientific, #14-648-17) as an average of three measurements in a double-blinded manner. Infrarenal aortas with diameters more than 50% larger than the adjacent portion were considered abdominal aortic aneurysms. Serum TC, TG, MCP-1, and IL-6 were determined as described above.

All animal procedures were performed according to protocols approved by the Institutional Animal Care & Use Committee (IACUC) at the University of Michigan.

3.3.4 Immunostaining and immunohistochemistry

Human and murine aorta samples were fixed with 10% buffered formalin in PBS (Fisher Healthcare, #245685) and were then embedded in paraffin according to standard laboratory procedures after dehydration and processed at the In-Vivo Animal Core (IVAC) at the University of Michigan. Paraffin sections of human tissue (5 μm) were deparaffinized, rehydrated, and boiled in Citrate Buffer at pH 6.0 (Invitrogen, #00-5000) for epitope retrieval for 15 min. After blocking with 5% donkey serum in PBS at room temperature for 1 hour, sections were stained with primary antibody against SM22α (Abcam, ab10135, 1:100 dilution) or BAF60a (Abcam, ab245222, 1:100 dilution) at 4°C overnight. Next, sections were washed in PBS and incubated with Alexa Fluor conjugated secondary antibody (Jackson ImmunoResearch Laboratories). Finally, slides were mounted with ProLong™ Gold Antifade Mountant with DAPI (Invitrogen, #P36935) before taking pictures with an Olympus IX73 microscope.

Serial sections (5μm thick, 200μm apart) of mouse suprarenal abdominal aorta (AngII-induced AAA) and infrarenal aorta (elastase-induced AAA) were deparaffinized, rehydrated and

stained with Verhoeff Van Gieson's staining for elastic fibers (Electron Microscopy Sciences) according to the manufacturer's instructions. Based on the previous reports,[185] the standard for elastin degradation grade was set as: grade 1, less than 25% degradation; grade 2, 25% to 50% degradation; grade 3, 50% to 75% degradation; and grade 4, over 75% degradation. Six serial sections were analyzed for each aorta and the mean value was counted as the elastin degradation grade of this aorta. For Mac2 immunofluorescence staining, sections were stained with macrophage-specific antibody Mac2 (eBioscience, #14-5301-82, 1:150 dilution) after antigen retrieval. Quantification analysis of macrophage content indicated by the Mac2+ fraction was performed with Image J software, and an average number of 4 sections was calculated as the macrophage content of each aorta.

3.3.5 Flow cytometry analysis of murine aorta

BAF60A$^{f/f}$ and BAF60A^{SMKO} mice were euthanized after 28 days of AngII infusion or sham operation in the AngII model or 14 days after elastase treatment or sham operation in the elastase model. The aortas were perfused with PBS containing 2% heparin to remove excessive blood before being minced and digested in an enzymatic digestion solution containing 450 U/mL collagenase type I (Gibco, #17100-017), 125 U/mL collagenase type XI (Sigma-Aldrich, #C7657), 60 U/mL hyaluronidase type I-s (Sigma-Aldrich, #H3506) and 60 U/mL DNase-I (Roche, #10104159001) at 37°C for 60 minutes. Single cells were released using a 70μm cell strainer and stained with the indicated antibodies before performing flow cytometry analysis[186] on a MoFlo Astrios cell sorter (Beckman Coulter, Brea, CA). Antibodies used for flow cytometry: CD16/CD32 for Fc block (eBioscience, #14-0161-85), PE-conjugated isotype control (rat IgG2b kappa, Invitrogen, #12-4031-82), eFluor 450 isotype control (rat IgG2b kappa, eBioscience, #48-4031-82), APC conjugated isotype control (rat IgG2a kappa, eBioscience, #17-

4321-81), CD45 (EF450, eBioscience, #48-0451-82), F4/80 (APC, eBioscience, #17-4801-82), CD11b (R-PE, Tonbo Bioscience, #50-0112-U100). Dot plots were generated using the FlowJo Software.

3.3.6 RNAscope in situ hybridization

RNAscope® 2.0 HD Brown Chromogenic Reagent Kit was used for *RNA in situ* hybridization assay according to the manufacturer's instructions (Advanced Cell Diagnostics, Hayward, CA)[187]. Briefly, suprarenal abdominal aortas of BAF60A$^{f/f}$ and BAF60A^{SMKO} mice infused with AngII for 28 days in the AngII-induced AAA model were fixed in freshly prepared 4% paraformaldehyde for 24h at 4°C before freezing the tissue in optimal cutting temperature (OCT) embedding media (Fisher Healthcare, #23-730-571). Tissue blocks were cut into 8μm sections with a Leica cryostat. Air-dried slides were incubated for 30 min at 60°C and postfixed in 4% paraformaldehyde for 15min at 4°C before use. After dehydration, tissues were treated with a peroxidase blocker, target retrieval solution, and protease plus reagent. Probes targeting mouse Ctss (ACD #579891) and DapB (ACD #310043) for negative control were hybridized for 2h at 40°C, followed by 6 signal amplification steps. DAB was used to detect RNA signals and the tissue was then counterstained with hematoxylin following the manufacturer's protocol. Images were collected with an Olympus IX73 microscope.

3.3.7 Isolation of mouse aortic smooth muscle cells

Mouse aortic smooth muscle cells (MASMCs) were isolated from 8 weeks old male BAF60a$^{f/f}$ and BAF60a^{SMKO} mice as previously described[188]. Briefly, aortas were harvested, followed by the removal of perivascular adipose tissue and digested in 1 mg/mL collagenase type II (Worthington Biochemical Corporation, #LS004174) in Hank's balanced salt solution (HBSS)

(Invitrogen, #14170-112) at 37°C for 10-15 minutes. The adventitial layer of the vessel was removed under a dissecting microscope after the first digestion, and the intimal surface of the aorta was gently rubbed to denude the endothelium. The remaining aortic tissues were then moved to the second enzymatic solution of HBSS containing 1 mg/mL collagenase type II and 0.5 mg/mL elastase (Sigma-Aldrich, #E-0258) and incubated at 37°C for 1 hour. After digestion, smooth muscle cells were dissociated, washed, and cultured in DMEM/F12 supplemented with 20% FBS and 1% penicillin/streptomycin solution (Gibco, #15140122). MASMCs from $BAF60A^{f/f}$ and $BAF60A^{SMKO}$ mice were infected with 10 multiplicity of infection (MOI) of adenovirus expressing GFP (Ad-CMV-GFP) or Cre recombinase (Ad-CMV-iCre, Vector Biolabs, #1045N) for 48 hours before used for experiments. MASMCs were used in passage 5 for co-Immunoprecipitation and passages 6-7 for ChIP assay.

3.3.8 siRNA-mediated BAF60a knockdown

Human aortic smooth muscle cells (HASMCs) were transfected with 30 nM siBAF60a (ThermoFisher Scientific, # s13151) or non-targeting siRNA (Silencer™ Select Negative Control No. 1 siRNA, ThermoFisher Scientific, #4390843) using Lipofectamine RNAiMAX Reagent (Invitrogen, # 13778150) following the manufacturer's instructions.

3.3.9 Adenovirus-mediated BAF60a overexpression

Adenovirus encoding human BAF60a (AdBAF60a)[189] and GFP (AdGFP) was used in the gain of function experiments in this study by infecting HASMCs with 20 multiplicity of infection (MOI) for 48 hours.

3.3.10 Protein extraction and western blotting

Cell extracts were prepared in RIPA lysis buffer and supplemented with Complete™ EDTA-free protease inhibitor cocktail (Roche, #11836170001, Penzberg, Germany) and PhosSTOP™ phosphatase inhibitor (Roche, #4906845001). Human and mouse tissues were homogenized in T-PER™ tissue protein extraction reagent (ThermoFisher Scientific, #78510). Tissue or cells were lysed at 4°C for 30min and centrifuged at 15,000 rpm for 15 minutes to remove insoluble debris. Nuclear and cytoplasmic proteins were extracted using NE-PER™ Nuclear and Cytoplasmic Extraction Reagents (ThermoFisher Scientific, #78835) following the manufacturer's protocol. Protein extracts were resolved in SDS-PAGE gels and transferred to nitrocellulose membranes (Bio-Rad, #1620115, Hercules, CA). Membranes were incubated with primary antibody at 4°C overnight after blocking with 5% non-fat milk for 1 hour at room temperature in TBST. After washing 3 times with TBST, membranes were incubated with IRDye secondary antibody at 0.2 µg/ml (LI-COR Bioscience, Lincoln, NE) at room temperature for 1h. Blots were washed with TBST three times, scanned using the Odyssey CLx Imaging System (LI-COR Bioscience), and quantified with the LI-COR Image Studio Software.

3.3.11 mRNA isolation and qPCR analysis

Total RNA from mouse or human tissues was extracted using TRIzol Reagent (Invitrogen, #15596018) and purified using RNeasy Mini Kit (QIAGEN, #74106, Hilden, Germany). Total RNA from HASMCs was isolated with the RNeasy Mini Kit (QIAGEN, #74106). SuperScript™ III First-Strand Synthesis System (Invitrogen, #18080051) and random primers were used to reverse transcribe RNA into cDNA. Gene expression was quantified in triplicates by quantitative real-time PCR (qPCR) using IQ SYBR Green Supermix (Bio-Rad, #1708882). qPCR primer sequences are listed in Supplemental Table V.

3.3.12 RNA-sequencing

Total RNA was extracted from HASMCs transfected with siControl or siBAF60A for 72h (n=4 for each group) or HASMCs infected with AdGFP or AdSMACRD1for 48h (n=3 for each group), followed by treatment with RNase-free DNase I (QIAGEN, #79254) according to the manufacturer's instructions. RNA library preparation and sequencing were performed by the DNA sequencing core of the University of Michigan. Briefly, RNA quality was assessed with the BioAnalyzer (Agilent) before sequencing. Then, the RNA library was prepared with TruSeq RNA Library Prep Kit v2 (Illumina, San Diego, CA) and 50bp non-stranded single-end sequencing was performed on a HiSeq 4000 platform (Illumina). A total of 350 million reads were generated, with an average of 43 million reads for each sample.

RNAseq read mapping was performed as described previously[190]. Briefly, FastQC (Babraham Bioinformatics) was used for quality control of the sequencing reads from each sample, and one sample in the siBAF60a group was excluded from the subsequent analysis due to the low quality of library preparation. Gene expression quantification was performed using Salmon v 0.14.0[191], with human cDNA sequences of GRCh38 (Ensembl database) as reference. Finally, the differential expression analysis was performed with the DeSeq2 package in R[192].

Gene Set Enrichment Analysis (GSEA)[193] was performed to interpret gene expression profiles of siControl/siBAF60a or AdGFP/AdBAF60a treated HASMCs. In addition, genes were mapped to the HALLMARK gene set in the Molecular Signatures Database (MSigDB) for pathway analysis.

3.3.13 Chromatin immunoprecipitation (ChIP) assay

The chromatin immunoprecipitation (ChIP) experiment followed the instructions in the SimpleChIP Enzymatic Chromatin IP Kit (Magnetic Beads, CST, #9003S). In a nutshell, HASMCs that were 70% confluent were transfected with 30 nM of siRNA targeting BAF60A or a control sequence using Lipofectamine RNAiMAX reagent. The transfected cells were then grown for 72 hours. A ChIP test was performed on MASMCs that had been grown after being removed from the aortas of $BAF60A^{f/f}$ and $BAF60A^{SMKO}$ mice. In order to facilitate the formation of crosslinks between the histones and transcription factors and the DNA, the cells were treated at room temperature for ten minutes with 1% newly produced paraformaldehyde. Before being exposed to 1% paraformaldehyde at room temperature for 10 minutes, cells were given a 45-minute treatment at room temperature with 2mM disuccinimidyl glutarate for BRG1 crosslinking. After that, the crosslinking reaction was stopped by adding 0.1% glycine and letting it sit at room temperature for five minutes. The nuclei were first subjected to micrococcal nuclease digestion at 37 degrees Celsius for twenty minutes, and then they were sonicated using a Branson Sonifier SLPe for twenty seconds at amplification levels of thirty percent three times.

Chromatin was immunoprecipitated at 4°C overnight with rotation using antibodies against BRG1 (Abcam, ab110641, 1:50 dilution), p65 (CST, #8242, 1:100 dilution), or normal rabbit IgG (CST, #2729). After adding ChIP grade Protein G magnetic beads, the IP samples were rotated for two hours at four degrees Celsius. After washing the beads three times with rinse buffer, once with high-salt wash buffer, and once with LiCl buffer, the DNA could be eluted. The DNA was amplified by real-time PCR after being subjected to a reaction with Proteinase K at a temperature of 65 degrees Celsius for two hours.

3.3.14 Chromatin immunoprecipitation followed by sequencing (ChIP-seq)

Using antibodies against BRG1 (Abcam, ab110641, 1:50 dilution), H3K9Ac (CST, #9649, 1:100 dilution), and H3K27Ac (CST, #8173, 1:100 dilution), samples containing 30 ng of DNA were immunoprecipitated, and their respective inputs were sent to the DNA sequencing core at the University of Michigan for quality control, library preparation, and sequencing. The DNA library was created by utilizing the New England Biolabs NEBNext® UltraTM II FS DNA Library Prep Kit for Illumina (located in Ipswich, Massachusetts), and it was sequenced on an Illumina Novaseq S1 flowcell using 100 bp pair-end reads. On average, the number of reads produced for each sample was forty million. Using bowtie2 version 2.3.5 with the default parameters, the ChIP-seq reads were aligned to the human genome (NCBI GRCh19). The MACS2[198] program was used to call the peaks, and the readings from the input served as a control using the following parameters: -f BAMPE -g hs -B —SPMR -q 0.05. Samples normalization was performed to account for the sequencing depth. Integrative Genomics Viewer was used to visualize the peaks (IGV) [194].

3.3.15 Co-immunoprecipitation

HASMCs transfected with siControl or siBAF60a for 72 hours or MASMC isolated from aortas of BAF60A$^{f/f}$ and BAF60A^{SMKO} mice were lysed with Pierce@ IP Lysis Buffer (ThermoScientific, #87788). The cell lysate was sonicated for three periods of 5 seconds each using a Branson Sonifier SLPe at 35% amplitude and centrifuged at 4°C at 15,000 rpm for 10 min. The cell lysate was pre-cleaned with Protein A Magnetic Beads (CST, # 73778) at room temperature for 20 min before incubating with primary antibody against p300 (CST, #54062) or normal rabbit IgG (CST, #2729) at 4°C overnight with rotation. The immunocomplexes were then precipitated with Protein A Magnetic Beads and eluted for Western blot analysis.

3.3.16 Immunofluorescence staining of cultured cells

Cells were cultured in Falcon™ Chambered Cell Culture Slides (Fisher, #08774208) before fixation in 4% paraformaldehyde in PBS at 4°C for 10 min. Following a three-time washing with PBS, the slides were incubated at room temperature for one hour in a blocking solution consisting of 5% normal donkey serum and 0.3% Triton X-100 in PBS. After that, the cells were stained with primary antibodies directed against p65 (CST, #8242, diluted at 1:100) in a dilution buffer consisting of 5% normal donkey serum and 0.1% Triton X-100 in PBS for an overnight period at 4 degrees Celsius, which was then followed by an incubation with an Alexa Fluor conjugated secondary antibody (Jackson ImmunoResearch Laboratories). The slides were mounted using ProLongTM Gold Antifade Mountant with DAPI (Invitrogen, #P36935) and imaged with an Olympus IX73 microscope,

3.3.17 ELISA

HASMCs were transfected with 30nM siRNA to knock down SMACRD1 or negative control siRNA for 48h before changing the medium to fresh OptiMEM (Gibco, # 31985070) with or without 20 ng/ml TNFα for other 24h. In addition, the cell culture supernatant was collected to quantify MCP-1 (R&D, #DCP00) and Cathepsin S (Abcam, #ab155427) by ELISA following the manufacturer's instructions.

3.3.18 Macrophage migration assay

Human aortic smooth muscle cells were transfected with 30 nM siRNA targeting BAF60a (siBAF60a) or negative control (siControl) for 48 hours, or infected with 20MOI AdBAF60A or AdGFP for 48 hours before changing to fresh medium (Opti-MEM, Gibco #31985-070) with or without TNFα (20ng/ml). The medium was changed to fresh OptiMEM 4

hours later and incubated for another 20 hours. The conditioned medium was collected and added to the lower chambers of a Corning Costar Transwell (6.5mm diameter, 8.0μm pore size, Sigma-Aldrich #CLS3464) plate while 2×10^5 RAW 264.7 cells starved in OptiMEM overnight were seeded in the upper chambers of the transwells. After six hours, the cells on the top part of the transwell insert were removed by gently scraping them with a cotton swab. The membranes were then fixed in methanol for ten minutes before being stained with 0.1% crystal violet (Sigma-Aldrich, #C0775) for 15 minutes at room temperature. This process was repeated three times. The microscope captured images of four random fields for each transwell. Then, the ImageJ imaging program was used to count the number of migrated cells.

3.3.19 Statistical analyses

Statistical evaluations were carried out either using the GraphPad Prism 8.0 program (available from GraphPad Software in San Diego, California) or the R programming language (for RNA-seq and ChIP-seq). Data are presented as mean ± standard error of the mean (SEM). If the data were normally distributed and had comparable variances, the parametric Student's t-test was used to compare the difference between the two groups. For comparisons among three or more groups, either a one-way ANOVA followed by Tukey's post hoc analysis or a two-way ANOVA followed by Holm-Sidak post hoc analysis was performed. In addition, the Mann-Whitney test (a nonparametric analysis), Chi-squared analysis (a distribution analysis), and the Mantel-Cox test (a survival percentage analysis) were used to analyze the differences between the two groups when the data did not pass the normality test. The results were deemed statistically significant if they had a p-value of less than 0.05. At least three separate experiments were performed for each result.

3.4 Results

3.4.1 BAF60a is highly expressed in human and murine AAA

We first compared the expression of BAF60a in human AAA samples and normal aortic tissues by quantitative real-time PCR (qPCR) and Western blot, and the results showed significantly increased BAF60a mRNA and protein levels in aneurysmal aortic tissues (Fig. 3.1 A-B). In addition, immunofluorescence staining confirmed upregulated BAF60a in the human abdominal aorta (Fig. 3.1 C). We also monitored the BAF60a expression levels in the murine experimental AAA models. In the AngII model[181], using adeno-associated virus (AAV) carrying a gain-of-function mutation of the mouse proprotein convertase subtilisin/kexin type 9 (AAV-Pcsk9.D377Y, hereafter AAV-Pcsk9) (Fig. 3.1 D), both the mRNA and the protein levels of BAF60a exhibit a significant increase in mouse AAA (Fig. 3.1 E-F). We then assessed BAF60a abundance during the pathogenic process of elastase-induced AAA by immunofluorescence staining (Fig 3.1 G). Similarly, increased expression of BAF60a was identified at 7 and 14 days after elastase exposure (Fig. 3.1 H). Altogether, these data indicate a potential pathogenic role of BAF60a in AAA development.

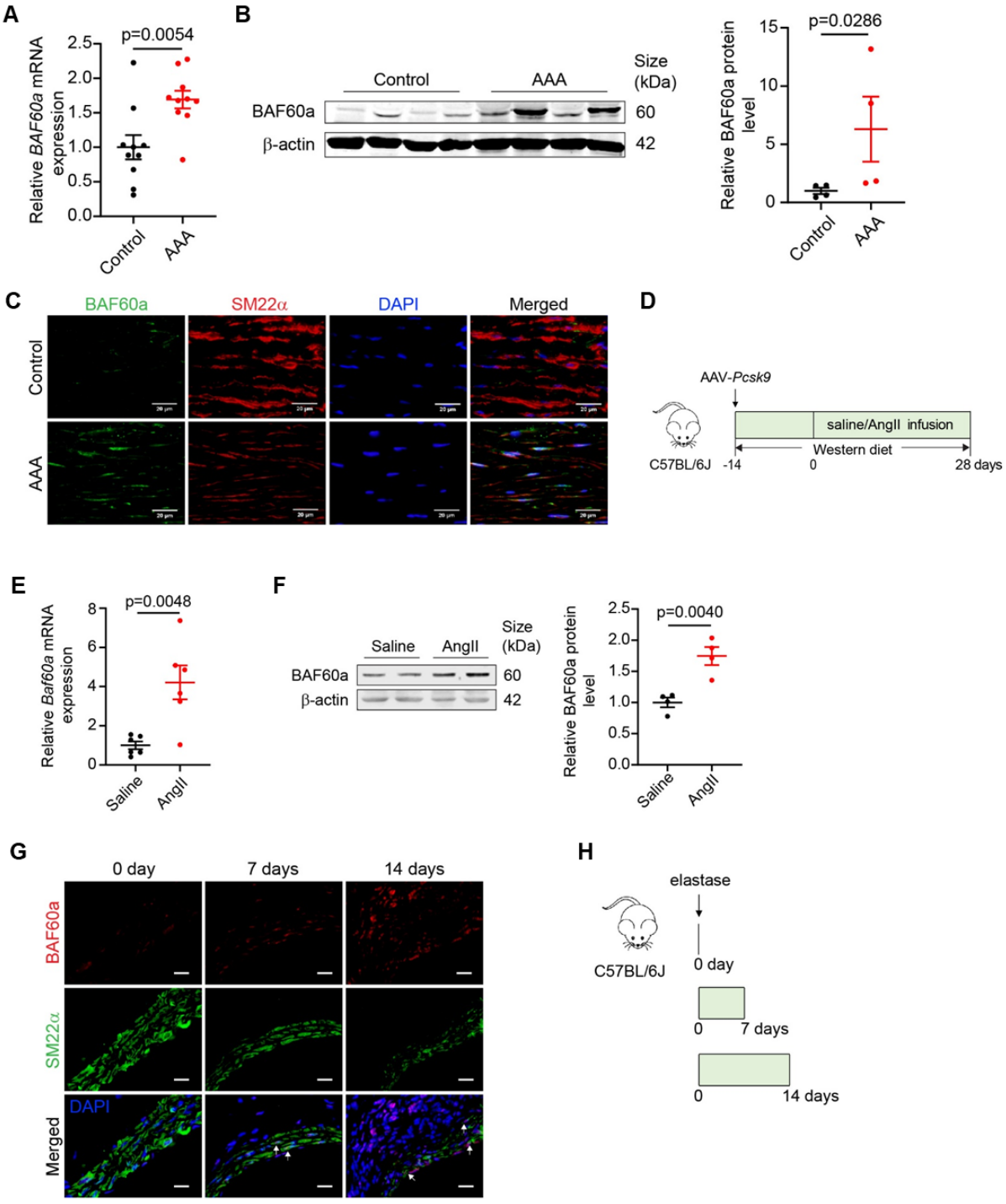

A
p=0.0054
Relative BAF60a mRNA expression
2.5
2.0
1.5
1.0
0.5
0.0
Control
AAA
B
Control
AAA
Size (kDa)
BAF60a
60
β-actin
42
p=0.0286
Relative BAF60a protein level
15
10
5
0
Control
AAA
C
BAF60a
SM22α
DAPI
Merged
Control
AAA
D
AAV-Pcsk9
C57BL/6J
saline/AngII infusion
Western diet
-14
0
28 days
E
p=0.0048
Relative Baf60a mRNA expression
8
6
4
2
0
Saline
AngII
F
Saline
AngII
Size (kDa)
BAF60a
60
β-actin
42
p=0.0040
Relative BAF60a protein level
2.5
2.0
1.5
1.0
0.5
0.0
Saline
AngII
G
0 day
7 days
14 days
BAF60a
SM22α
DAPI
Merged
H
elastase
C57BL/6J
0 day
0
7 days
0
14 days

Figure 3.1 BAF60a is upregulated in human and murine AAA.

A, BAF60a mRNA expression was determined by qPCR in human AAA lesions (n=10) and control abdominal aortas (n=10). B, BAF60a protein abundance was determined by Western blotting in human AAA lesion (n=4) and control abdominal aortic areas (n=4). C, Representative immunofluorescence staining of BAF60a (green) in human AAA samples (n=3) and control abdominal aortas (n=3). SM22α, red; DAPI blue. Scale bar=20 μm. D, Schematic saline and AngII infusion diagram in the AngII-induced AAA model in C57BL/6J mice. E-F, Relative BAF60a mRNA and protein levels were determined by qPCR (E, n=6 for each group) and Western blotting (F, n=4 for each group) in abdominal aortas of C57BL/6J mice infused with saline or AngII for 28 days. G, Representative immunofluorescence staining of BAF60a (red) in the infrarenal abdominal aortas of C57BL/6J mice at 0, 7, or 14 days after elastase exposure (n=3 for each group). SM22α, green; DAPI, blue. Scale bar=10 μm. H, Schematic diagram of elastase treatment for 0, 7, or 14 days in C57BL/6J mice. Data are presented as mean±SEM. Student's t-tests for A, E, and F. Data are presented as mean±SEM. Nonparametric Mann-Whitney test for B.

3.4.2 BAF60a deficiency in VSMCs attenuates AngII-induced murine AAA formation

VSMCs play a crucial role in maintaining vascular homeostasis, and their dysfunction is a hallmark of AAA[195]. To determine the function of BAF60a in the pathogenesis of AAA, we used 8 to 10 weeks old male BAF60a$^{f/f}$ and BAF60a^{SMKO} mice and subjected them to AngII-induced AAA formation or sham operation. In the presence of AngII, a 57.14% AAA incidence was observed in BAF60a$^{f/f}$ mice, while only 8.33% of BAF60a^{SMKO} mice developed aneurysms in their suprarenal aortas (Fig. 3.2 A-B). Furthermore, AngII infused BAF60a^{SMKO} mice showed a significant decrease in maximal outer diameters compared with BAF60a$^{f/f}$ mice (BAF60a$^{f/f}$ 1.41 ± 0.09mm vs. BAF60a^{SMKO} 1.05 ± 0.05mm, p=0.0001, Fig. 3.2 C). No significant differences were found in survival rate, systolic blood pressure, body weight, total serum cholesterol and triglyceride levels between AngII-infused BAF60a$^{f/f}$ and BAF60a^{SMKO} mice (Fig. 3.2 D-H). In sham-operated groups, no mice developed AAA (Fig. 3.2 I-K).

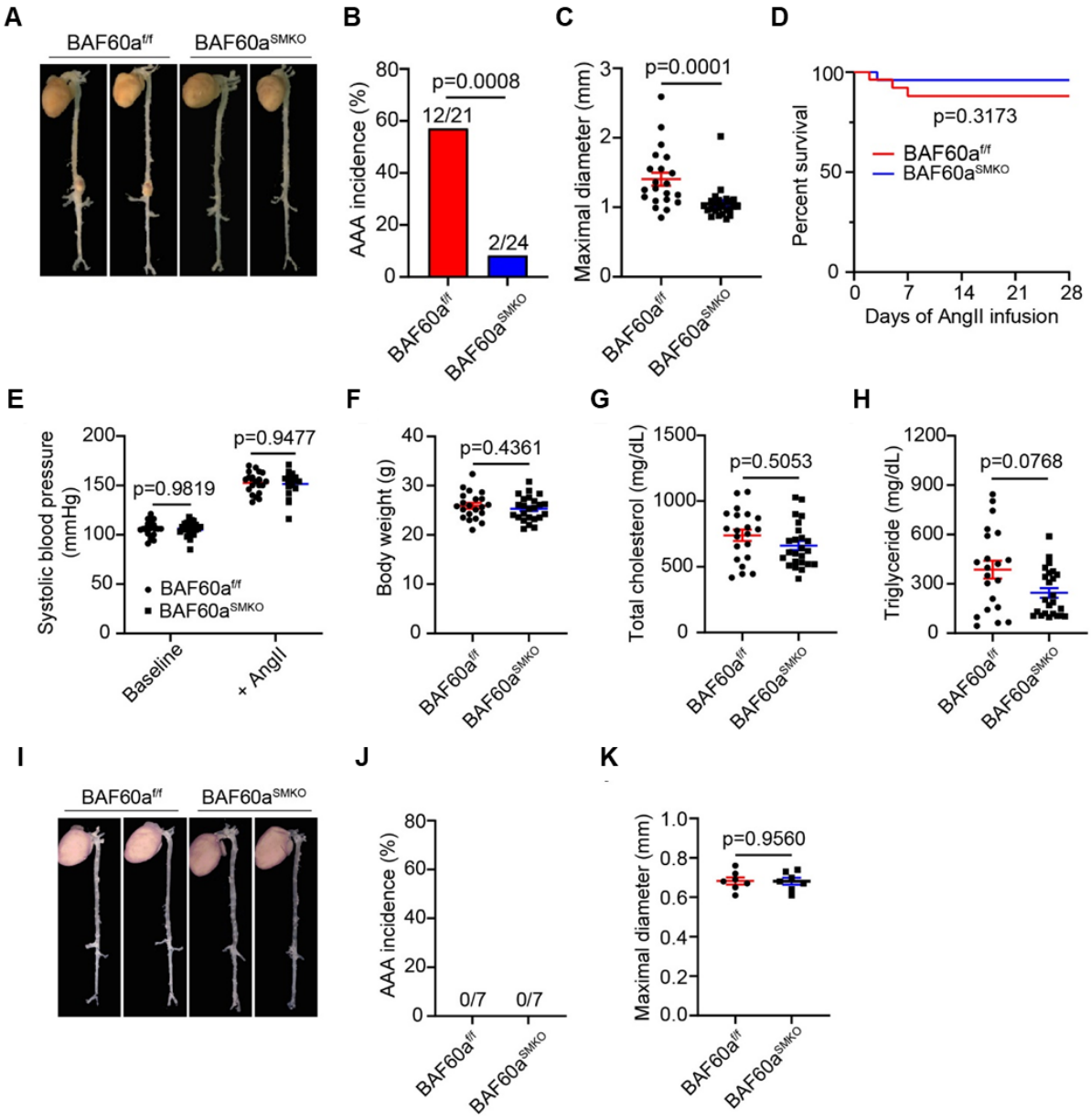

A
BAF60a^f/f
BAF60a^SMKO
B
AAA incidence (%)
p=0.0008
12/21
2/24
BAF60a^f/f
BAF60a^SMKO
C
Maximal diameter (mm)
p=0.0001
BAF60a^f/f
BAF60a^SMKO
D
Percent survival
p=0.3173
BAF60a^f/f
BAF60a^SMKO
Days of AngII infusion
E
Systolic blood pressure (mmHg)
p=0.9819
p=0.9477
BAF60a^f/f
BAF60a^SMKO
Baseline
+ AngII
F
Body weight (g)
p=0.4361
BAF60a^f/f
BAF60a^SMKO
G
Total cholesterol (mg/dL)
p=0.5053
BAF60a^f/f
BAF60a^SMKO
H
Triglyceride (mg/dL)
p=0.0768
BAF60a^f/f
BAF60a^SMKO
I
BAF60a^f/f
BAF60a^SMKO
J
AAA incidence (%)
0/7
0/7
BAF60a^f/f
BAF60a^SMKO
K
Maximal diameter (mm)
p=0.9560
BAF60a^f/f
BAF60a^SMKO

Figure 3.2 BAF60a deficiency in VSMCs attenuates AngII-induced murine AAA formation

In the AngII-induced AAA model, 8 to 10 weeks old male BAF60a$^{f/f}$ (n=24) and BAF60a^{SMKO} (n=25) mice were given AAV-Pcsk9 (i.p.) and a Western diet to generate hypercholesterolemia followed by AngII (1,500 ng/kg/min) infusion for 28 days. A, Representative morphology of aortas. B, Incidence of AAA, rupture events in the thoracic aorta were excluded from AAA incidence. C, Quantification of maximal external diameters of suprarenal aortas. D, Survival rates indicated by Kaplan-Meier curves. E, Systolic blood pressure before and 28 days after AngII minipump implantation. F-H, Body weight (F), total serum cholesterol (G), and triglyceride levels (H) of BAF60a$^{f/f}$ and BAF60a^{SMKO} mice infused with AngII for 28 days. I-K, Eight to 10 weeks old male BAF60a$^{f/f}$ (n=7) and BAF60a^{SMKO} mice (n=7) were subjected to sham operation and euthanized 28 days after surgery. I, Representative morphology of aortas. G, Incidence of AAA. K, Quantification of maximal external diameters of suprarenal aortas. Data are presented as mean ± SEM. Chi-squared test for B, J, Mann-Whitney test for C, K, Mantel-Cox test for D, two-way ANOVA followed by Holm-Sidak analysis for E, and Student's t-test for F-H.

3.4.3 BAF60a deficiency in VSMCs attenuates elastase-induced murine AAA formation

To further verify the role of VSMC-specific BAF60a deletion in attenuating AAA formation, the elastase-induced aneurysm model was performed on 10 to 12 weeks old male BAF60a$^{f/f}$ and BAF60a^{SMKO} mice. Fourteen days after elastase exposure, systolic blood pressure, body weight, total serum cholesterol, and serum triglyceride levels were comparable between the two groups (Fig. 3.3 A-D). No mice developed AAA with heat-inactivated elastase exposure (Fig. 3.3 E-G). However, and consistent with the AngII model, BAF60a depletion in VSMCs significantly reduced elastase-induced AAA incidence (BAF60a$^{f/f}$ 72.22% vs. BAF60a^{SMKO} 6.67%, p=0.0002, Fig. 3.3 H-I) and maximal infrarenal aortic diameter (BAF60a$^{f/f}$ 0.83 ± 0.04mm vs. BAF60a^{SMKO} 0.58 ± 0.02mm, p<0.0001, Fig. 3.3 J).

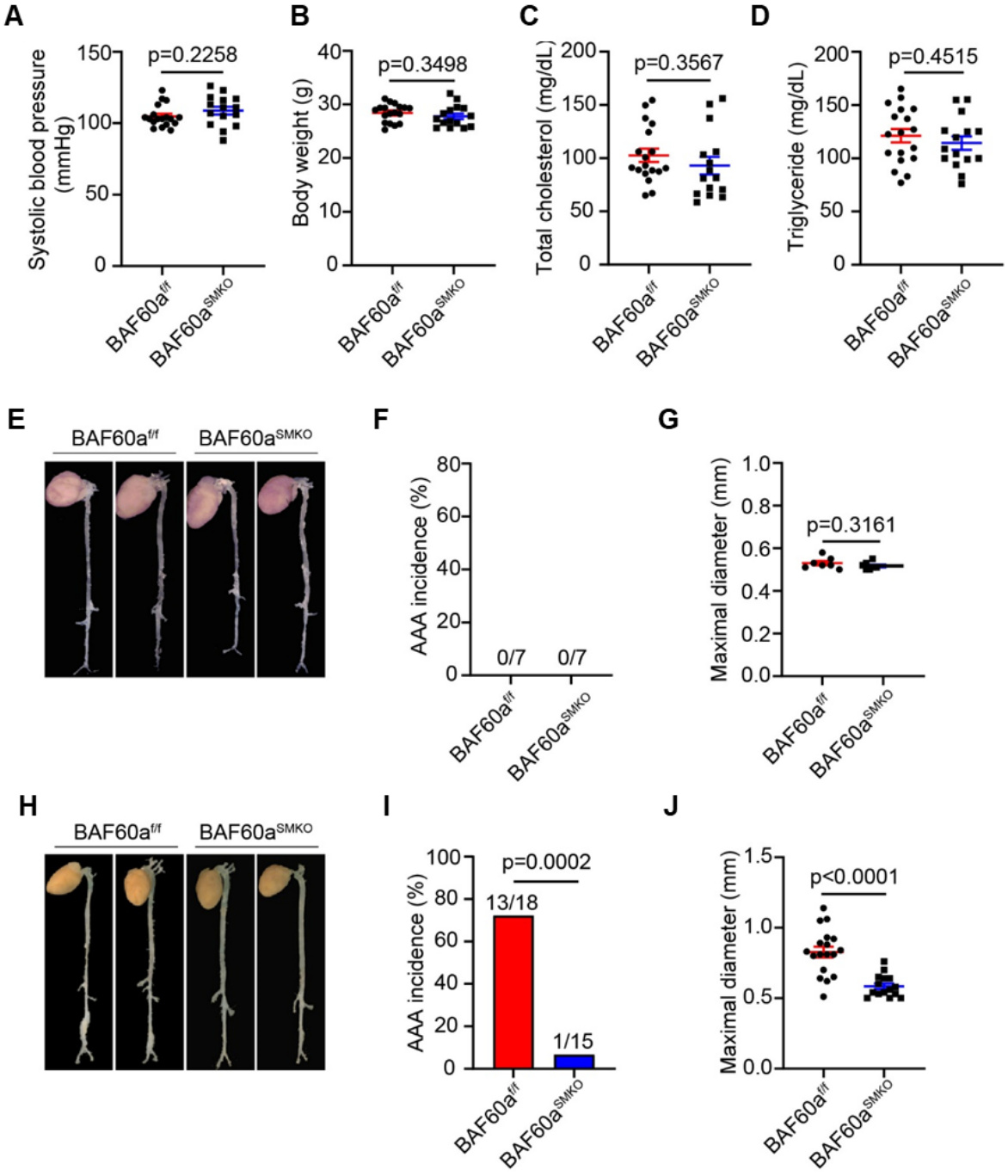

A
Systolic blood pressure (mmHg)
150
100
50
0
p=0.2258
BAF60a^f/f
BAF60a^SMKO
B
Body weight (g)
40
30
20
10
0
p=0.3498
BAF60a^f/f
BAF60a^SMKO
C
Total cholesterol (mg/dL)
200
150
100
50
0
p=0.3567
BAF60a^f/f
BAF60a^SMKO
D
Triglyceride (mg/dL)
200
150
100
50
0
p=0.4515
BAF60a^f/f
BAF60a^SMKO
E
BAF60a^f/f
BAF60a^SMKO
F
AAA incidence (%)
80
60
40
20
0
0/7
0/7
BAF60a^f/f
BAF60a^SMKO
G
Maximal diameter (mm)
1.0
0.8
0.6
0.4
0.2
0.0
p=0.3161
BAF60a^f/f
BAF60a^SMKO
H
BAF60a^f/f
BAF60a^SMKO
I
AAA incidence (%)
100
80
60
40
20
0
p=0.0002
13/18
1/15
BAF60a^f/f
BAF60a^SMKO
J
Maximal diameter (mm)
1.5
1.0
0.5
0.0
p<0.0001
BAF60a^f/f
BAF60a^SMKO

Figure 3.3 BAF60a deficiency in VSMCs attenuates elastase-induced murine AAA formation

Ten to 12 weeks old male BAF60a$^{f/f}$ and BAF60a^{SMKO} mice were subjected to elastase-induced AAA by the treatment of the infrarenal aortas with 30 μL elastase for 30 min as described in the Supplemental Methods and euthanized 14 days after elastase exposure. A-D, Systolic blood pressure (A), body weight (B), total serum cholesterol (C) and triglyceride levels (D) in BAF60a$^{f/f}$ and BAF60a^{SMKO} mice. E-G, Ten to 12 weeks old male BAF60a$^{f/f}$ (n=7) and BAF60a^{SMKO} (n=7) mice were treated with the sham operation and euthanized 14 days after surgery. E, Representative morphology of aortas. F, Incidence of AAA. G, Quantification of maximal external diameters of suprarenal aortas. H-J, In the elastase-induced AAA model, 10 to 12 weeks old male BAF60a$^{f/f}$ (n=18) and BAF60a^{SMKO} (n=15) mice were treated with elastase and euthanized 14 days after elastase exposure. H, Representative morphology of aortas. I, Incidence of AAA. J, Quantification of the maximal external diameter of infrarenal aortas. Data are presented as mean±SEM. Student's t-test for A-D, G, J. Chi-squared test for F, I.

3.4.4 BAF60a deficiency in VSMCs reduces ECM degradation in AAA lesions

Elastin fragmentation is well recognized to play a pivotal role in aortic wall dilation and can be detected through Verhoff Van Gieson staining[185]. Sham-operated mice identified no elastin breakage in either suprarenal or infrarenal aortic sections (Fig. 3.4 A-B). Notably, BAF60a^{SMKO} mice were protected from severe ECM degradation induced by AngII infusion (Fig. 3.4 C) or elastase exposure (Fig. 3.4 D), indicating a reduced level of protease production or activity.

We then checked the expression of several proteolytic cysteine cathepsins reported to contribute to the pathogenesis of AAA[196] in the medial layer of aortas harvested from the AngII-induced AAA model. Notably, the mRNA level of cathepsin S, encoded by the CTSS gene, was significantly downregulated in the aortas of BAF60a^{SMKO} mice compared with BAF60a$^{f/f}$ mice (Fig. 3.4 E). This finding was confirmed by RNAscope assay, a novel RNA in situ hybridization technology using specific probes to measure gene expression within tissues[197]. In addition, abundant brown staining representing Ctss RNA was detected in the aortic sections of BAF60a$^{f/f}$ mice, mainly located in the media and adventitia. In contrast, the equivalent aortic area from BAF60a^{SMKO} mice demonstrated faint staining with a reduction in both the amount and density of the punctate signals (Fig. 3.4 F). Furthermore, deletion of BAF60a in VSMCs largely inhibited the aneurysm-associated increase[196] in cathepsin S protein expression as indicated by Western blot (Fig. 3.4 G).

Next, we investigated the effect of BAF60a depletion in VSMCs on matrix metalloproteinases (MMPs) expression, especially MMP2 and MMP9, two well-recognized family members reported contributing to ECM degradation during AAA formation[198, 199]. qPCR showed that the mRNA level of MMP9, not MMP2, was significantly decreased in the

aortic media following BAF60a deficiency in the AngII-induced AAA model (Fig. 3.4 H). Immunofluorescence staining further confirmed the reduction of MMP9 in the tunica media of the abdominal aortas of AngII and elastase (Fig. 3.4 I-J) treated BAF60a^{SMKO} mice. Interestingly, reduced signals of both MMP9 and MMP2 were noted in the adventitia of the abdominal aortic wall of BAF60a^{SMKO} mice. Since macrophages are a significant source of MMPs, the discrepancy in MMP2 qPCR and immunofluorescence staining may be due to suppressed recruitment of immune cells into the BAF60a^{SMKO} mouse aorta.

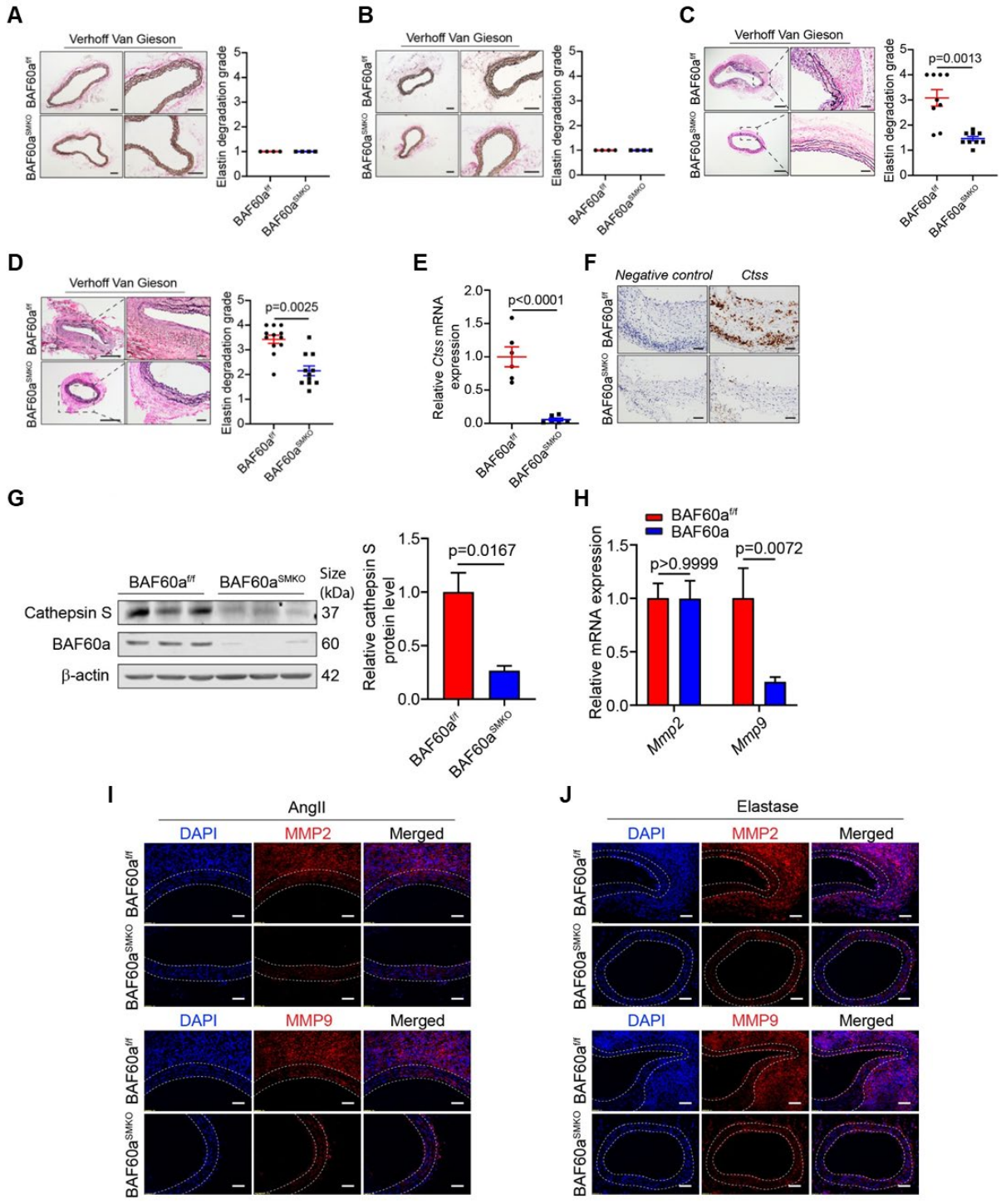

A
Verhoff Van Gieson
BAF60a f/f
BAF60a SMKO
Elastin degradation grade
B
C
p=0.0013
D
p=0.0025
E
Relative Ctss mRNA expression
p<0.0001
F
Negative control
Ctss
G
BAF60a f/f
BAF60a SMKO
Size (kDa)
Cathepsin S
37
BAF60a
60
β-actin
42
Relative cathepsin S protein level
p=0.0167
H
BAF60a f/f
BAF60a
Relative mRNA expression
p>0.9999
p=0.0072
Mmp2
Mmp9
I
AngII
DAPI
MMP2
Merged
MMP9
J
Elastase

Figure 3.4 BAF60a deficiency in VSMCs reduces ECM degradation in AAA lesions

A, Representative images of Verhoff Van Gieson staining and quantification analysis of elastin fragmentation in suprarenal aortic sections from BAF60a$^{f/f}$ (n=4) and BAF60a^{SMKO} (n=4) mice 28 days after sham operation in AngII-induced AAA model. Scale bar=100 μm. B, Representative images of Verhoff Van Gieson staining and quantification analysis of elastin fragmentation in infrarenal aortic sections from BAF60a$^{f/f}$ (n=4) and BAF60a^{SMKO} (n=4) mice 14 days after sham operation in elastase-induced AAA model. Scale bar=100 μm. C, Representative images of Verhoff Van Gieson staining in aortic sections and quantification analysis of elastin fragmentation (n=9 for each group). Scale bar=200 μm for whole aortic sections; scale bar=20 μm for magnified areas on the right. D, Representative images of Verhoff Van Gieson staining and quantification analysis of elastin fragmentation in aortic sections from BAF60a$^{f/f}$ (n=12) and BAF60a^{SMKO} (n=11) mice 14 days after elastase treatment. Scale bar=200 μm for whole aortic sections; scale bar=20 μm for magnified areas on the right. E, Cathepsin S mRNA expression was determined by qPCR in aortic RNA extract (n=6 for each group). F, Representative images of RNAscope in situ hybridization assay detecting Cathepsin S mRNA in aortic sections (n=3 for each group). Scale bar=20 μm. G, The Western blot determined Cathepsin S protein level in abdominal aortic extracts (n=3 for each group). H, Relative MMP2 and MMP9 mRNA and levels were determined by qPCR in the aortic media of BAF60a$^{f/f}$ (n=5) and BAF60a^{SMKO} (n=5) mice 28 days after AngII infusion. I-J, Representative immunofluorescence staining of MMP2 and MMP9 (red) in aortic sections from BAF60a$^{f/f}$ and BAF60a^{SMKO} mice subjected to AngII- (I) or elastase- (J) induced AAA model. Nuclei stained by DAPI were indicated in blue. Dotted lines depict aortic media. Scale bar=20 μm. n=3 for each group. Data are presented as mean±SEM. Student's t-test for C-E, G. One-way ANOVA followed by Tukey's post hoc analysis for H.

3.4.5 BAF60a deficiency in VSMCs suppresses inflammatory response in AAA lesions

To explore whether the protective effect of VSMC-specific BAF60a knockout in AAA development is related to reduced immune cell recruitment, flow cytometry analysis was performed on single cells isolated from abdominal aortas[200]. No significant difference was identified in the proportions of CD45+ leukocytes and CD11b+/F4/80+ macrophages between sham-operated BAF60a$^{f/f}$ and BAF60a^{SMKO} mice. However, in the presence of AngII or elastase, significantly decreased numbers of CD45+ leukocytes and CD11b+/F4/80+ macrophages were noticed in BAF60a^{SMKO} aortas (Fig. 3.5 A-F). Further immunofluorescence staining of Mac2 confirmed the attenuated macrophage accumulation in the aortic wall of BAF60a^{SMKO} mice compared with BAF60a$^{f/f}$ mice (Fig. 3.5 G-H). The systemic inflammatory response was then determined by ELISA measuring the concentration of circulating monocyte chemoattractant protein-1 (MCP-1/CCL2) and interleukin-6 (IL-6), two inflammatory cytokines that were reported as elevated in human AAA disease[173, 201]. In the AngII model, serum MCP-1 concentration in BAF60a^{SMKO} mice was significantly lower than in BAF60a$^{f/f}$ mice (Fig. 3.5 I); serum IL-6 level was also decreased in BAF60a^{SMKO} mice, although without statistical significance due to wide variation (Fig. 3.5 J). However, in the elastase-induced AAA model, circulating MCP-1 and IL-6 concentrations were not significantly changed in the BAF60a^{SMKO} mice (Fig. 3.5 K-L), likely due to the highly localized nature of the stimulus in this model.

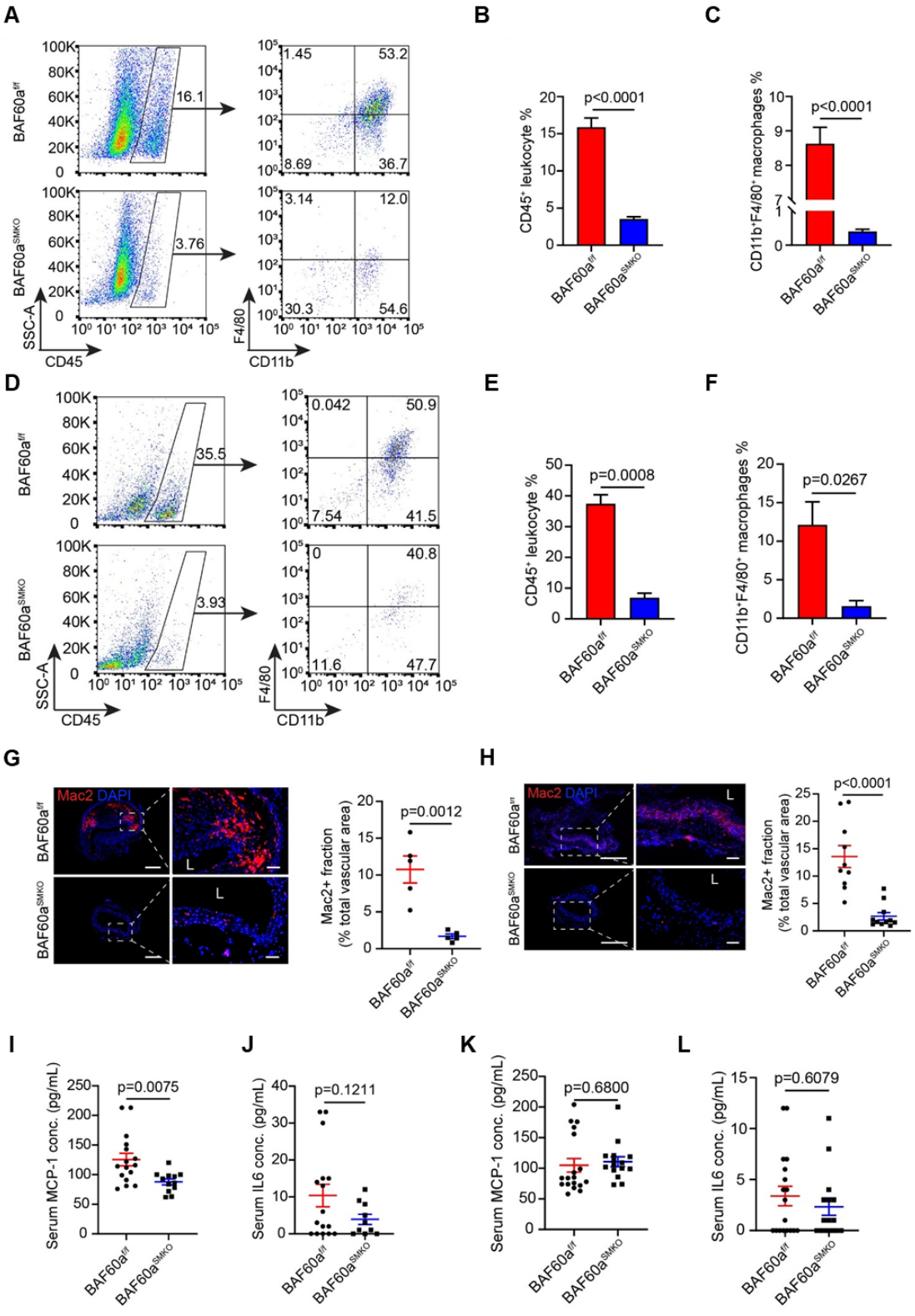

A
BAF60a f/f
BAF60a SMKO
SSC-A
CD45
F4/80
CD11b
16.1
3.76
1.45
53.2
8.69
36.7
3.14
12.0
30.3
54.6
B
CD45+ leukocyte %
p<0.0001
BAF60a f/f
BAF60a SMKO
C
CD11b+F4/80+ macrophages %
p<0.0001
D
35.5
3.93
0.042
50.9
7.54
41.5
0
40.8
11.6
47.7
E
CD45+ leukocyte %
p=0.0008
F
CD11b+F4/80+ macrophages %
p=0.0267
G
Mac2 DAPI
L
Mac2+ fraction (% total vascular area)
p=0.0012
H
p<0.0001
I
Serum MCP-1 conc. (pg/mL)
p=0.0075
J
Serum IL6 conc. (pg/mL)
p=0.1211
K
Serum MCP-1 conc. (pg/mL)
p=0.6800
L
Serum IL6 conc. (pg/mL)
p=0.6079

Figure 3.5 BAF60a deficiency in VSMCs suppresses inflammatory response in AAA lesion

A-C, Single cells were isolated from abdominal aortas of BAF60a$^{f/f}$ (n=3) and BAF60a^{SMKO} (n=3) mice after 28 days of AngII infusion, and flow cytometry analysis was performed. A, D, Representative dot plots showing the gating strategy to obtain the macrophage population (CD11b+F4/80+) from gated CD45+ leukocytes. B, E, Quantitative analysis of the percentage of CD45+ leukocytes. C, F, Quantitative analysis of the CD11b+F4/80+ macrophage percentage. AngII- (A-C) or elastase- (D-F). G-H, Representative images of Mac2 staining (red) and quantification analysis of Mac2+ fraction in abdominal aortas of BAF60a$^{f/f}$ (n=5) and BAF60a^{SMKO} (n=5) mice. AngII- (G) or elastase- (H). Scale bar=200 μm for whole aortic sections; scale bar=20 μm for magnified areas; L, lumen. Data are presented as mean±SEM. Student's t-test for B, C, E, F, I-L.

3.4.6 BAF60a knockdown reduces VSMC inflammation

To further explore the molecular mechanisms underlying the function of BAF60a in AAA development, small interfering RNA (siRNA) was used to knockdown BAF60a (siBAF60a) in cultured human aortic smooth muscle cells (HASMCs) (Fig. 3.6 A), and RNA sequencing was performed to uncover the transcriptomic changes relative to HASMCs transfected with control siRNA (siControl). Gene Set Enrichment Analysis (GSEA)[202] was employed to search for overrepresented pathways across the Molecular Signatures Database (MSigDB) and the top ten up-regulated and down-regulated HALLMARK pathways are listed (Fig. 3.6 B). Notably, inflammatory response and TNFα signaling via NF-κB were highly enriched as the top two down-regulated pathways in HASMCs transfected with siBAF60a, indicating suppressed inflammation upon BAF60a knockdown in VSMCs (Fig. 3.6 C). In addition, decreased expression of several pro-inflammatory cytokines regulated by NF-κB (nuclear factor kappa-light-chain-enhancer of activated B cells) (Fig. 3.6 D) was validated through qPCR (Fig. 3.6 E). Furthermore, silencing of BAF60a in HASMCs decreased TNFα (tumor necrosis factor alpha)-induced MCP-1 secretion to the culture medium, as determined by ELISA (Fig. 3.6 F). Consistently, further macrophage migration assay[185] also indicated a decreased level of cytokine secretion, as demonstrated by significantly reduced recruitment of RAW264.7 cells (a mouse macrophage cell line) towards the conditioned medium of BAF60a-deficient HASMCs (Fig. 3.6 G).

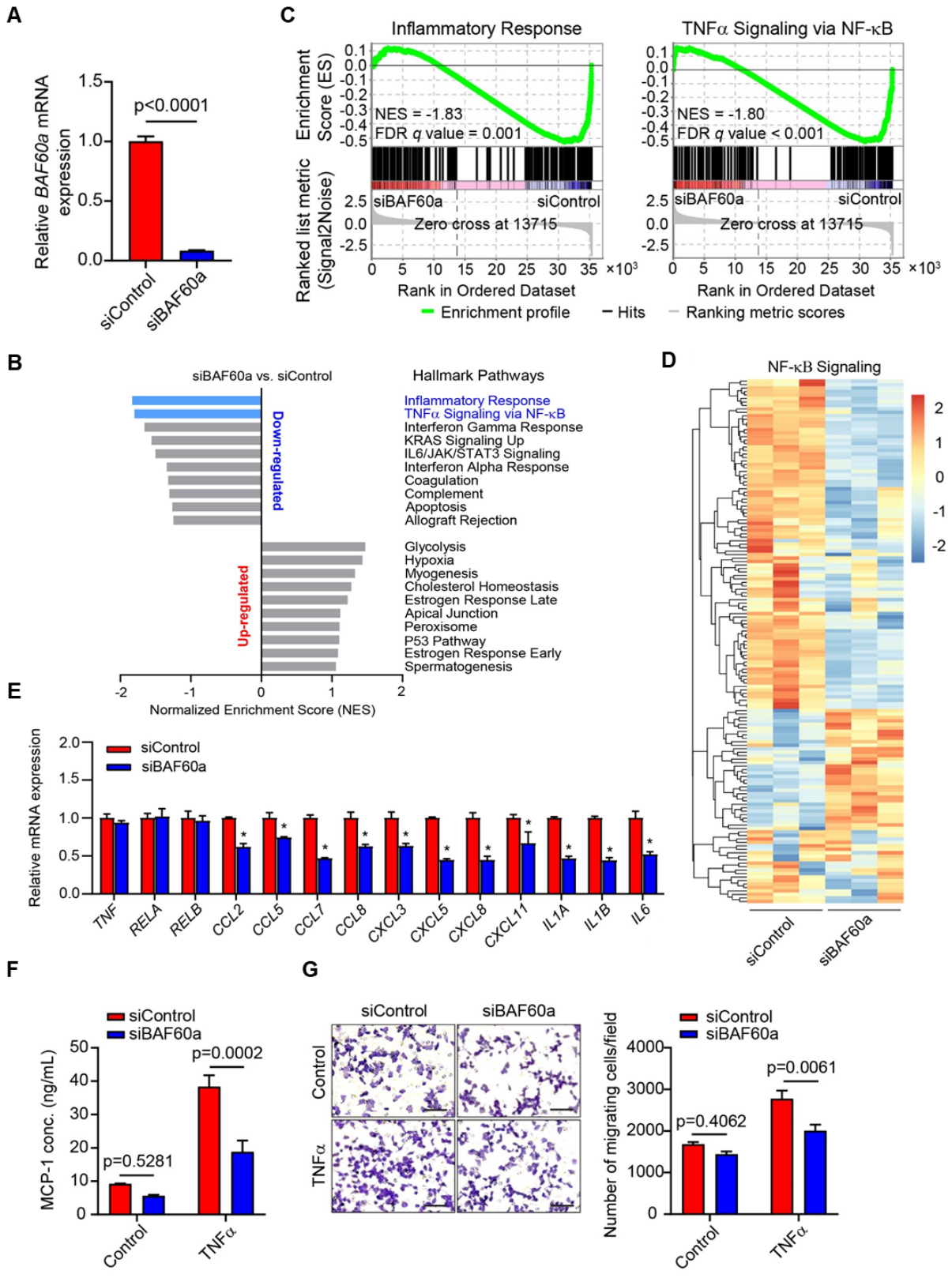

A
Relative BAF60a mRNA expression
p<0.0001
siControl
siBAF60a
C
Inflammatory Response
TNFα Signaling via NF-κB
Enrichment Score (ES)
NES = -1.83
FDR q value = 0.001
NES = -1.80
FDR q value < 0.001
Ranked list metric (Signal2Noise)
siBAF60a
siControl
Zero cross at 13715
Rank in Ordered Dataset
Enrichment profile
Hits
Ranking metric scores
B
siBAF60a vs. siControl
Hallmark Pathways
Down-regulated
Up-regulated
Inflammatory Response
TNFα Signaling via NF-κB
Interferon Gamma Response
KRAS Signaling Up
IL6/JAK/STAT3 Signaling
Interferon Alpha Response
Coagulation
Complement
Apoptosis
Allograft Rejection
Glycolysis
Hypoxia
Myogenesis
Cholesterol Homeostasis
Estrogen Response Late
Apical Junction
Peroxisome
P53 Pathway
Estrogen Response Early
Spermatogenesis
Normalized Enrichment Score (NES)
D
NF-κB Signaling
siControl
siBAF60a
E
Relative mRNA expression
siControl
siBAF60a
TNF
RELA
RELB
CCL2
CCL5
CCL7
CCL8
CXCL3
CXCL5
CXCL8
CXCL11
IL1A
IL1B
IL6
F
MCP-1 conc. (ng/mL)
siControl
siBAF60a
p=0.5281
p=0.0002
Control
TNFα
G
siControl
siBAF60a
Control
TNFα
Number of migrating cells/field
p=0.4062
p=0.0061

Figure 3.6 BAF60a knockdown reduces VSMC inflammation

A-B, HASMCs were transfected with siControl or siBAF60a (30 nM). After 72 hours, total RNA was extracted for RNA-seq (n=3 for each group). A, BAF60a mRNA expression was determined by qPCR. B, Gene set enrichment analysis (GSEA) was performed using transcriptomic data from RNA-seq (siBAF60a vs. siControl). Bars show normalized enrichment scores (NES) of the top ten upregulated and downregulated pathways on the hallmark gene set. C, Negative enrichment in the Inflammatory Response (left) and the TNFα Signaling via NF-κB (right) pathways are shown in GSEA plots (siBAF60a vs. siControl). D, Genes involved in NF-κB signaling are shown by heatmap. The color bar [red to blue (2 to −2) vertical bar] denotes the row-scaled transcripts per million (TPM) value, representing the Z score of gene expression across samples. E, qPCR Validation of representative NF-κB target genes identified by RNA-seq in 3 independent sets of samples treated as in A. n=3 for each group. F, MCP-1 concentration was measured by ELISA in the cell culture medium of HASMCs transfected with siControl or siBAF60a for 48 hours, followed by treatment with or without TNFα (20 ng/ml, 24h). n=3. G, Representative images (magnified field, left) and quantitative analysis (right) of the macrophages migrated through the transwell toward the conditioned media from HASMCs transfected with siControl or siBAF60a, with or without TNFα stimulation (20 ng/ml, 20h). n=3. Scale bar=100 μm. Data are presented as mean ± SEM. *$p < 0.05$. Student's t-test for A, one-way ANOVA followed by Tukey's post hoc analysis for E, and two-way ANOVA followed by Holm-Sidak post hoc analysis for D-G.

3.4.7 BAF60a overexpression aggravates VSMC inflammation

As a complementary approach, BAF60a was overexpressed in HASMCs (Fig. 3.7 A), followed by RNA sequencing. As a result, GSEA uncovered that inflammatory response and TNFα signaling via NF-κB are highly enriched in BAF60a-overexpressing HASMCs (Fig. 3.7 B). Moreover, BAF60a overexpression upregulated the mRNA level of several NF-κB target genes encoding pro-inflammatory cytokines (Fig. 3.7 C) and enhanced macrophage migration (Fig. 3.7 D). Altogether, these data indicate that BAF60a induces VSMC inflammatory response.

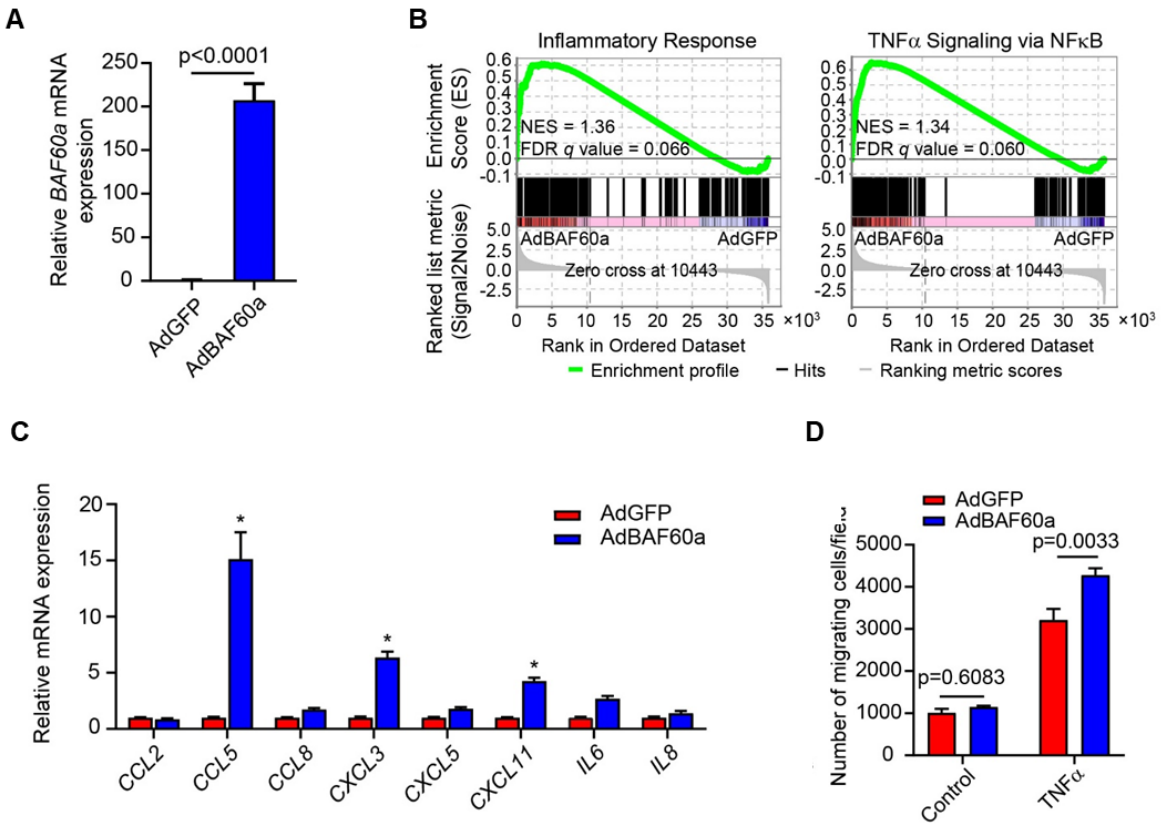


Figure 3.7 BAF60a overexpression aggravates VSMC inflammation

HASMCs were infected with AdGFP or AdBAF60a (20 MOI). Total RNA was extracted after 48 hours for RNA-seq (n=3 for each group). A, BAF60a mRNA expression was determined by qPCR. n=3. B, Positive enrichment in the Inflammatory Response (left) and the TNFα Signaling via NF-κB (right) pathways are shown in GSEA plots (AdBAF60a vs. AdGFP). C, qPCR Validation of representative NF-κB target genes identified by RNA-seq in 3 independent sets of samples. n=3 for each group. D, Quantitative analysis of the migrated macrophages in the transwell migration assay using the conditioned media from HASMCs infected with AdGFP or AdBAF60a, with or without TNFα stimulation (20 ng/ml, 20h). n=3. Data are presented as mean±SEM. Student's t-test for A, one-way ANOVA followed by Tukey's post hoc analysis for C. Two-way ANOVA followed by Holm-Sidak post hoc analysis for D. *$p < 0.05$.

3.4.8 BAF60a regulates Cathepsin S expression in VSMCs

RNA-seq in HASMCs also indicated an alteration in the mRNA levels of various cathepsins upon BAF60a knockdown and overexpression. Notably, cathepsin S expression was significantly down-regulated (log2 fold change = -1.080, adjusted p-value = 2.5E-21) in BAF60a deficient HASMCs and up-regulated in BAF60a-overexpressing HASMCs (log2 fold change = 1.430, adjusted p-value = 5.1E-4), which was later confirmed by qPCR (Fig. 3.8 A-B), respectively. Furthermore, TNFα stimulation upregulated cathepsin S protein levels in cultured HASMCs, while knockdown of BAF60a significantly reduced cathepsin S protein expression (Fig. 3.8 C). Consistently, silencing of BAF60a decreased the concentration of cathepsin S secreted into the HASMCs culture media either in the presence or absence of TNFα, as measured by ELISA (Fig. 3.8 D).

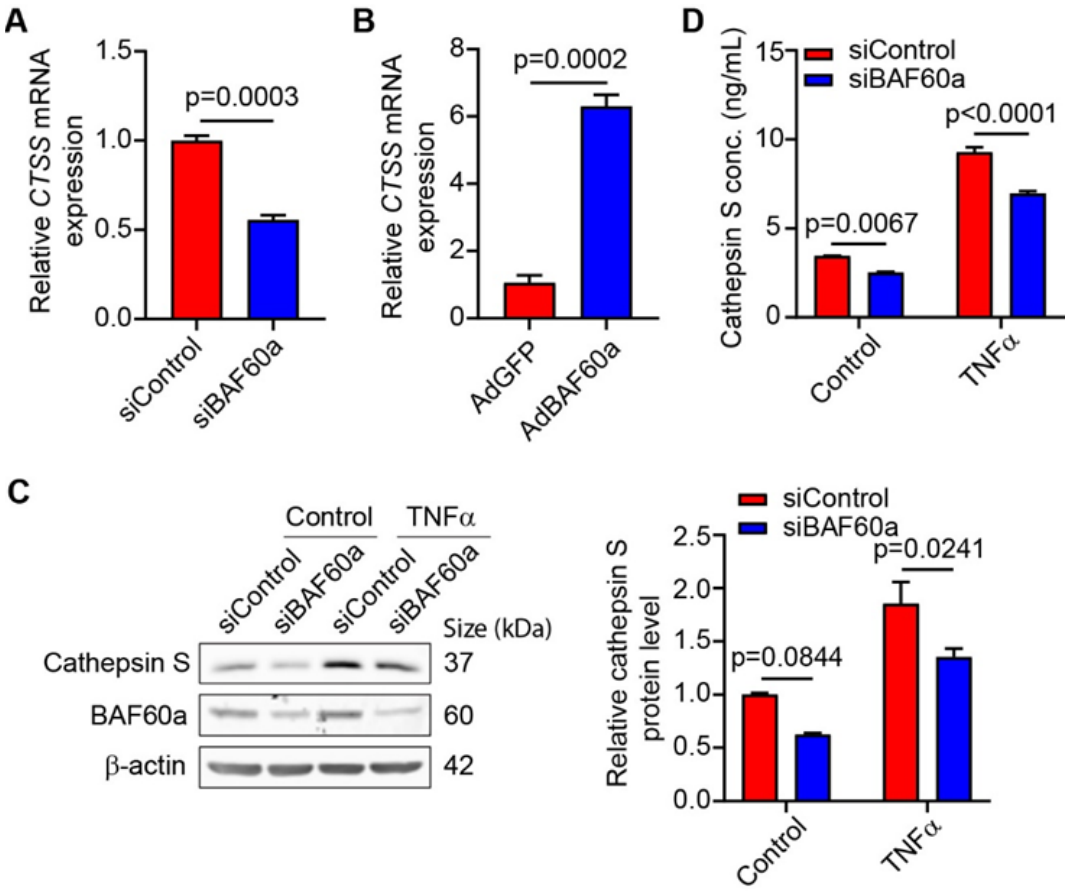


Figure 3.8 BAF60a regulates Cathepsin S expression in VSMCs

A, HASMCs were transfected with siControl or siBAF60a (30 nM). After 72 hours, CTSS mRNA expression was determined by qPCR. n=3. B, HASMCs were infected with AdGFP or AdBAF60a (30 MOI). After 48 hours, CTSS mRNA expression was determined by qPCR. n=3. C-D, HASMCs were transfected with siControl or siBAF60a (30 nM). After 48 hours, cells were treated with or without TNFα (20 ng/ml) for 24h. C, Cathepsin S protein level was determined by Western blot. n=3. D, Cathepsin S concentration in the cultured media was measured by ELISA. n=3. Data are presented as mean ± SEM. Student's t-test for A-B, two-way-ANOVA followed by Holm-Sidak post hoc analysis for C-D.

3.4.9 BAF60a is required for SWI/SNF recruitment to the promoters of NF-κB target genes

As the NF-κB family of transcription factors plays a central role in inflammatory gene expression during the immune response, regulation of the NF-κB pathway is crucial to maintain cellular homeostasis upon environmental stimuli. To address whether BAF60a mediates SWI/SNF-dependent chromatin remodeling to facilitate NF-κB target gene transcription[203], we performed chromatin immunoprecipitation followed by sequencing (ChIP-seq) for BRG1 in HASMCs transfected with either siBAF60a or siControl. This study discovered 8699 genome-wide binding sites for BRG1 (Fig. 3.9 A). Compared with the siControl group, BAF60a knockdown in HASMCs resulted in significantly decreased BRG1 genomic binding (Fig. 3.9 A) without altering the protein abundance of BRG1 or other core SWI/SNF subunits (Data not shown). Next, we plotted the binding of BRG1 within a ±3kb region surrounding the transcription start site (TSS) of NF-κB target genes, according to a recently published database (http://www.bu.edu/nf-kb/gene-resources/target-genes/). Similarly, the knockdown of BAF60a in HASMCs resulted in a significantly decreased enrichment of BRG1 around the TSS of NF-κB target genes (Fig. 3.9 B). Through ChIP-seq, we also examined changes in the histone modification markers H3K9Ac and H3K27Ac. Two chromatin signatures were reported to be enriched at active promoters[204, 205]. In addition, a decreased binding of H3K9Ac was identified around the TSS of NF-κB target genes, in concert with the impaired activation of the NF-κB pathway (Fig. 3.9 C). Then we performed the ChIP assay in primary aortic smooth muscle cells[188] isolated from BAF60a$^{f/f}$ and BAF60a^{SMKO} mice, and reduced binding of BRG1 was identified in the promoters of several NF-κB target genes (Fig. 3.9 D).

To further explore the mechanism of BAF60a-dependent regulation of cathepsin S expression, we analyzed the BRG1 ChIP-seq data and identified a significantly reduced signal at the promoter region of the CTSS gene upon knockdown of BAF60a in HASMCs (Fig. 3.9 E). Similarly, the silencing of BAF60a resulted in a suppressed enrichment of the activation histone marker H3K9Ac within the CTSS promoter (Fig. 3.9 E), indicating impaired transcription. Further investigation uncovered that p65 accumulation to the CTSS promoter induced by TNFα was significantly dampened upon silencing of BAF60a in VSMCs (Fig. 3.9 F). These data indicate CTSS as a novel direct target of p65 regulated by BAF60a-dependent recruitment of the SWI/SNF complex to the promoter. As one of the best-characterized co-factors of NF-κB, p300, a member of the histone acetyltransferase (HAT) family, is associated with increased transcription of inflammatory response genes[206]. Besides, previous reports have demonstrated a physical interaction between the SWI/SNF complex and p300, suggesting a synergistic role of these chromatin remodelers in modulating transcription factor accessibility[207, 208]. Consequently, we performed co-immunoprecipitation (co-IP) and found that p300 interacts with both BAF60a and BRG1 in cultured HASMCs (Fig. 3.9 G). Knockdown of BAF60a in HASMCs significantly reduced the interaction between p300 and BRG1 (Fig. 3.9 H), which may explain the reduced histone acetylation. These data indicate that BAF60a is required for SWI/SNF recruitment in mediating NF-κB target gene expression in VSMC inflammation.

In summary, our data prove that loss of BAF60a in VSMCs impaired NF-κB transcriptional activity and reduced cysteine protease cathepsin S expression, thus protecting from AAA formation by simultaneously inhibiting ECM degradation and reducing the overall inflammatory response.

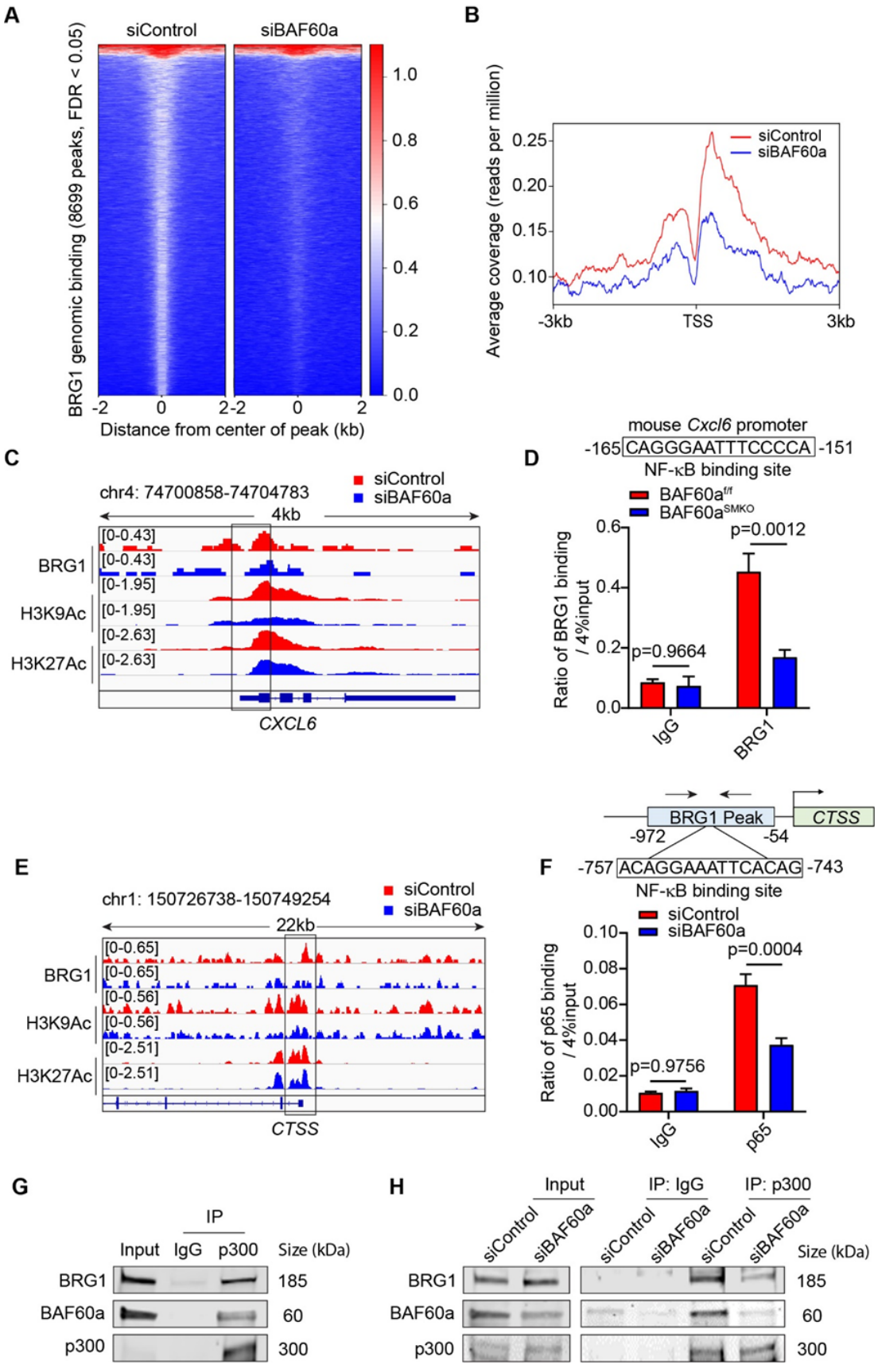

A
siControl
siBAF60a
BRG1 genomic binding (8699 peaks, FDR < 0.05)
1.0
0.8
0.6
0.4
0.2
0.0
-2
0
2
Distance from center of peak (kb)
B
Average coverage (reads per million)
siControl
siBAF60a
0.25
0.20
0.15
0.10
-3kb
TSS
3kb
C
chr4: 74700858-74704783
siControl
siBAF60a
4kb
BRG1
H3K9Ac
H3K27Ac
[0-0.43]
[0-1.95]
[0-2.63]
CXCL6
D
mouse Cxcl6 promoter
-165 CAGGGAATTTCCCCA -151
NF-κB binding site
BAF60af/f
BAF60aSMKO
Ratio of BRG1 binding / 4%input
p=0.9664
p=0.0012
IgG
BRG1
E
chr1: 150726738-150749254
siControl
siBAF60a
22kb
BRG1
H3K9Ac
H3K27Ac
[0-0.65]
[0-0.56]
[0-2.51]
CTSS
F
BRG1 Peak
CTSS
-972
-54
-757 ACAGGAAATTCACAG -743
NF-κB binding site
siControl
siBAF60a
Ratio of p65 binding / 4%input
p=0.9756
p=0.0004
IgG
p65
G
IP
Input
IgG
p300
Size (kDa)
BRG1
BAF60a
p300
185
60
300
H
Input
IP: IgG
IP: p300
siControl
siBAF60a
Size (kDa)
BRG1
BAF60a
p300
185
60
300

Figure 3.9 BAF60a is required for SWI/SNF recruitment to the promoters of NF-κB target genes

A-C and E, HASMCs were transfected with siControl or siBAF60a (30 nM). After 72 hours, ChIP-seq was performed for BRG1, H3K9Ac and H3K27Ac. A, BRG1 genomic binding on target sites within a ±2kb range centered on each peak is presented as a heatmap. B, Histogram of ChIP-seq reads of BRG1 ±3kb surrounding the TSS of NF-κB target genes. C, Normalized ChIP-seq reads of BRG1, H3K9Ac, and H3K27Ac in the CXCL6 gene promoter and coding region are shown in IGV. D, BRG1 binding on the NF-κB binding site in the mouse Cxcl6 promoter was detected by ChIP assay in primary aortic smooth muscle cells isolated from abdominal aortas of BAF60af/f and BAF60aSMKO mice. n=3. E, Normalized ChIP-seq reads of BRG1, H3K9Ac, and H3K27Ac around the TSS of the CTSS gene shown in IGV. F, p65 binding on the NF-κB binding site located in the CTSS promoter was detected by ChIP assay in HASMCs transfected with 30 nM siControl or siBAF60a for 72h followed by 1h treatment with TNFα (20 ng/ml). n=3. G, Physical interaction between p300, BRG1, and BAF60a in cultured HASMCs was detected by Co-IP. IgG was used as the negative control. n=3. H, HASMCs were transfected with siControl or siBAF60a (30 nM). After 72 hours, physical interaction between p300 and BRG1 was detected by Co-IP. IgG was used as the negative control. n=3. Data are presented as mean ± SEM. Two-way-ANOVA followed by Holm-Sidak post hoc analysis for D and F.

3.5 Discussion

Although the SWI/SNF chromatin remodeling complex has been demonstrated to be an essential regulator of many chromatin accessibility checkpoints for maintaining cellular homeostasis in various human diseases[43, 175], its role in the biology and pathophysiology of the vasculature remains largely unknown. The mutually exclusive incorporation of BAF60 family members (BAF60a, b and c) into distinct SWI/SNF complexes suggests different biological functions: BAF60a regulates fatty acid oxidation and cholesterol homeostasis, while BAF60c involves in glucose metabolism[153]. BAF60a is the only 60-kDa subunit involved in all three mammalian SWI/SNF assemblies, including canonical BAF (cBAF), polybromo-associated BAF (PBAF), and non-canonical BAF (ncBAF)[209], its role in vascular biology, however, remains unexplored. Our results here show that loss of BAF60a in VSMCs protected mice from AngII- and elastase-induced AAA formation by suppressing vascular inflammation and ECM degradation, which sheds new light on the molecular mechanisms of this disease. In this study, BAF60a was found to be required for recruiting the catalytic subunit BRG1 of the SWI/SNF complex to the promoter of NF-κB target genes, underscoring the critical role of BAF60a in regulating VSMC inflammatory response. Furthermore, we uncovered that NF-κB regulates the expression of cathepsin S in a BAF60a-dependent fashion, thus providing the first evidence that NF-κB/BAF60a regulate the VSMC inflammatory response and the ECM remodeling, two hallmark features of AAA concurrently.

The transcription factors of the NF-κB family regulate a significant fraction of the inflammatory transcriptome. According to the kinetics of transcription activation, NF-κB target genes can be divided into two classes: primary response genes with chromatin landscape poised for immediate activation, such as TNF; and secondary response genes with delayed transcription,

such as most of the cytokines and chemokines, with promoters that are frequently found to contain a positioned nucleosome overlapping the TATA box[210]. In this scenario, chromatin remodelers, such as the SWI/SNF complex, which alters DNA/histone contacts, are essential to increase the accessibility of transcription. BRG1, the catalytic subunit of the SWI/SNF complex, contained a DNA-dependent ATPase domain and was shown to cooperate with other co-factors, such as histone acetyltransferase (HAT), to configure the chromatin and facilitate NF-κB target gene expression[203]. In this study, by performing ChIP-seq, we identified BAF60a as a bridge able to recruit BRG1 in the SWI/SNF complex to the transcriptional target genes of NF-κB. Silencing of BAF60a in HASMCs resulted in a noticeable decrease in BRG1 genome-wide occupancy, especially within a 6-kb region around the TSS of NF-κB-dependent secondary response genes, without altering the expression of primary response genes. As one of the best co-factors of NF-κB, p300 functions as an acetyltransferase to enhance transcriptional activity through the acetylation of p65 and histones residing in the promoters[204]. Acetylated p65 presents stabilized binding to DNA and suppressed interaction with IkBα, leading to enhanced NF-κB transcription activation.[206] Interestingly, this study identified a physical interaction between BAF60a and p300. Based on our observations, we proposed a novel model for the BAF60a-dependent regulation of NF-κB transcription of inflammatory genes (mainly secondary response genes) where BAF60a plays a central role in linking NF-κB transcriptional co-factors with the SWI/SNF chromatin remodeling complex (Fig. 3.10).

In summary, through the use of VSMC-specific BAF60a-deficient mice in AngII- and elastase-induced murine aneurysm models, our study demonstrates for the first time that BAF60a regulates inflammatory signaling and cysteine protease cathepsin S expression in VSMCs, crucial in AAA development. Mechanistically, BAF60a regulates inflammatory gene expression

in VSMCs by recruiting the SWI/SNF chromatin remodeling complex to the promoter of NF-κB target genes and interacting with the NF-κB transcriptional co-factor p300. Of relevance, it is remarkable that targeting individual genes or pathways has failed to translate into clinically relevant drugs so far. A coordinated, genome-wide chromatin remodeling, such as that uncovered here for BAF60a in response to stimuli from AAA risk factors, could help explain the paucity of favorable results for targeted treatments in AAA. As local and tissue-specific delivery strategies continue to develop, inhibition of VSMC BAF60a may eventually contribute to the pharmacological treatment of AAA and other inflammatory diseases of the vascular wall.

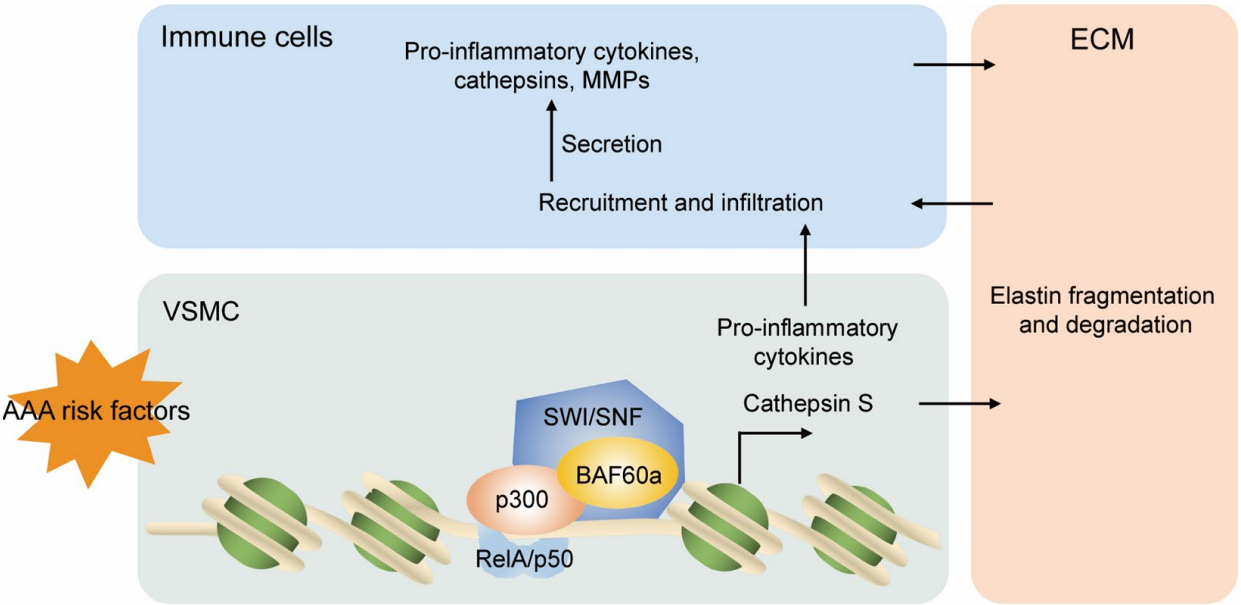


Figure 3.10 Schematic model of BAF60a regulation of VSMC inflammation and ECM degradation in AAA development.

VSMC, vascular smooth muscle cells; ECM, extracellular matrix; MMPs, matrix metalloproteinase.

Chapter 4 Summary and Perspectives

4.1 Summary

As the leading cause of death globally, cardiovascular diseases (CVDs) are caused by hereditary and environmental factors. Additionally, many vascular pathological changes have been linked to the epigenetic modification of disease-associated genes. In response to internal and external cellular settings, these modifications by chromatin remodeling complexes change DNA accessibility and chromatin structure to influence gene expression.

Complicated disease settings context-dependently affect how chromatin remodeling and transcription machinery interact with each other to cause changes in gene expression that are cell-type specific. Immune cells are crucial in atherosclerosis. We found that BAF60a is positively linked with mitochondria-high macrophages in human plaques and is downregulated in mouse atherosclerotic macrophages. Inducing macrophage toxicity and apoptosis, dampening mitochondrial integrity, promoting monocyte adhesion, and aggravating murine plaque development are all effects of myeloid BAF60a deletion. Mechanistically, we discovered that BAF60a maintains NRF1 accessibility to the promoters of crucial nuclear mitochondrial genes in a way that is SWI/SNF complex-dependent. Functional compensation of BAF60a deficiency-induced macrophage mitochondria dysfunction can be achieved by overexpressing NRF1.

Changes to VSMCs may be responsible for the underlying mechanism of many vascular disorders, such as AAA. We investigated the impact of BAF60a loss on AAA formation in VSMCs. BAF60a is elevated in aneurysm lesions in both human and experimental mice. VSMC-specific BAF60a deletion prevented mice from developing AAA in vivo. This was associated

with significantly reduced vascular inflammation, monocyte infiltration, and elastin fragmentation. By luring BRG1 to the promoter region of NF-κB target genes, BAF60a controls VSMC inflammation. Degradation of ECM was also improved by BAF60a deficiency in VSMCs through inhibition of the CTSS.

Our work showed the importance of the BAF60a-Transcription Factor interaction in macrophages in the fight against atherosclerosis and revealed the need for BAF60a in the recruitment of the SWI/SNF complex to enable the epigenetic control of VSMC inflammation in AAA. BAF60a's involvement in vascular disorders, including atherosclerosis and AAA, is highly cell-type and context-dependent, which points to functional compensation of aberrant epigenetic-disease interaction as possible therapeutic targets.

4.2 Perspective

4.2.1 Generation and characterization of a sex-independent smooth muscle-targeted inducible Cre recombinase mouse model

Smooth muscle cells (SMCs) are enriched and play essential roles in forming and maintaining the physiological function in hollow structured tissues widely distributed in the blood vessel, bladder, intestine, uterus, stomach, and other organs. As one of the major cell types being focused on in the vasculature studies, SMCs displayed potent plasticity. Therefore, alterations of SMCs could take charge of the underlying mechanism of various cardiovascular diseases (CVDs). To understand the functional genes in SMCs, so as the corresponding CVDs, we and others have developed several transgenic Cre knock-in (KI) mice models driven by SMC-specific promoters [211-214]. These Cre-bearing mice enable targeted deletion of specific genes by crossbreeding with corresponding loxP-flanked mice. In addition, by fusing with a modified estrogen receptor, the Cre-ERT2 mice also allow a controlled deletion of the gene of interest in a spatial and temporal-dependent manner. One of the SMC-specific tamoxifen-inducible Cre models, the SMMHC-CreERT2 transgenic mice, has been extensively used to characterize gene functions in vasculature and CVDs[212] was also used in Chapter 3 for the BAF60a VSMC study. However, given that the SMMHC-CreERT2 transgene is located on the Y-chromosome, its application is limited to only the male sex. As the number one cause of death, although CVDs were generally and traditionally thought to be more prevalent in men and have less incidence in pre-menopause women, it has been more explicit that CVDs were a leading cause of death in women. Indeed, the pathophysiological difference between men and women patients and the lack of sex-oriented study would underestimate the degree of CVD risks in

women and leave women in an inequity position that is more likely to suffer from inadequate treatment.

Herein, we developed a new Myh11-CreERT2 KI mouse model by CRISPR/Cas9 mediated double break and homologous recombination between the donor vector containing the CreERT2-P2A sequence and the homologous arm flanking the ATG transcription start site at exon 2 of the endogenous Myh11 gene. Adding the P2A self-cleaving peptide ensures the production of a bi-cistronic mRNA transcript that will translate both CreERT2 and intact Myh11 proteins[215]. The corresponding donor assembly, sgRNA containing Cas9 plasmid, was microinjected into fertilized mouse eggs of C57BL/6XSJL origin, followed by identifying founder mice, genotyping, and sequencing of offspring (Fig. 4.1 A). PCR primers targeting potential off-target sites identified no off-target cleavage. Heterozygote male founders were backcrossed to the C57BL/6J background female for multiple generations before the Cre efficiency and specificity characterization. The Myh11-CreERT2 KI mice appear normal and fertile. Furthermore, the insertion of the Myh11- CreERT2 showed minimal effect on the endogenous Myh11 gene expression in multiple SMC-enriched tissues. Smooth muscle functions remain mostly intact. As a demonstration, the systolic blood pressure is identical among the wildtype (Myh11-CreERT2$^{-/-}$), heterozygotes (Myh11-CreERT2$^{+/-}$), and homozygotes (Myh11-CreERT2$^{+/+}$) mice. Offspring from heterozygotes crossbreeding recapitulates that of a standard mendelian distribution at a ratio of 7:10:6 for the Myh11-CreERT2$^{-/-}$, Myh11-CreERT2$^{+/-}$, and Myh11-CreERT2$^{+/+}$ mice respectively (Fig. 4.1 B).

In addition, to visually inspect the Cre recombinase activity at the tissue level, we crossbred the Myh11-CreERT2$^{+/-}$ mice with an mT/mG reporter mouse (JAX # 007676) and injected them with tamoxifen as previously described[211]. Frozen sections from the reporter

Myh11-CreERT2$^{+/-}$ mice showed increased EGFP fluorescence (green) and a decreased tdTomato fluorescence (red) in the SMC portion of the aorta, bladder, and intestine. The Cre recombinase activity was smooth muscle-specific and did not appear in cardiomyocytes or skeletal muscles (Fig. 4.1 C). Protein isolated from SMC-enriched aorta, bladder, and intestine confirmed the existence of EGFP protein in the reporter Myh11-CreERT2$^{+/-}$ mice, with expression levels comparable in both male and female sexes (Fig. 4.1 D). Utilizing an additional LacZ reporter mice model (JAX #003474), we confirmed the specificity of the tamoxifen-inducible Cre by β-galactosidase staining without the interference of tissue autofluorescence. For example, the blue stains are restricted to the brain vasculature and only appear with tamoxifen injection (Fig. 4.1 E). Lastly, to quantitatively calculate the gene knockout efficiency, Myh11-CreERT2$^{+/-}$ mice were crossbred to the Baf60a floxed mice, and Baf60a gene expression from Baf60aflox/flox mice with or without Cre was quantified and normalized by Myh11 level. Compared to the control, the Myh11-CreERT2$^{+/-}$ mice displayed a significant reduction of Baf60a in SMCs, including but not limited to those in the aorta and bladder (Fig. 4.1 F).

In summary, we report a novel Myh11-CreERT2 KI mice line that displays an inducible Cre recombinase activity in an SMC-dependent manner. The Myh11-CreERT2 showed comparable efficiency and specificity with the most widely used SMMHC-CreERT2 KI mice line. At the same time, the endogenous Myh11-driven CreERT2 located at chromosome 16 is sex-independent. It thus allows for sex-oriented studies that are compatible with both male and female mice. The Myh11-CreERT2 KI mice model will be valuable to address better underestimated SMCs and cardiovascular-related diseases in the female sex and aid in understanding VSMC-specific BAF60a in female aneurysm conditions.

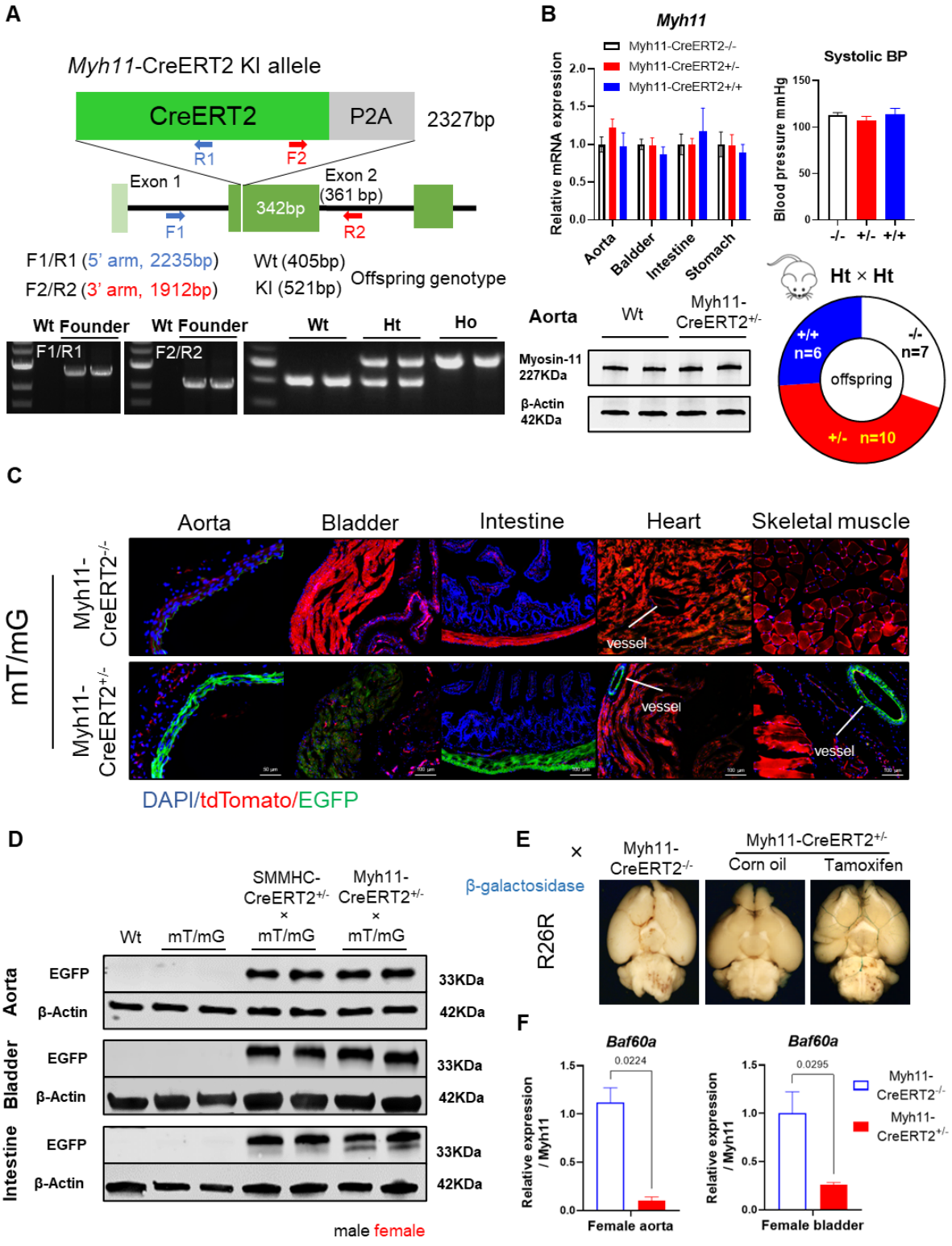

A
Myh11-CreERT2 KI allele
CreERT2
P2A
2327bp
R1
F2
Exon 1
Exon 2
(361 bp)
342bp
F1
R2
F1/R1 (5' arm, 2235bp)
F2/R2 (3' arm, 1912bp)
Wt (405bp)
KI (521bp)
Offspring genotype
Wt Founder
Wt Founder
Wt
Ht
Ho
F1/R1
F2/R2
B
Myh11
Myh11-CreERT2-/-
Myh11-CreERT2+/-
Myh11-CreERT2+/+
Relative mRNA expression
Aorta
Baldder
Intestine
Stomach
Systolic BP
Blood pressure mmHg
-/-
+/-
+/+
Aorta
Wt
Myh11-CreERT2+/-
Myosin-11
227KDa
β-Actin
42KDa
Ht × Ht
+/+
n=6
-/-
n=7
offspring
+/-
n=10
C
Aorta
Bladder
Intestine
Heart
Skeletal muscle
mT/mG
Myh11-CreERT2-/-
Myh11-CreERT2+/-
vessel
vessel
vessel
DAPI/tdTomato/EGFP
D
SMMHC-CreERT2+/-
×
mT/mG
Myh11-CreERT2+/-
×
mT/mG
Wt
mT/mG
Aorta
EGFP
β-Actin
33KDa
42KDa
Bladder
EGFP
β-Actin
33KDa
42KDa
Intestine
EGFP
β-Actin
33KDa
42KDa
male female
E
×
Myh11-CreERT2-/-
Myh11-CreERT2+/-
Corn oil
Tamoxifen
β-galactosidase
R26R
F
Baf60a
0.0224
Relative expression / Myh11
Female aorta
Baf60a
0.0295
Relative expression / Myh11
Female bladder
Myh11-CreERT2-/-
Myh11-CreERT2+/-

Figure 4.1 Generation and characterization of a sex-independent smooth muscle-targeted inducible Cre recombinase mouse model.

A, Schematic illustration of donor vector and insertion site by CRISPR/Cas9 mediated knockin followed by PCR confirmation of founders and offspring. B, Knockin effect on endogenous Myh11 expression level, subsequent smooth muscle function (blood pressure), and Mendelian distribution in offspring. (N=6, 7 and 10 for +/+, -/- and +/- group, respectively) C, Frozen tissue sections from Myh11-CreERT2$^{+/-}$ mice crossbred with ROSA26 driven mT/mG reporter mice (JAX #007676). The Cre activity is reported by tdTomato (Red) signal loss and EGFP (Green) signal gain. D, Western-blot quantification of EGFP in various smooth muscle cell-enriched tissues. E, β-galactosidase (Blue) staining shows the specificity and intrinsic activity of inducible Cre recombinase after breeding Myh11-CreERT2$^{+/-}$ mice to LacZ reporter mice (JAX #003474), with or without tamoxifen treatment. F, Quantitative calculation of Myh11-CreERT2$^{+/-}$ mediated knockout efficiency by qPCR of the aorta and bladder cDNA from Myh11-CreERT2$^{+/-}$ mice bred with BAF60A$^{flox/flox}$ mice (N=3/group). Data are presented as mean ± SEM. Student's t-test for F.

4.2.2 The three-way balance between BAF60a, b, and c

The BAF60 family consists of three subunits of the SWItch/Sucrose Non-Fermentable (SWI/SNF) chromatin remodeling complex: BAF60a, b, and c. Interacting with distinct transcription factors, BAF60a, b, and c seem to mediate the mutually exclusive recruitment of SWI/SNF complex to specific promoters. We hypothesized that BAF60a, BAF60b, and BAF60c might drive the homeostasis or pathological response of cells in vascular disorders in a three-way manner. Due to their unique interaction with SWI/SNF, the consequences of each specific BAF60 deficiency may occur from their relative expression in response to inputs from the diverse risk factors. Disruption of this balance by varied and potentially changing combinations of risk factor-associated local inputs might result in disparate, presumably negative results. Remarkably, the majority of investigations so far have focused on individual BAF60 subunits. The results reflected the combined impacts of the changed subunit itself and the relatively increased recruitment of the other two subunits associated with SWI/SNF signaling, preventing us from comprehending their individual and simultaneous effects on the disease outcomes. Although with significant challenges, future studies should investigate how the different BAF60 subunits coordinate the transcriptome and cell homeostasis in the vascular disease milieu.

4.3 Concluding remarks

In this dissertation, I showed that BAF60a is a crucial chromatin remodeler subunit to maintain essential vascular homeostasis, eliciting bidirectional and cell-dependent crosstalk with transcription factors to regulate disease response genes. Furthermore, BAF60a maintains mitochondrial integrity in macrophages under atherosclerosis while promoting vascular smooth muscle cell inflammation in aortic aneurysms. This work offers a fresh understanding of the molecular processes behind cardiovascular disease and prospective therapeutic targets.

Bibliography

1. Flora, G.D. and M.K. Nayak, *A Brief Review of Cardiovascular Diseases, Associated Risk Factors and Current Treatment Regimes.* Curr Pharm Des, 2019. **25**(38): p. 4063-4084.
2. Bjorkegren, J.L.M. and A.J. Lusis, *Atherosclerosis: Recent developments.* Cell, 2022. **185**(10): p. 1630-1645.
3. Libby, P., *The biology of atherosclerosis comes full circle: lessons for conquering cardiovascular disease.* Nat Rev Cardiol, 2021. **18**(10): p. 683-684.
4. Forteza, M.J. and D.F.J. Ketelhuth, *Metabolism in atherosclerotic plaques: immunoregulatory mechanisms in the arterial wall.* Clin Sci (Lond), 2022. **136**(6): p. 435-454.
5. Pagler, T.A., et al., *Deletion of ABCA1 and ABCG1 impairs macrophage migration because of increased Rac1 signaling.* Circ Res, 2011. **108**(2): p. 194-200.
6. Tomas, L., et al., *Altered metabolism distinguishes high-risk from stable carotid atherosclerotic plaques.* Eur Heart J, 2018. **39**(24): p. 2301-2310.
7. Van den Bossche, J., J. Baardman, and M.P.J. de Winther, *Metabolic Characterization of Polarized M1 and M2 Bone Marrow-derived Macrophages Using Real-time Extracellular Flux Analysis.* Jove-Journal of Visualized Experiments, 2015(105).
8. Xie, N., et al., *NAD(+) metabolism: pathophysiologic mechanisms and therapeutic potential.* Signal Transduct Target Ther, 2020. **5**(1): p. 227.
9. Zernecke, A., et al., *Meta-Analysis of Leukocyte Diversity in Atherosclerotic Mouse Aortas.* Circ Res, 2020. **127**(3): p. 402-426.
10. Tarnick, M., *[Acrodermatosis caused by Ornithonyssus bacoti Hirst (tropical rat mite)].* Dermatol Monatsschr, 1987. **173**(5): p. 272-5.
11. Pinard, A., G.T. Jones, and D.M. Milewicz, *Genetics of Thoracic and Abdominal Aortic Diseases.* Circ Res, 2019. **124**(4): p. 588-606.
12. Jones, G.T., et al., *Meta-Analysis of Genome-Wide Association Studies for Abdominal Aortic Aneurysm Identifies Four New Disease-Specific Risk Loci.* Circ Res, 2017. **120**(2): p. 341-353.
13. Multicentre Aneurysm Screening Study, G., *Multicentre aneurysm screening study (MASS): cost effectiveness analysis of screening for abdominal aortic aneurysms based on four year results from randomised controlled trial.* BMJ, 2002. **325**(7373): p. 1135.
14. Soden, P.A., et al., *Outcomes for symptomatic abdominal aortic aneurysms in the American College of Surgeons National Surgical Quality Improvement Program.* J Vasc Surg, 2016. **64**(2): p. 297-305.
15. Golledge, J., *Abdominal aortic aneurysm: update on pathogenesis and medical treatments.* Nat Rev Cardiol, 2019. **16**(4): p. 225-242.
16. Yoshimura, K., et al., *Current Status and Perspectives on Pharmacologic Therapy for Abdominal Aortic Aneurysm.* Curr Drug Targets, 2018. **19**(11): p. 1265-1275.

17. He, L., et al., *Deficiency of FAM3D (Family With Sequence Similarity 3, Member D), A Novel Chemokine, Attenuates Neutrophil Recruitment and Ameliorates Abdominal Aortic Aneurysm Development.* Arterioscler Thromb Vasc Biol, 2018. **38**(7): p. 1616-1631.
18. Liu, J., A. Daugherty, and H. Lu, *Angiotensin II and Abdominal Aortic Aneurysms: An update.* Curr Pharm Des, 2015. **21**(28): p. 4035-48.
19. Lindeman, J.H. and J.S. Matsumura, *Pharmacologic Management of Aneurysms.* Circ Res, 2019. **124**(4): p. 631-646.
20. Swerdlow, N.J., W.W. Wu, and M.L. Schermerhorn, *Open and Endovascular Management of Aortic Aneurysms.* Circ Res, 2019. **124**(4): p. 647-661.
21. Feinberg, A.P., *The Key Role of Epigenetics in Human Disease Prevention and Mitigation.* N Engl J Med, 2018. **378**(14): p. 1323-1334.
22. Shi, Y., et al., *Epigenetic regulation in cardiovascular disease: mechanisms and advances in clinical trials.* Signal Transduct Target Ther, 2022. **7**(1): p. 200.
23. Kornberg, R.D. and Y. Lorch, *Twenty-five years of the nucleosome, fundamental particle of the eukaryote chromosome.* Cell, 1999. **98**(3): p. 285-94.
24. Allis, C.D. and T. Jenuwein, *The molecular hallmarks of epigenetic control.* Nat Rev Genet, 2016. **17**(8): p. 487-500.
25. Morrison, A.J., *Chromatin-remodeling links metabolic signaling to gene expression.* Mol Metab, 2020. **38**: p. 100973.
26. Gaspar-Maia, A., et al., *Open chromatin in pluripotency and reprogramming.* Nat Rev Mol Cell Biol, 2011. **12**(1): p. 36-47.
27. Li, W. and A.A. Mills, *Architects of the genome: CHD dysfunction in cancer, developmental disorders and neurological syndromes.* Epigenomics, 2014. **6**(4): p. 381-95.
28. Nodelman, I.M. and G.D. Bowman, *Biophysics of Chromatin Remodeling.* Annu Rev Biophys, 2021. **50**: p. 73-93.
29. Kadoch, C. and G.R. Crabtree, *Mammalian SWI/SNF chromatin remodeling complexes and cancer: Mechanistic insights gained from human genomics.* Sci Adv, 2015. **1**(5): p. e1500447.
30. Bartholomew, B., *Regulating the chromatin landscape: structural and mechanistic perspectives.* Annu Rev Biochem, 2014. **83**: p. 671-96.
31. Clapier, C.R., et al., *Mechanisms of action and regulation of ATP-dependent chromatin-remodelling complexes.* Nat Rev Mol Cell Biol, 2017. **18**(7): p. 407-422.
32. Narlikar, G.J., R. Sundaramoorthy, and T. Owen-Hughes, *Mechanisms and functions of ATP-dependent chromatin-remodeling enzymes.* Cell, 2013. **154**(3): p. 490-503.
33. Neigeborn, L. and M. Carlson, *Genes affecting the regulation of SUC2 gene expression by glucose repression in Saccharomyces cerevisiae.* Genetics, 1984. **108**(4): p. 845-58.
34. Stern, M., R. Jensen, and I. Herskowitz, *Five SWI genes are required for expression of the HO gene in yeast.* J Mol Biol, 1984. **178**(4): p. 853-68.
35. Cote, J., et al., *Stimulation of GAL4 derivative binding to nucleosomal DNA by the yeast SWI/SNF complex.* Science, 1994. **265**(5168): p. 53-60.
36. Smith, C.L., et al., *Structural analysis of the yeast SWI/SNF chromatin remodeling complex.* Nat Struct Biol, 2003. **10**(2): p. 141-5.
37. Tamkun, J.W., et al., *brahma: a regulator of Drosophila homeotic genes structurally related to the yeast transcriptional activator SNF2/SWI2.* Cell, 1992. **68**(3): p. 561-72.

38. Chiba, H., et al., *Two human homologues of Saccharomyces cerevisiae SWI2/SNF2 and Drosophila brahma are transcriptional coactivators cooperating with the estrogen receptor and the retinoic acid receptor.* Nucleic Acids Res, 1994. **22**(10): p. 1815-20.
39. Centore, R.C., et al., *Mammalian SWI/SNF Chromatin Remodeling Complexes: Emerging Mechanisms and Therapeutic Strategies.* Trends Genet, 2020. **36**(12): p. 936-950.
40. Alpsoy, A. and E.C. Dykhuizen, *Glioma tumor suppressor candidate region gene 1 (GLTSCR1) and its paralog GLTSCR1-like form SWI/SNF chromatin remodeling subcomplexes.* J Biol Chem, 2018. **293**(11): p. 3892-3903.
41. Michel, B.C., et al., *A non-canonical SWI/SNF complex is a synthetic lethal target in cancers driven by BAF complex perturbation.* Nature Cell Biology, 2018. **20**(12): p. 1410-+.
42. Rafati, H., et al., *Repressive LTR Nucleosome Positioning by the BAF Complex Is Required for HIV Latency.* Plos Biology, 2011. **9**(11).
43. Kadoch, C., et al., *Proteomic and bioinformatic analysis of mammalian SWI/SNF complexes identifies extensive roles in human malignancy.* Nat Genet, 2013. **45**(6): p. 592-601.
44. Biegel, J.A., et al., *Germ-line and acquired mutations of INI1 in atypical teratoid and rhabdoid tumors.* Cancer Res, 1999. **59**(1): p. 74-9.
45. Roberts, C.W., et al., *Haploinsufficiency of Snf5 (integrase interactor 1) predisposes to malignant rhabdoid tumors in mice.* Proc Natl Acad Sci U S A, 2000. **97**(25): p. 13796-800.
46. Sullivan, L.M., et al., *Epithelioid sarcoma is associated with a high percentage of SMARCB1 deletions.* Modern Pathology, 2013. **26**(3): p. 385-392.
47. Bevilacqua, A., M.S. Willis, and S.J. Bultman, *SWI/SNF chromatin-remodeling complexes in cardiovascular development and disease.* Cardiovasc Pathol, 2014. **23**(2): p. 85-91.
48. Hang, C.T., et al., *Chromatin regulation by Brg1 underlies heart muscle development and disease.* Nature, 2010. **466**(7302): p. 62-7.
49. Stankunas, K., et al., *Endocardial Brg1 represses ADAMTS1 to maintain the microenvironment for myocardial morphogenesis.* Dev Cell, 2008. **14**(2): p. 298-311.
50. Lei, I., et al., *SWI/SNF protein component BAF250a regulates cardiac progenitor cell differentiation by modulating chromatin accessibility during second heart field development.* J Biol Chem, 2012. **287**(29): p. 24255-62.
51. Stenina-Adognravi, O., *Thrombospondins: old players, new games.* Curr Opin Lipidol, 2013. **24**(5): p. 401-9.
52. Lynch, J.M., et al., *A thrombospondin-dependent pathway for a protective ER stress response.* Cell, 2012. **149**(6): p. 1257-68.
53. Huang, X.L., et al., *Coronary development is regulated by ATP-dependent SWI/SNF chromatin remodeling component BAF180.* Developmental Biology, 2008. **319**(2): p. 258-266.
54. Wang, Z., et al., *Polybromo protein BAF180 functions in mammalian cardiac chamber maturation.* Genes Dev, 2004. **18**(24): p. 3106-16.
55. He, L.J., et al., *BAF200 Is Required for Heart Morphogenesis and Coronary Artery Development.* Plos One, 2014. **9**(10).

56. Zhao, G., et al., *BAF60c prevents abdominal aortic aneurysm formation through epigenetic control of vascular smooth muscle cell homeostasis.* J Clin Invest, 2022.
57. Sokpor, G., et al., *Chromatin Remodeling BAF (SWI/SNF) Complexes in Neural Development and Disorders.* Frontiers in Molecular Neuroscience, 2017. **10**.
58. Tsurusaki, Y., et al., *Mutations affecting components of the SWI/SNF complex cause Coffin-Siris syndrome.* Nature Genetics, 2012. **44**(4): p. 376-378.
59. Neale, B.M., et al., *Patterns and rates of exonic de novo mutations in autism spectrum disorders.* Nature, 2012. **485**(7397): p. 242-U129.
60. Santen, G.W.E., et al., *Coffin-Siris Syndrome and the BAF Complex: Genotype-Phenotype Study in 63 Patients.* Human Mutation, 2013. **34**(11): p. 1519-1528.
61. Wieczorek, D., et al., *A comprehensive molecular study on Coffin-Siris and Nicolaides-Baraitser syndromes identifies a broad molecular and clinical spectrum converging on altered chromatin remodeling.* Human Molecular Genetics, 2013. **22**(25): p. 5121-5135.
62. Kosho, T., et al., *Clinical Correlations of Mutations Affecting Six Components of the SWI/SNF Complex: Detailed Description of 21 Patients and a Review of the Literature.* American Journal of Medical Genetics Part A, 2013. **161A**(6): p. 1221-1237.
63. Versteege, I., et al., *Truncating mutations of hSNF5/INI1 in aggressive paediatric cancer.* Nature, 1998. **394**(6689): p. 203-206.
64. Kosho, T., N. Okamoto, and I. Coffin-Siris Syndrome, *Genotype-Phenotype Correlation of Coffin-Siris Syndrome Caused by Mutations in SMARCB1, SMARCA4, SMARCE1, and ARID1A.* American Journal of Medical Genetics Part C-Seminars in Medical Genetics, 2014. **166**(3): p. 262-275.
65. Gossai, N., et al., *Report of a patient with a constitutional missense mutation in SMARCB1, Coffin-Siris phenotype, and schwannomatosis.* Am J Med Genet A, 2015. **167A**(12): p. 3186-91.
66. Bachmann, C., et al., *mSWI/SNF (BAF) Complexes Are Indispensable for the Neurogenesis and Development of Embryonic Olfactory Epithelium.* Plos Genetics, 2016. **12**(9).
67. Narayanan, R., et al., *Loss of BAF (mSWI/SNF) Complexes Causes Global Transcriptional and Chromatin State Changes in Forebrain Development.* Cell Rep, 2015. **13**(9): p. 1842-54.
68. Van Houdt, J.K.J., et al., *Heterozygous missense mutations in SMARCA2 cause Nicolaides-Baraitser syndrome.* Nature Genetics, 2012. **44**(4): p. 445-U261.
69. Ejaz, R., R. Babul-Hirji, and D. Chitayat, *The evolving features of Nicolaides-Baraitser syndrome - a clinical report of a 20-year follow-up.* Clinical Case Reports, 2016. **4**(4): p. 351-355.
70. Kleefstra, T., et al., *Loss-of-function mutations in euchromatin histone methyl transferase 1 (EHMT1) cause the 9q34 subtelomeric deletion syndrome.* American Journal of Human Genetics, 2006. **79**(2): p. 370-377.
71. Kleefstra, T., et al., *Disruption of an EHMT1-Associated Chromatin-Modification Module Causes Intellectual Disability.* American Journal of Human Genetics, 2012. **91**(1): p. 73-82.
72. O'Roak, B.J., et al., *Sporadic autism exomes reveal a highly interconnected protein network of de novo mutations.* Nature, 2012. **485**(7397): p. 246-U136.
73. Chesi, A., et al., *Exome sequencing to identify de novo mutations in sporadic ALS trios.* Nature Neuroscience, 2013. **16**(7): p. 851-U98.

74. Koga, M., et al., *Involvement of SMARCA2/BRM in the SWI/SNF chromatin-remodeling complex in schizophrenia.* Human Molecular Genetics, 2009. **18**(13): p. 2483-2494.
75. Basak, A., et al., *BCL11A deletions result in fetal hemoglobin persistence and neurodevelopmental alterations.* Journal of Clinical Investigation, 2015. **125**(6): p. 2363-2368.
76. Wanior, M., et al., *Exploiting vulnerabilities of SWI/SNF chromatin remodelling complexes for cancer therapy.* Oncogene, 2021. **40**(21): p. 3637-3654.
77. Wilson, B.G., et al., *Residual complexes containing SMARCA2 (BRM) underlie the oncogenic drive of SMARCA4 (BRG1) mutation.* Mol Cell Biol, 2014. **34**(6): p. 1136-44.
78. Wang, X., et al., *BRD9 defines a SWI/SNF sub-complex and constitutes a specific vulnerability in malignant rhabdoid tumors.* Nat Commun, 2019. **10**(1): p. 1881.
79. Brien, G.L., et al., *Targeted degradation of BRD9 reverses oncogenic gene expression in synovial sarcoma.* Elife, 2018. **7**.
80. Hoffman, G.R., et al., *Functional epigenetics approach identifies BRM/SMARCA2 as a critical synthetic lethal target in BRG1-deficient cancers.* Proceedings of the National Academy of Sciences of the United States of America, 2014. **111**(8): p. 3128-3133.
81. Oike, T., et al., *A synthetic lethality-based strategy to treat cancers harboring a genetic deficiency in the chromatin remodeling factor BRG1.* Cancer Res, 2013. **73**(17): p. 5508-18.
82. Schick, S., et al., *Systematic characterization of BAF mutations provides insights into intracomplex synthetic lethalities in human cancers.* Nat Genet, 2019. **51**(9): p. 1399-1410.
83. Puri, P.L. and M. Mercola, *BAF60 A, B, and Cs of muscle determination and renewal.* Genes Dev, 2012. **26**(24): p. 2673-83.
84. Hsiao, P.W., et al., *BAF60a mediates critical interactions between nuclear receptors and the BRG1 chromatin-remodeling complex for transactivation.* Mol Cell Biol, 2003. **23**(17): p. 6210-20.
85. Oh, J., et al., *BAF60a interacts with p53 to recruit the SWI/SNF complex.* J Biol Chem, 2008. **283**(18): p. 11924-34.
86. Lee, Y.S., et al., *Chromatin remodeling complex interacts with ADD1/SREBP1c to mediate insulin-dependent regulation of gene expression.* Mol Cell Biol, 2007. **27**(2): p. 438-52.
87. Li, S., et al., *Genome-wide coactivation analysis of PGC-1 alpha identifies BAF60a as a regulator of hepatic lipid metabolism.* Cell Metabolism, 2008. **8**(2): p. 105-117.
88. Meng, Z.X., et al., *A Diet-Sensitive BAF60a-Mediated Pathway Links Hepatic Bile Acid Metabolism to Cholesterol Absorption and Atherosclerosis.* Cell Reports, 2015. **13**(8): p. 1658-1669.
89. Sun, X., et al., *Cardiac-enriched BAF chromatin-remodeling complex subunit Baf60c regulates gene expression programs essential for heart development and function.* Biology Open, 2018. **7**(1).
90. Liu, T., et al., *BAF60a deficiency uncouples chromatin accessibility and cold sensitivity from white fat browning.* Nat Commun, 2020. **11**(1): p. 2379.
91. Kong, Q., et al., *BAF60a Deficiency in Macrophage Promotes Diet-Induced Obesity and Metabolic Inflammation.* Diabetes, 2022.
92. Neuschwander-Tetri, B.A., *Non-alcoholic fatty liver disease.* BMC Med, 2017. **15**(1): p. 45.

93. Lehman, J.J., et al., *Peroxisome proliferator-activated receptor gamma coactivator-1 promotes cardiac mitochondrial biogenesis.* J Clin Invest, 2000. **106**(7): p. 847-56.
94. Inoue, C., et al., *SMARCD1 regulates senescence-associated lipid accumulation in hepatocytes.* NPJ Aging Mech Dis, 2017. **3**: p. 11.
95. Luong, Q.E., J. Huang, and K.Y. Lee, *Deciphering White Adipose Tissue Heterogeneity.* Biology-Basel, 2019. **8**(2).
96. Wu, J., et al., *Beige adipocytes are a distinct type of thermogenic fat cell in mouse and human.* Cell, 2012. **150**(2): p. 366-76.
97. Ling, C. and T. Ronn, *Epigenetics in Human Obesity and Type 2 Diabetes.* Cell Metab, 2019. **29**(5): p. 1028-1044.
98. Ross, R., *Atherosclerosis--an inflammatory disease.* N Engl J Med, 1999. **340**(2): p. 115-26.
99. Ait-Oufella, H., et al., *Adaptive (T and B cells) immunity and control by dendritic cells in atherosclerosis.* Circ Res, 2014. **114**(10): p. 1640-60.
100. Liu, Y.H., et al., *Dysregulated oxalate metabolism is a driver and therapeutic target in atherosclerosis.* Cell Reports, 2021. **36**(4).
101. Jonasson, L., et al., *Regional accumulations of T cells, macrophages, and smooth muscle cells in the human atherosclerotic plaque.* Arteriosclerosis, 1986. **6**(2): p. 131-8.
102. Zhou, X.H., S. Stemme, and G.K. Hansson, *Evidence for a local immune response in atherosclerosis - CD4(+) T cells infiltrate lesions of apolipoprotein-E-deficient mice.* American Journal of Pathology, 1996. **149**(2): p. 359-366.
103. Doran, A.C., et al., *B-cell aortic homing and atheroprotection depend on Id3.* Circ Res, 2012. **110**(1): p. e1-12.
104. Zhou, X. and G.K. Hansson, *Detection of B cells and proinflammatory cytokines in atherosclerotic plaques of hypercholesterolaemic apolipoprotein E knockout mice.* Scand J Immunol, 1999. **50**(1): p. 25-30.
105. Gautier, E.L., et al., *Conventional Dendritic Cells at the Crossroads Between Immunity and Cholesterol Homeostasis in Atherosclerosis.* Circulation, 2009. **119**(17): p. 2367-U151.
106. Banach, M. and P.E. Penson, *Lipid-lowering therapies: Better together.* Atherosclerosis, 2021. **320**: p. 86-88.
107. Vincent, J., *Lipid Lowering Therapy for Atherosclerotic Cardiovascular Disease: It Is Not So Simple.* Clinical Pharmacology & Therapeutics, 2018. **104**(2): p. 220-224.
108. Lorenzatti, A.J., *Anti-inflammatory Treatment and Cardiovascular Outcomes: Results of Clinical Trials.* Eur Cardiol, 2021. **16**: p. e15.
109. Brandes, R.P. and R. Gilsbach, *Understanding Arteriosclerosis 2.0: Making Sense of Genetic Variants with scATAC.* Circ Res, 2021. **129**(2): p. 259-261.
110. Ord, T., et al., *Single-Cell Epigenomics and Functional Fine-Mapping of Atherosclerosis GWAS Loci.* Circ Res, 2021. **129**(2): p. 240-258.
111. Hou, H. and H. Zhao, *Epigenetic factors in atherosclerosis: DNA methylation, folic acid metabolism, and intestinal microbiota.* Clin Chim Acta, 2021. **512**: p. 7-11.
112. Fisslthaler, B., et al., *Myeloid-Specific Deletion of the AMPKalpha2 Subunit Alters Monocyte Protein Expression and Atherogenesis.* Int J Mol Sci, 2019. **20**(12).
113. Zhang, M., et al., *Ablation of Myeloid ADK (Adenosine Kinase) Epigenetically Suppresses Atherosclerosis in ApoE(-/-) (Apolipoprotein E Deficient) Mice.* Arteriosclerosis Thrombosis and Vascular Biology, 2018. **38**(12): p. 2780-2792.

114. Chang, Z., et al., *BAF60a Deficiency in Vascular Smooth Muscle Cells Prevents Abdominal Aortic Aneurysm by Reducing Inflammation and Extracellular Matrix Degradation.* Arterioscler Thromb Vasc Biol, 2020. **40**(10): p. 2494-2507.
115. Lv, Y.C., et al., *Histone Methyltransferase Enhancer of Zeste Homolog 2-Mediated ABCA1 Promoter DNA Methylation Contributes to the Progression of Atherosclerosis.* PLoS One, 2016. **11**(6): p. e0157265.
116. Peng, J., et al., *Tet methylcytosine dioxygenase 2 inhibits atherosclerosis via upregulation of autophagy in ApoE-/- mice.* Oncotarget, 2016. **7**(47): p. 76423-76436.
117. Liu, Y., et al., *Emerging roles and mechanisms of long noncoding RNAs in atherosclerosis.* Int J Cardiol, 2017. **228**: p. 570-582.
118. Moroni, F., et al., *The Role of Monocytes and Macrophages in Human Atherosclerosis, Plaque Neoangiogenesis, and Atherothrombosis.* Mediators Inflamm, 2019. **2019**: p. 7434376.
119. Lin, P., et al., *Macrophage Plasticity and Atherosclerosis Therapy.* Front Mol Biosci, 2021. **8**: p. 679797.
120. Shioi, A. and Y. Ikari, *Plaque Calcification During Atherosclerosis Progression and Regression.* J Atheroscler Thromb, 2018. **25**(4): p. 294-303.
121. Jinnouchi, H., et al., *Diversity of macrophage phenotypes and responses in atherosclerosis.* Cell Mol Life Sci, 2020. **77**(10): p. 1919-1932.
122. Boyle, J.J., et al., *Heme induces heme oxygenase 1 via Nrf2: role in the homeostatic macrophage response to intraplaque hemorrhage.* Arterioscler Thromb Vasc Biol, 2011. **31**(11): p. 2685-91.
123. Chinetti-Gbaguidi, G., et al., *Human atherosclerotic plaque alternative macrophages display low cholesterol handling but high phagocytosis because of distinct activities of the PPARgamma and LXRalpha pathways.* Circ Res, 2011. **108**(8): p. 985-95.
124. Li, Y., et al., *Pleiotropic regulation of macrophage polarization and tumorigenesis by formyl peptide receptor-2.* Oncogene, 2011. **30**(36): p. 3887-99.
125. Colin, S., G. Chinetti-Gbaguidi, and B. Staels, *Macrophage phenotypes in atherosclerosis.* Immunol Rev, 2014. **262**(1): p. 153-66.
126. Domschke, G. and C.A. Gleissner, *CXCL4-induced macrophages in human atherosclerosis.* Cytokine, 2019. **122**: p. 154141.
127. Kadl, A., et al., *Identification of a Novel Macrophage Phenotype That Develops in Response to Atherogenic Phospholipids via Nrf2.* Circulation Research, 2010. **107**(6): p. 737-U155.
128. Cochain, C., et al., *Single-Cell RNA-Seq Reveals the Transcriptional Landscape and Heterogeneity of Aortic Macrophages in Murine Atherosclerosis.* Circ Res, 2018. **122**(12): p. 1661-1674.
129. Zhao, G., et al., *Single-cell RNA sequencing reveals the cellular heterogeneity of aneurysmal infrarenal abdominal aorta.* Cardiovasc Res, 2021. **117**(5): p. 1402-1416.
130. Zhao, G., et al., *Single-Cell Transcriptomics Reveals Endothelial Plasticity During Diabetic Atherogenesis.* Front Cell Dev Biol, 2021. **9**: p. 689469.
131. Kim, K., et al., *Transcriptome Analysis Reveals Nonfoamy Rather Than Foamy Plaque Macrophages Are Proinflammatory in Atherosclerotic Murine Models.* Circ Res, 2018. **123**(10): p. 1127-1142.

132. Lin, J.D., et al., *Single-cell analysis of fate-mapped macrophages reveals heterogeneity, including stem-like properties, during atherosclerosis progression and regression.* JCI Insight, 2019. **4**(4).
133. Xiong, X., et al., *Landscape of Intercellular Crosstalk in Healthy and NASH Liver Revealed by Single-Cell Secretome Gene Analysis.* Mol Cell, 2019. **75**(3): p. 644-660 e5.
134. Qing, J., et al., *Mitochondrial metabolism in regulating macrophage polarization: an emerging regulator of metabolic inflammatory diseases.* Acta Biochim Biophys Sin (Shanghai), 2020. **52**(9): p. 917-926.
135. Shrivastava, R., et al., *M2 polarization of macrophages by Oncostatin M in hypoxic tumor microenvironment is mediated by mTORC2 and promotes tumor growth and metastasis.* Cytokine, 2019. **118**: p. 130-143.
136. Gordon, S. and F.O. Martinez, *Alternative activation of macrophages: mechanism and functions.* Immunity, 2010. **32**(5): p. 593-604.
137. Feng, J., et al., *IL-25 stimulates M2 macrophage polarization and thereby promotes mitochondrial respiratory capacity and lipolysis in adipose tissues against obesity.* Cell Mol Immunol, 2018. **15**(5): p. 493-505.
138. Van den Bossche, J., et al., *Mitochondrial Dysfunction Prevents Repolarization of Inflammatory Macrophages.* Cell Rep, 2016. **17**(3): p. 684-696.
139. Cabrera, J.A., et al., *Uncoupling protein-2 expression and effects on mitochondrial membrane potential and oxidant stress in heart tissue.* Translational Research, 2012. **159**(5): p. 383-390.
140. Orekhov, A.N., et al., *Mitochondrion as a Selective Target for the Treatment of Atherosclerosis: Role of Mitochondrial DNA Mutations and Defective Mitophagy in the Pathogenesis of Atherosclerosis and Chronic Inflammation.* Current Neuropharmacology, 2020. **18**(11): p. 1064-1075.
141. O'Neill, L.A.J. and E.J. Pearce, *Immunometabolism governs dendritic cell and macrophage function.* Journal of Experimental Medicine, 2016. **213**(1): p. 15-23.
142. Reid, M.A., Z. Dai, and J.W. Locasale, *The impact of cellular metabolism on chromatin dynamics and epigenetics.* Nat Cell Biol, 2017. **19**(11): p. 1298-1306.
143. Britt, E.C., et al., *Metabolic regulation of epigenetic remodeling in immune cells.* Curr Opin Biotechnol, 2020. **63**: p. 111-117.
144. Liu, P.S., et al., *alpha-ketoglutarate orchestrates macrophage activation through metabolic and epigenetic reprogramming.* Nat Immunol, 2017. **18**(9): p. 985-994.
145. Covarrubias, A.J., et al., *Akt-mTORC1 signaling regulates Acly to integrate metabolic input to control of macrophage activation.* Elife, 2016. **5**.
146. Tong, W.H., et al., *TLR-activated repression of Fe-S cluster biogenesis drives a metabolic shift and alters histone and tubulin acetylation.* Blood Adv, 2018. **2**(10): p. 1146-1156.
147. Langston, P.K., et al., *Glycerol phosphate shuttle enzyme GPD2 regulates macrophage inflammatory responses.* Nat Immunol, 2019. **20**(9): p. 1186-1195.
148. Seim, G.L., et al., *Two-stage metabolic remodelling in macrophages in response to lipopolysaccharide and interferon-gamma stimulation.* Nat Metab, 2019. **1**(7): p. 731-742.
149. Duroux-Richard, I., F. Apparailly, and M. Khoury, *Mitochondrial MicroRNAs Contribute to Macrophage Immune Functions Including Differentiation, Polarization, and Activation.* Front Physiol, 2021. **12**: p. 738140.

150. Curtale, G., M. Rubino, and M. Locati, *MicroRNAs as Molecular Switches in Macrophage Activation.* Frontiers in Immunology, 2019. **10**.
151. Kwon, H., et al., *Nucleosome disruption and enhancement of activator binding by a human SW1/SNF complex.* Nature, 1994. **370**(6489): p. 477-81.
152. Wang, W., et al., *Purification and biochemical heterogeneity of the mammalian SWI-SNF complex.* EMBO J, 1996. **15**(19): p. 5370-82.
153. Wang, R.R., et al., *The SWI/SNF chromatin-remodeling factors BAF60a, b, and c in nutrient signaling and metabolic control.* Protein Cell, 2018. **9**(2): p. 207-215.
154. Meng, Z.X., et al., *Glucose Sensing by Skeletal Myocytes Couples Nutrient Signaling to Systemic Homeostasis.* Molecular Cell, 2017. **66**(3): p. 332-+.
155. Zhao, Y., et al., *Suppression of Vascular Macrophage Activation by Nitro-Oleic Acid and its Implication for Abdominal Aortic Aneurysm Therapy.* Cardiovasc Drugs Ther, 2021. **35**(5): p. 939-951.
156. Zhu, W., et al., *Myeloid TM6SF2 Deficiency Inhibits Atherosclerosis.* Cells, 2022. **11**(18).
157. Roychowdhury, T., et al., *Regulatory variants in TCF7L2 are associated with thoracic aortic aneurysm.* Am J Hum Genet, 2021. **108**(9): p. 1578-1589.
158. Hao, Y., et al., *Integrated analysis of multimodal single-cell data.* Cell, 2021. **184**(13): p. 3573-3587 e29.
159. Newman, A.M., et al., *Determining cell type abundance and expression from bulk tissues with digital cytometry.* Nat Biotechnol, 2019. **37**(7): p. 773-782.
160. Peters, S.A.E., P. Muntner, and M. Woodward, *Sex Differences in the Prevalence of, and Trends in, Cardiovascular Risk Factors, Treatment, and Control in the United States, 2001 to 2016.* Circulation, 2019. **139**(8): p. 1025-1035.
161. Hu, W., et al., *Kruppel-like factor 14, a coronary artery disease associated transcription factor, inhibits endothelial inflammation via NF-kappaB signaling pathway.* Atherosclerosis, 2018. **278**: p. 39-48.
162. Javadifar, A., et al., *Foam Cells as Therapeutic Targets in Atherosclerosis with a Focus on the Regulatory Roles of Non-Coding RNAs.* International Journal of Molecular Sciences, 2021. **22**(5).
163. Zhang, S., et al., *Targeting the Microenvironment of Vulnerable Atherosclerotic Plaques: An Emerging Diagnosis and Therapy Strategy for Atherosclerosis.* Adv Mater, 2022. **34**(29): p. e2110660.
164. Ward, L.J., et al., *Exposure to atheroma-relevant 7-oxysterols causes proteomic alterations in cell death, cellular longevity, and lipid metabolism in THP-1 macrophages.* PLoS One, 2017. **12**(3): p. e0174475.
165. Xiao, Q., et al., *Macrophage autophagy regulates mitochondria-mediated apoptosis and inhibits necrotic core formation in vulnerable plaques.* J Cell Mol Med, 2020. **24**(1): p. 260-275.
166. Virbasius, C.A., J.V. Virbasius, and R.C. Scarpulla, *NRF-1, an activator involved in nuclear-mitochondrial interactions, utilizes a new DNA-binding domain conserved in a family of developmental regulators.* Genes Dev, 1993. **7**(12A): p. 2431-45.
167. Kiyama, T., et al., *Essential roles of mitochondrial biogenesis regulator Nrf1 in retinal development and homeostasis.* Mol Neurodegener, 2018. **13**(1): p. 56.
168. Nordon, I.M., et al., *Pathophysiology and epidemiology of abdominal aortic aneurysms.* Nat Rev Cardiol, 2011. **8**(2): p. 92-102.

169. Moll, F.L., et al., *Management of abdominal aortic aneurysms clinical practice guidelines of the European society for vascular surgery.* Eur J Vasc Endovasc Surg, 2011. **41 Suppl 1**: p. S1-S58.
170. Raffort, J., et al., *Monocytes and macrophages in abdominal aortic aneurysm.* Nat Rev Cardiol, 2017. **14**(8): p. 457-471.
171. Li, H., et al., *Modulation of Immune-Inflammatory Responses in Abdominal Aortic Aneurysm: Emerging Molecular Targets.* J Immunol Res, 2018. **2018**: p. 7213760.
172. Siasos, G., et al., *The Role of Endothelial Dysfunction in Aortic Aneurysms.* Curr Pharm Des, 2015. **21**(28): p. 4016-34.
173. Chen, H.Z., et al., *Age-Associated Sirtuin 1 Reduction in Vascular Smooth Muscle Links Vascular Senescence and Inflammation to Abdominal Aortic Aneurysm.* Circ Res, 2016. **119**(10): p. 1076-1088.
174. Ackers-Johnson, M., et al., *Myocardin regulates vascular smooth muscle cell inflammatory activation and disease.* Arterioscler Thromb Vasc Biol, 2015. **35**(4): p. 817-28.
175. Jiang, W., D.K. Agrawal, and C.S. Boosani, *Cellspecific histone modifications in atherosclerosis (Review).* Mol Med Rep, 2018. **18**(2): p. 1215-1224.
176. Ito, T., et al., *Identification of SWI.SNF complex subunit BAF60a as a determinant of the transactivation potential of Fos/Jun dimers.* J Biol Chem, 2001. **276**(4): p. 2852-7.
177. Alajem, A., et al., *Differential association of chromatin proteins identifies BAF60a/SMARCD1 as a regulator of embryonic stem cell differentiation.* Cell Rep, 2015. **10**(12): p. 2019-31.
178. Tao, W., et al., *SWItch/sucrose nonfermentable (SWI/SNF) complex subunit BAF60a integrates hepatic circadian clock and energy metabolism.* Hepatology, 2011. **54**(4): p. 1410-20.
179. Lenk, G.M., et al., *Whole genome expression profiling reveals a significant role for immune function in human abdominal aortic aneurysms.* BMC Genomics, 2007. **8**: p. 237.
180. Nakaoka, H., et al., *Gene expression profiling reveals distinct molecular signatures associated with the rupture of intracranial aneurysm.* Stroke, 2014. **45**(8): p. 2239-45.
181. Lu, H., et al., *Hypercholesterolemia Induced by a PCSK9 Gain-of-Function Mutation Augments Angiotensin II-Induced Abdominal Aortic Aneurysms in C57BL/6 Mice-Brief Report.* Arterioscler Thromb Vasc Biol, 2016. **36**(9): p. 1753-7.
182. Zhang, C., et al., *Matricellular protein CCN3 mitigates abdominal aortic aneurysm.* The Journal of Clinical Investigation, 2016. **126**(4): p. 1282-1299.
183. Bhamidipati, C.M., et al., *Development of a novel murine model of aortic aneurysms using peri-adventitial elastase.* Surgery, 2012. **152**(2): p. 238-46.
184. Benjamin, E.J., et al., *Heart Disease and Stroke Statistics-2018 Update: A Report From the American Heart Association.* Circulation, 2018. **137**(12): p. e67-e492.
185. Zhao, G., et al., *Unspliced XBP1 Confers VSMC Homeostasis and Prevents Aortic Aneurysm Formation via FoxO4 Interaction.* Circ Res, 2017. **121**(12): p. 1331-1345.
186. Gjurich, B.N., P.L. Taghavie-Moghadam, and E.V. Galkina, *Flow Cytometric Analysis of Immune Cells Within Murine Aorta*, in *Methods in Mouse Atherosclerosis*, V. Andrés and B. Dorado, Editors. 2015, Springer New York: New York, NY. p. 161-175.

187. Wang, F., et al., *RNAscope: A Novel in Situ RNA Analysis Platform for Formalin-Fixed, Paraffin-Embedded Tissues.* The Journal of Molecular Diagnostics, 2012. **14**(1): p. 22-29.
188. Hamblin, M., L. Chang, and Y.E. Chen, *Isolation and Culture of Vascular smooth Muscle Cells.* Manual of Research Techniques in Cardiovascular Medicine, 2014: p. 125-130.
189. Li, S., et al., *Genome-wide coactivation analysis of PGC-1alpha identifies BAF60a as a regulator of hepatic lipid metabolism.* Cell Metab, 2008. **8**(2): p. 105-17.
190. Lu, H., et al., *Novel gene regulatory networks identified in response to nitro-conjugated linoleic acid in human endothelial cells.* Physiological Genomics, 2019. **51**(6): p. 224-233.
191. Patro, R., et al., *Salmon provides fast and bias-aware quantification of transcript expression.* Nature Methods, 2017. **14**: p. 417.
192. Love, M.I., W. Huber, and S. Anders, *Moderated estimation of fold change and dispersion for RNA-seq data with DESeq2.* Genome biology, 2014. **15**(12): p. 550-550.
193. Subramanian, A., et al., *Gene set enrichment analysis: A knowledge-based approach for interpreting genome-wide expression profiles.* Proceedings of the National Academy of Sciences, 2005. **102**(43): p. 15545.
194. Robinson, J.T., et al., *Integrative genomics viewer.* Nature biotechnology, 2011. **29**(1): p. 24-26.
195. Petsophonsakul, P., et al., *Role of Vascular Smooth Muscle Cell Phenotypic Switching and Calcification in Aortic Aneurysm Formation.* Arteriosclerosis, Thrombosis, and Vascular Biology, 2019. **39**(7): p. 1351-1368.
196. Qin, Y., et al., *Deficiency of cathepsin S attenuates angiotensin II-induced abdominal aortic aneurysm formation in apolipoprotein E-deficient mice.* Cardiovasc Res, 2012. **96**(3): p. 401-10.
197. Wang, F., et al., *RNAscope: a novel in situ RNA analysis platform for formalin-fixed, paraffin-embedded tissues.* J Mol Diagn, 2012. **14**(1): p. 22-9.
198. Kadoglou, N.P. and C.D. Liapis, *Matrix metalloproteinases: contribution to pathogenesis, diagnosis, surveillance and treatment of abdominal aortic aneurysms.* Curr Med Res Opin, 2004. **20**(4): p. 419-32.
199. Longo, G.M., et al., *Matrix metalloproteinases 2 and 9 work in concert to produce aortic aneurysms.* The Journal of Clinical Investigation, 2002. **110**(5): p. 625-632.
200. Gjurich, B.N., P.L. Taghavie-Moghadam, and E.V. Galkina, *Flow Cytometric Analysis of Immune Cells Within Murine Aorta.* Methods Mol Biol, 2015. **1339**: p. 161-75.
201. Golledge, A.L., et al., *A systematic review of studies examining inflammation associated cytokines in human abdominal aortic aneurysm samples.* Dis Markers, 2009. **26**(4): p. 181-8.
202. Subramanian, A., et al., *Gene set enrichment analysis: a knowledge-based approach for interpreting genome-wide expression profiles.* Proceedings of the National Academy of Sciences of the United States of America, 2005. **102**(43): p. 15545-15550.
203. Ramirez-Carrozzi, V.R., et al., *Selective and antagonistic functions of SWI/SNF and Mi-2beta nucleosome remodeling complexes during an inflammatory response.* Genes Dev, 2006. **20**(3): p. 282-96.
204. Heintzman, N.D., et al., *Distinct and predictive chromatin signatures of transcriptional promoters and enhancers in the human genome.* Nat Genet, 2007. **39**(3): p. 311-8.

205. Wang, Z., et al., *Combinatorial patterns of histone acetylations and methylations in the human genome.* Nat Genet, 2008. **40**(7): p. 897-903.
206. Calao, M., et al., *A pervasive role of histone acetyltransferases and deacetylases in an NF-kappaB-signaling code.* Trends Biochem Sci, 2008. **33**(7): p. 339-49.
207. Huang, Z.Q., et al., *A role for cofactor-cofactor and cofactor-histone interactions in targeting p300, SWI/SNF and Mediator for transcription.* EMBO J, 2003. **22**(9): p. 2146-55.
208. Alver, B.H., et al., *The SWI/SNF chromatin remodelling complex is required for maintenance of lineage specific enhancers.* Nat Commun, 2017. **8**: p. 14648.
209. Michel, B.C., et al., *A non-canonical SWI/SNF complex is a synthetic lethal target in cancers driven by BAF complex perturbation.* Nature Cell Biology, 2018. **20**(12): p. 1410-1420.
210. Saccani, S., S. Pantano, and G. Natoli, *Two waves of nuclear factor kappaB recruitment to target promoters.* J Exp Med, 2001. **193**(12): p. 1351-9.
211. Zhang, J., et al., *Generation of an adult smooth muscle cell-targeted Cre recombinase mouse model.* Arterioscler Thromb Vasc Biol, 2006. **26**(3): p. e23-4.
212. Wirth, A., et al., *G12-G13-LARG-mediated signaling in vascular smooth muscle is required for salt-induced hypertension.* Nat Med, 2008. **14**(1): p. 64-8.
213. Xin, H.B., et al., *Smooth muscle expression of Cre recombinase and eGFP in transgenic mice.* Physiol Genomics, 2002. **10**(3): p. 211-5.
214. Miano, J.M., et al., *Smooth muscle myosin heavy chain exclusively marks the smooth muscle lineage during mouse embryogenesis.* Circ Res, 1994. **75**(5): p. 803-12.
215. Liu, Z., et al., *Systematic comparison of 2A peptides for cloning multi-genes in a polycistronic vector.* Sci Rep, 2017. **7**(1): p. 2193.